

Measurement of the Polarisation Dependence of
Charged Current Cross Sections in e^+p Deep
Inelastic Scattering at $\sqrt{s} = 318$ GeV

Mayuko Kataoka

January 2005

Abstract

The first measurements of the single differential and total cross sections of the charged current deep inelastic scattering for $Q^2 > 200 \text{ GeV}^2$ in e^+p collisions with longitudinally polarised positron beams at a centre of energy of 318 GeV are performed. These measurements are based on two data sets with opposite signed polarisation P . The integrated luminosities are 22.7 pb^{-1} for $P = +32.6 \pm 0.9 \%$ and 16.4 pb^{-1} for $P = -40.2 \pm 1.2 \%$ taken by the ZEUS detector from 2003 autumn to 2004 summer. The polarised cross section is significantly different from the previously measured unpolarised cross section and is consistent with the absence of right-handed current in the Standard Model. The results are compared with the Standard Model. A lower limit of the mass of right-handed W boson is derived.

Contents

1	INTRODUCTION	1
2	DEEP INELASTIC SCATTERING	4
2.1	Kinematics of lepton-nucleon scattering	4
2.2	Cross section of CC DIS	6
2.3	W_R searches in the other experiments	9
2.4	Electroweak radiative correction	9
3	HERA and the ZEUS detector	11
3.1	The HERA collider	11
3.2	The ZEUS detector	12
3.2.1	Central Tracking Detector (CTD)	16
3.2.2	Uranium scintillator calorimeter (CAL)	16
3.2.3	Luminosity Monitor	18
3.3	C5 counter	19
3.4	ZEUS data acquisition and trigger system	20
3.4.1	First Level Trigger (FLT)	20
3.4.2	Second Level Trigger (SLT)	20
3.4.3	Third Level Trigger (TLT)	21
3.5	Polarimeter	21
3.5.1	Transverse polarimeter (TPOL)	22
3.5.2	Longitudinal polarimeter (LPOL)	23
3.5.3	Polarisation for this analysis	23
4	Monte Carlo simulation (MC)	32
4.1	DIS Event Generator	32
4.2	Signal Monte Carlo	33
4.3	Event generators for background processes	33
4.3.1	Photoproduction	33
4.3.2	Neutral current DIS	34
4.3.3	Di-lepton production	34

4.3.4	W production	35
5	RECONSTRUCTION OF KINEMATICS	37
5.1	Reconstruction methods	37
5.1.1	The Jacquet-Blondel method	37
5.1.2	The Double Angle method	38
5.2	Energy reconstruction	39
5.2.1	Noise suppression for the CAL	39
5.2.2	Clustering of energy deposits	39
5.2.3	Energy corrections for the CAL clusters	40
5.2.4	Reconstruction of charged current kinematic variables	41
5.3	Vertex reconstruction	42
6	EVENT SELECTION	46
6.1	Trigger requirement	46
6.1.1	FLT selection	46
6.1.2	SLT selection	48
6.1.3	TLT selection	49
6.1.4	pre-selection	50
6.2	Kinematic region	51
6.3	Selection for high- γ_0 and low- γ_0 events	51
6.3.1	Selection for high- γ_0 events	51
6.3.2	Selection for low- γ_0 events	58
6.4	Non- ep background rejection	64
6.4.1	Halo-muon and Cosmic-muon rejection with HAC fraction	64
6.4.2	Spark rejection	64
6.4.3	CAL timing cut	65
6.4.4	Summary of CC DIS selection	67
7	CROSS SECTION MEASUREMENTS	73
7.1	Outline	73
7.2	Bin definition for differential cross section	74
7.3	Background estimation	74
7.4	Acceptance correction	74
7.5	Born cross section	79
7.6	Bin centring correction	81
7.7	Total cross section	83
7.8	Systematic uncertainties	83
7.8.1	Calorimeter energy scale	83
7.8.2	Selection procedures	84
7.8.3	Monte Carlo fragmentation model	84

7.8.4	Background subtraction	86
7.8.5	Trigger efficiency	87
7.8.6	Summary for systematic uncertainty	88
8	RESULTS	94
8.1	Single differential cross section	94
8.2	Total cross section	101
9	Discussion of search of W_R boson	104
9.1	Limit of σ_{CC}^R	104
10	CONCLUSION	108
.1	The method of linear least squares fitting	110

List of Figures

2.1	Leading-order Feynman diagrams for deep inelastic ep scattering . . .	5
2.2	Polarisation dependence of the total charged current cross section . .	8
2.3	Diagram of W_R production in ep collision	9
2.4	Diagram of W_R production in pp collision	10
3.1	Layout of the HERA collider	12
3.2	Experiments on HERA and spin rotators	13
3.3	Integrated luminosity delivered at HERA I and HERA II	14
3.4	Layout(r-z view) of ZEUS detector	15
3.5	Layout(x-y view) of ZEUS detector	15
3.6	CTD wires arrangement	17
3.7	A view of the ZEUS calorimeter	18
3.8	A module of the ZEUS calorimeter	24
3.9	Luminosity detectors	25
3.10	Luminosity monitors	26
3.11	Schematic diagram of the ZEUS trigger and DAQ system	27
3.12	Transverse Polarimeter	28
3.13	Setup of the transverse polarimeter	29
3.14	Longitudinal Polarimeter	30
3.15	polarisation of the positron beam in one fill	31
3.16	HERA average positron polarisation for each day	31
4.1	Diagrams of photoproduction	34
4.2	A diagram of the di-lepton process	35
4.3	A diagram of W production	36
5.1	Efficiency and resolution of CTD and FCAL timing vertices	44
5.2	Z vertex distribution of NC real data at $P = +32.6\%$ and $P = -40.2\%$	45
6.1	CTD track classification at FLT level	47
6.2	Missing transverse momentum for high- γ_0 sample	52
6.3	Z vertex distribution measured by CTD for high γ_0	53
6.4	$P_{T,miss}/E_T$ distributions for high- γ_0	54

6.5	$P_{T,miss}$ distribution of the beam-gas enriched sample	55
6.6	Tracking cut for events with $P_{T,miss} > 25$ GeV	56
6.7	Tracking cut for events with $P_{T,miss} < 25$ GeV	57
6.8	$\Delta\phi$ distributions	58
6.9	NC-DIS rejection distributions	59
6.10	Missing transverse momentum $P_{T,miss}$ and $P_{T,miss}(-1ir)$ distribution for low- γ_0 sample	60
6.11	Z-vertex distribution for low- γ_0 events	61
6.12	Energy fractions in FCAL	62
6.13	Cluster size distributions in FCAL for low- γ_0 sample	63
6.14	The correlation of energy E and CAL timing T in each CAL section .	66
6.15	The correlation between energy and CAL timing in the upper and lower of halves of CAL	67
6.16	The correlation between energy and CAL timing in the upper and lower of halves of CAL	68
6.17	The correlation between energy and CAL timing in the upper and lower of halves of CAL.	69
6.18	The scattered plot of final CC candidates in the Q^2 - x plane	71
6.19	Distributions of CC final candidates	72
7.1	The resolution of the measured Q^2	75
7.2	The resolution of the measured x	76
7.3	The resolution of the measured y	77
7.4	Selection efficiency, Efficiency, Purity and Acceptance in Q^2 bin . . .	80
7.5	Selection efficiency, Efficiency, Purity and Acceptance in x bin	81
7.6	Selection efficiency, Efficiency, Purity and Acceptance in y bin	82
7.7	Systematic uncertainty due to the calorimeter energy scale	85
7.8	Systematic uncertainty due to the selection threshold	90
7.9	$P_{T,miss}/E_T$ distribution for the high- γ_0 events with $200 < Q^2 < 400$ GeV ²	91
7.10	The FLT trigger slot60 efficiency as a function of $P_{T,miss}$	92
7.11	Summary of systematic uncertainties for the single differential cross sections	93
8.1	The single differential cross sections as function of Q^2 , x , y	101
8.2	The measured total cross sections	103
9.1	Theory prediction of W_R mass	107

List of Tables

3.1	HERA machine parameters	13
3.2	Summary of ZEUS taken luminosity and polarisation at HERA II . . .	13
4.1	Charged Current Monte Carlo samples	33
4.2	Background Monte Carlo	34
6.1	A summary of selection cuts and their efficiencies	70
7.1	Number of background event expected by MC samples	78
7.2	Systematic check categories and varied threshold of selection variables	86
7.3	Systematic uncertainties for the total cross section	89
8.1	The single differential cross sections $d\sigma/dQ^2$ for the e^+p data with $P = +32.6\%$	95
8.2	The single differential cross sections $d\sigma/dQ^2$ for the e^+p data with $P = -40.2\%$	96
8.3	The single differential cross sections $d\sigma/dx$ for the e^+p data with $P = +32.6\%$	97
8.4	The single differential cross sections $d\sigma/dx$ for the e^+p data with $P = -40.2\%$	98
8.5	The single differential cross sections $d\sigma/dy$ for the e^+p data with $P = +32.6\%$	99
8.6	The single differential cross sections $d\sigma/dy$ for the e^+p data with $P = -40.2\%$	100
9.1	Systematic uncertainties for the total cross section	106
9.2	Results of the extrapolation to $P = -100\%$	107

Chapter 1

INTRODUCTION

It is possible to say that the first scattering experiment for investigating the substructure of the matter was started by E. Rutherford in 1911 [1]. In the collision of α -particles from a radioactive source to a target of gold foil, Rutherford discovered the existence of *point-like* charged structures inside the gold through the distribution of scattering angles. This is to say the discovery of the atomic nucleus.

In 1969, the SLAC experiments with multi-GeV electron beams found the substructure of the nucleon in much the same way as Rutherford demonstrated the existence of nuclei. In the deep inelastic scattering (DIS) region, where the target proton is excited to higher mass than the various resonance states, they observed a scattering angle distribution not as steep as expected if the proton has a uniform charge distribution in a sphere of the nucleon radius. Furthermore, initial measurements of the nucleon structure functions revealed the scaling behaviour predicted by Bjorken. These facts suggested that there are point-like contents, *partons*, inside the nucleon as predicted by Feynman thought. Later the partons were identified as the quarks. By DIS experiments with electrons at SLAC and with neutrinos at CERN, the properties of the nucleon contents were extensively studied.

In 1973, weak neutral currents was discovered in neutrino DIS. The Glashow-Salam-Weinberg (GSW) model of spontaneously broken $SU(2)_L \times U(1)_Y$ electroweak local gauge symmetry helped this discovery. After that, the discoveries of the charm quark, the τ lepton and the bottom quark were followed from the various experiments in the world. The GSW theory also predicted the existence and masses of the heavy gauge bosons W^\pm and Z which the weak interaction is generated by the emission and absorption of them. They were first discovered in 1983 in $p\bar{p}$ collisions at CERN. The strong interaction between quarks is described via quantum chromodynamics (QCD), which is the gauge theory of strong interaction. The standard model was established by the gauge theory of $SU(3) \times SU(2)_L \times U(1)_Y$.

The subscript 'L' of weak sector $SU(2)_L$ in the gauge theory represents that weak interaction exists between left-handed particles. The history of the weak interaction began 70 years ago. The historical opening of the weak interaction is the observation that the electrons in β decay are emitted with a continuous spectrum of energy, so that it looked that energy and momentum are not conserved in β decay. In order to explain it, W. Pauli proposed that a neutral particle (neutrino) of nearly zero rest mass and spin 1/2 is emitted together with electron and that it escapes due to no interaction with surrounding material. This hypothetical particle, neutrino, was later identified in the scattering experiment.

In 1956, T.D. Lee and L.N. Yang explained the puzzle that the kaon decays both two and three pions whose final states have opposite parity. They proposed parity was not conserved in weak interaction, which was confirmed by C.S. Wu through detection of β emission of polarised ^{60}Co nuclei. It means that electron emitted in β decay has helicity -1, i.e. 'left-handed'. From various experiments, we observed the weak interaction occurs only between left-handed particles. However, we do not understand why it is so.

The first ep collider in the world, HERA, was built at DESY in Hamburg. HERA started to operate in 1992 and has been giving a place to study DIS with the highest energy. Measurement of DIS of leptons on nuclei have been a valuable method in understanding the structure of nucleons. Two kinds of DIS can be measured at HERA, neutral current DIS (NC: $e^{+(-)}p \rightarrow e^{+(-)}X$) and charged current DIS (CC: $e^{+(-)}p \rightarrow \bar{\nu}_e(\nu_e)X$). The unification of the electroweak interaction was first visualised through the comparison of NC and CC cross sections at $Q^2 \approx M_W^2$.

A total integrated luminosity of about 100 pb^{-1} (15 pb^{-1}) was collected with unpolarised positron (electron) beam from 1994 until 2000 (HERA I). HERA was upgraded in 2001-2002 (called HERA II). This was for the aim to provide high luminosity and longitudinally polarised lepton for the collider experiments. HERA II e^+p collisions with a longitudinally polarized positron beam started in 2003. By measuring the CC DIS cross sections and these polarisation dependence, the first measurement of the right- and left-handed asymmetry in the weak interaction is possible.

In this thesis, the first measurements of total cross sections and its polarisation

dependence in e^+p deep inelastic scattering are presented. The two independent data sets which have the e^+ polarisation of $+32.6 \pm 0.9 \%$ and $-40.2 \pm 1.2 \%$ are used in this analysis. Their luminosities are 22.7 pb^{-1} and 16.4 pb^{-1} , respectively. Single differential cross sections are also measured as a function of Q^2 , x and y . Using these measured cross section, cross section of right-handed charged current is extracted, and a lower limit for the right-handed charged current propagator mass is given.

This thesis is organised as follows. The theoretical framework is presented in Chapter 2. The HERA accelerator and ZEUS detector are introduced in Chapter 3, Monte Carlo simulation is explained in Chapter 4. Reconstruction of kinematic variables is described in Chapter 5. In Chapter 6, the CC DIS event selection is explained. The measurement of cross sections and its results are described in Chapter 7 and 8, respectively. In Chapter 9, we discuss measurement of right-handed charged current cross section. Finally, we summarise this analysis in Chapter 10.

Chapter 2

DEEP INELASTIC SCATTERING

2.1 Kinematics of lepton-nucleon scattering

Deep inelastic lepton (l)- nucleon (N) scattering is the process,

$$lN \rightarrow l'X \tag{2.1}$$

where l, l' are incoming lepton and outgoing lepton or antilepton, respectively. N represents a nucleon and X represents the hadronic final state particles. There are two major reactions, neutral current (NC) and charged current (CC) as shown in Figure 2.1 in leading order (LO) Feynman diagrams. The final state of these reactions consists of the scattered neutrino(lepton) and a hadronic system with many particles.

The kinematics of inclusive CC and NC DIS scattering reactions are defined by the four momenta k, p and k' , which are for the incoming lepton, the incoming nucleon and outgoing lepton, respectively. The reaction is mediated by the exchange of a gauge boson (γ, W, Z), with four momentum given by

$$q = k - k', \tag{2.2}$$

and the four momentum P_X of the hadronic final states system X is given by

$$P_X = p + q. \tag{2.3}$$

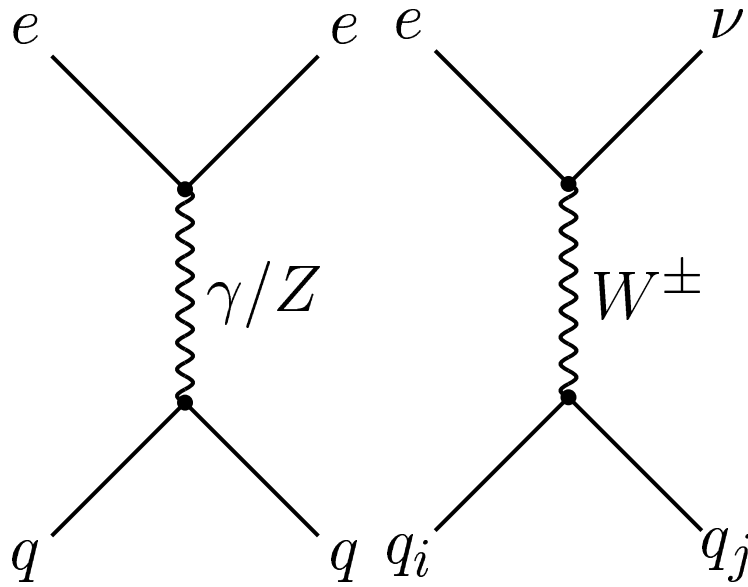


Figure 2.1: Leading-order Feynman diagrams for deep inelastic ep scattering: left and right diagrams denotes for NC and for CC, respectively.

The negative of the four momentum transfer squared Q^2 is useful in the description of the kinematics of the process,

$$Q^2 \equiv -q^2. \quad (2.4)$$

The Bjorken x variables is defined as

$$x \equiv \frac{Q^2}{2 p q}, \quad (2.5)$$

which means the fraction of the momentum of the incoming nucleon taken by the struck quark.

The inelasticity of the lepton, y is defined as

$$y \equiv \frac{p q}{p k}, \quad (2.6)$$

which means the amount of energy transferred between the lepton and the hadron systems in the proton rest frame.

These three variables have the following relation:

$$Q^2 = s x y, \quad (2.7)$$

where s is the center of mass (CM) energy squared for the reaction,

$$s \equiv (p + k)^2. \quad (2.8)$$

2.2 Cross section of CC DIS

CC DIS cross section with polarised lepton beams is generally written with the cross section for left-handed current (σ_{CC}^L) and right-handed one (σ_{CC}^R) as,

$$\sigma_{CC}^{e^\pm} = \frac{(1 \pm P)}{2} \sigma_{CC}^{L,e^\pm} + \frac{(1 \mp P)}{2} \sigma_{CC}^{R,e^\pm}, \quad (2.9)$$

where polarisation P of positron beam is defined using N_R and N_L , which are the number of right and left handed positrons in the beam, as follows:

$$P = \frac{N_R - N_L}{N_R + N_L}. \quad (2.10)$$

In the Standard Model (SM), there is no right-handed charged current and hence $\sigma_{CC}^{R,e^\pm} = 0$.

In the SM, cross section σ_{CC}^{L,e^\pm} is given in the differential formula,

$$\begin{aligned} \frac{d^2 \sigma_{CC}^{L,e^\pm}}{dx dQ^2} &= \frac{G_F^2}{2\pi x} \left(\frac{M_W^2}{M_W^2 + Q^2} \right)^2 \\ &\times \{ Y_+(y) F_2^{CC}(x, Q^2) - y^2 F_L^{CC}(x, Q^2) \mp Y_-(y) x F_3^{CC}(x, Q^2) \}. \end{aligned} \quad (2.11)$$

The M_W is the mass of the W boson. The G_F represent the Fermi coupling constant and $Y_\pm = 1 \pm (1-y)^2$. The F_L is the longitudinal structure function which is defined as $F_L = F_2 - 2xF_1$. The F_L is a term from the exchange of longitudinally polarised gauge bosons and is negligible at high Q^2 .

The charged current structure function, F_2^{CC} and $x F_3^{CC}$, are expressed as,

$$F_2^{CC} = \sum_i xq_i(x, Q^2) + \sum_i x\bar{q}_i(x, Q^2), \quad (2.12)$$

$$xF_3^{CC} = \sum_i xq_i(x, Q^2) - \sum_i x\bar{q}_i(x, Q^2), \quad (2.13)$$

where the q is the quark density contributing to the reaction and i runs flavour. The cross section is explicitly for e^+p scattering,

$$\begin{aligned} \frac{d^2\sigma_{CC}^{L^{e^+}}}{dx dQ^2} &= \frac{G_F^2}{\pi} \left(\frac{M_W^2}{M_W^2 + Q^2} \right)^2 \\ &\times [\bar{u}(x, Q^2) + \bar{c}(x, Q^2) + (1-y)^2(d(x, Q^2) + s(x, Q^2))], \end{aligned} \quad (2.14)$$

for e^-p scattering,

$$\begin{aligned} \frac{d^2\sigma_{CC}^{L^{e^-}}}{dx dQ^2} &= \frac{G_F^2}{\pi} \left(\frac{M_W^2}{M_W^2 + Q^2} \right)^2 \\ &\times [u(x, Q^2) + c(x, Q^2) + (1-y)^2(\bar{d}(x, Q^2) + \bar{s}(x, Q^2))], \end{aligned} \quad (2.15)$$

The behaviour of the total CC DIS cross section as a function of the P by the Standard Model is shown in Figure 2.2.

If W_R exists with the same coupling constant, G_F , the cross section σ_{CC}^R is given in the differential formula,

$$\begin{aligned} \frac{d^2\sigma_{CC}^{R^{e^\pm}}}{dx dQ^2} &= \frac{G_F^2}{2\pi x} \left(\frac{M_{W_R}^2}{M_{W_R}^2 + Q^2} \right)^2 \\ &\times \{Y_+(y)F_2^{CC}(x, Q^2) - y^2F_L^{CC}(x, Q^2) \mp Y_-(y)xF_3^{CC}(x, Q^2)\}. \end{aligned} \quad (2.16)$$

From the measurement of polarised CC DIS cross section, we can extract the mass limit of right-handed charged current.

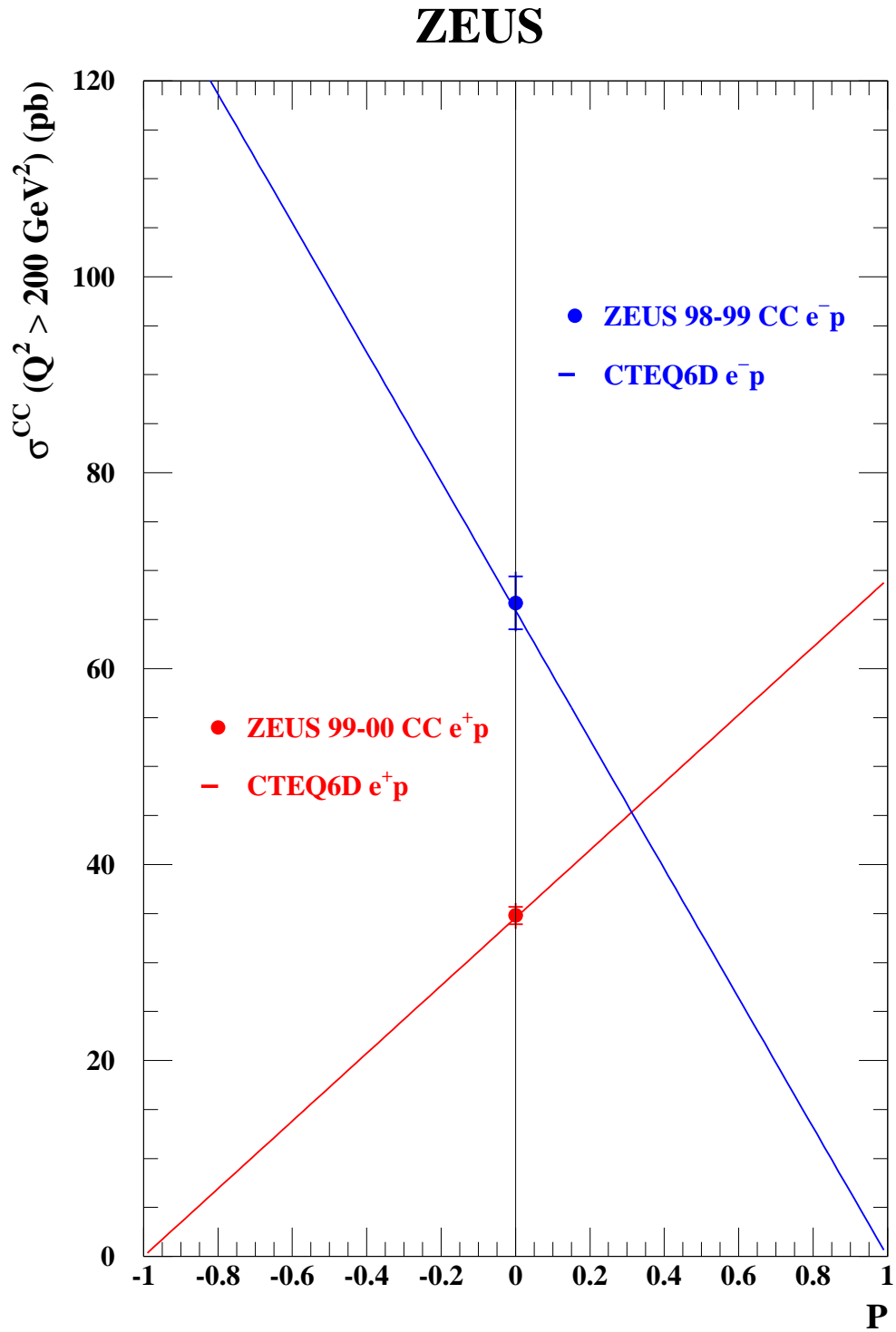
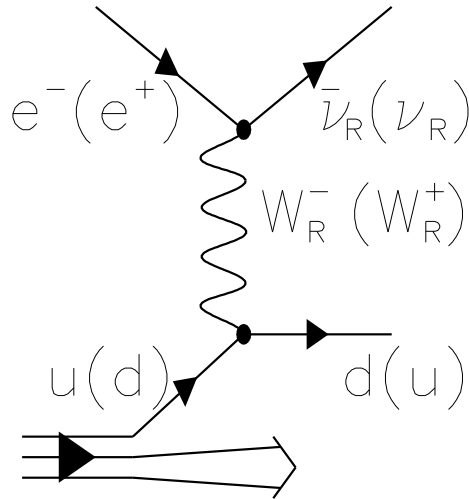


Figure 2.2: Dependence of the total charged current cross section

Figure 2.3: Diagram of W_R production in ep collision

2.3 W_R searches in the other experiments

W_R has been searched in various experiments at CERN and Fermilab¹. If ν_R is heavier than W_R , UA2 experiment had excluded a W_R in the mass range of 100 to 251 GeV [2]. D0 excludes the mass range of 340 to 680 GeV [3]. If ν_R is lighter than W_R , D0 has a limit of $M_{W_R} > 720$ GeV [4]. If ν_R is stable and much lighter than W_R , CDF has a limit of $M_{W_R} > 652$ GeV [5]. At $p\bar{p}$ collider, W_R is searched via s -channel as Figure 2.4.

In HERA collider, we can search W_R via t -channel virtual exchange in charged current processes as shown in Figure 2.3. For an integrated luminosity of 500 pb^{-1} at each opposite signed polarisation, the W_R mass limit will be excluded to 400 GeV to 500 GeV [6]. This is lower than $p\bar{p}$ collider, however we can search W_R at the different kinematic region and further measure directly cross section of W_R .

2.4 Electroweak radiative correction

In order to obtain the Born level cross section in this analysis, the radiative correction must be implemented. The contributions from *initial state radiation* (ISR) from the incoming positron and quark, *final state radiation* (FSR) from the scattered quark and photon radiation from the W are responsible for the radiative correction. Among them, a large contribute is from the ISR which affects the reconstruction of kinematic variables.

The cross section in the radiative level is represented using the Born cross section

¹ W_R can not explicitly be searched at $p\bar{p}$ collider since the search depends on s -channel process.

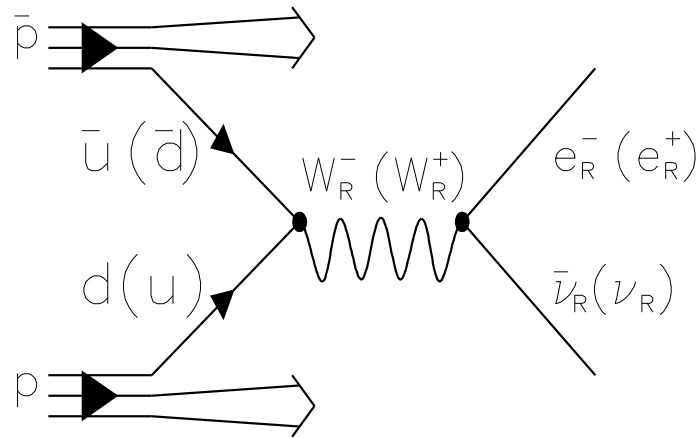


Figure 2.4: Diagram of W_R production in pp collision

as

$$\frac{d\sigma_{rad}}{d\mathbf{v}} = \int d\mathbf{v}' K(\mathbf{v}, \mathbf{v}') \frac{d\sigma_{\text{Born}}}{d\mathbf{v}'}, \quad (2.17)$$

where \mathbf{v} and \mathbf{v}' are two-dimensional vectors representing the kinematic variables (Q^2, x) . The $K(\mathbf{v}, \mathbf{v}')$ is the radiative kernel to change the phase space from \mathbf{v}' to \mathbf{v} . The calculation is implemented in DJANGO as discussed in Section 7.5.

Chapter 3

HERA and the ZEUS detector

3.1 The HERA collider

The HERA (Hadron Electron Ring Accelerator) is the unique lepton-proton collider. It was built at the DESY (Deutsches Elektronen Synchrotron) in Hamburg, Germany, and has been in operation since 1992. Figure 3.1 shows the layout of the accelerator. The circumference of the HERA is about 6.3 km. There are four experimental complex halls at HERA. Among them, two lepton-proton colliding experiments are H1 (North Hall) and ZEUS (South Hall). The others are HERMES (East Hall) and HERA-B (West Hall) which are fixed-target experiments for studies on the nucleon spin with the longitudinally polarised lepton and for studies on the B meson with the proton beam, respectively.

The HERA operated with positrons of energy 27.5 GeV and protons of energy 820 GeV from 1994 until 1997. Between 1998 and earlier 1999 electrons of energy 27.5 GeV and protons of energy 920 GeV were used. In later 1999 electron beam was switched to positron beam again and ran until 2000 (called HERA I). In 2001 the accelerator was upgraded to HERA II aiming for higher luminosity and experiments with longitudinally polarised lepton beam [13]. In Table 3.1, design parameters for HERA I and HERA II were summarised. In addition to the modest increase of the beam currents, the beam spot size is much reduced than HERA I. To achieve the high luminosity, new superconducting magnets were installed inside the experimental detectors.

The lepton beam in a ring accelerator is transversely polarised by emitting synchrotron radiation known as Sokolov-Ternov effect [14]. To obtain the longitudinally polarised positron beam, four 90° spin rotators were installed in the HERA ring. They were located in front and in the rear of H1 and ZEUS as shown in Figure 3.2. The transverse polarisation of positron is rotated to the longitudinal polarisation before collisions, then the polarisation is reversed after collisions. The HERA II

experiments started in the fall of 2003 using the longitudinally polarised positron beam. The ZEUS taken polarisation and luminosity are summarised in Table 3.2. Figure 3.3 shows the integrated luminosity and polarisation delivered by HERA I and HERA II. HERA II has delivered a day's luminosity more than HERA I.

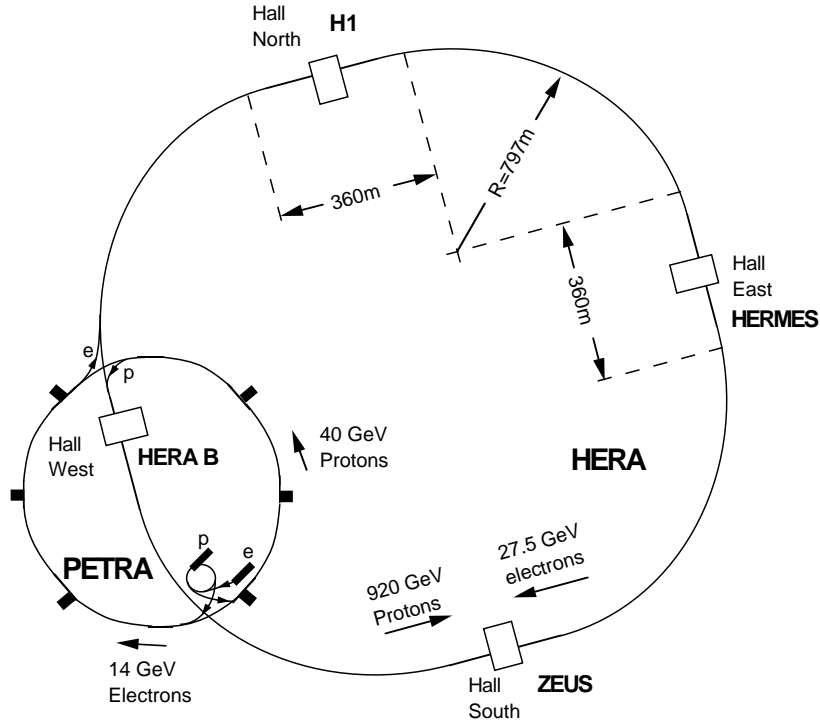


Figure 3.1: Layout of the HERA collider

3.2 The ZEUS detector

In the high energy experiment with a large accelerator as HERA, many particles with various characteristics are produced in the final states. The ZEUS detector [17] consists of the several subdetector components with different purposes to measure particles produced in the interaction point. It covers 99.7% of 4π solid angle around the interaction point of e^+p collisions. Figure 3.4 and 3.5 are the layout view of ZEUS detector.

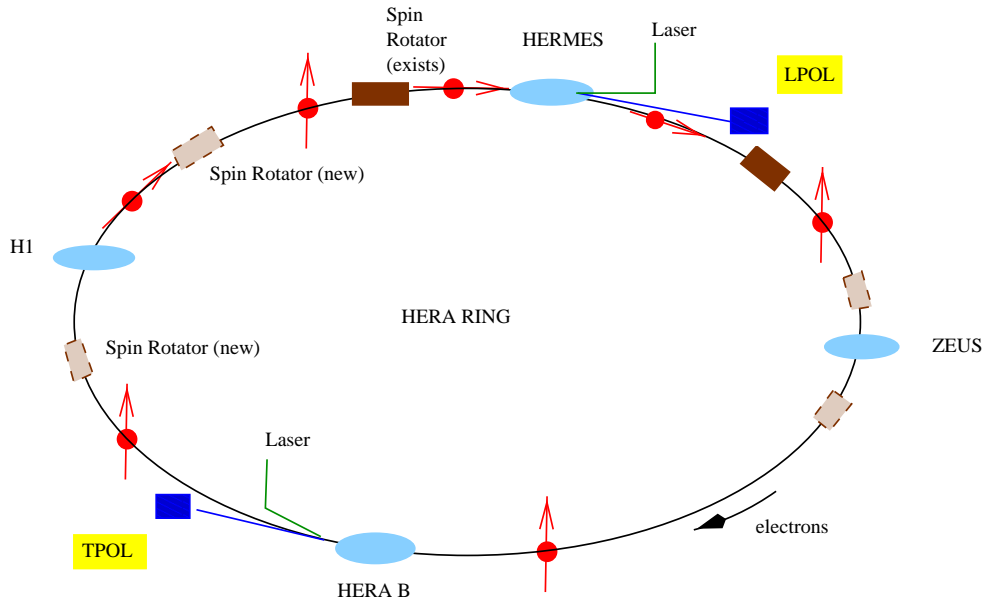


Figure 3.2: Experiments on HERA and spin rotators

Parameter	HERA I		HERA II	
	e-Beam	P-Beam	e-Beam	P-Beam
Nominal energy	27.5 GeV	920 GeV	27.5 GeV	920 GeV
Centre of mass energy	318 GeV		318 GeV	
Luminosity	$1.78 \times 10^{31} \text{ cm}^{-2} \text{ s}^{-1}$		$7.00 \times 10^{31} \text{ cm}^{-2} \text{ s}^{-1}$	
Beam spot size $\sigma_x \times \sigma_y$	187×50	187×50	112×30	112×30
Particle current	50 mA	100 mA	58 mA	140 mA
Particles per bunch	3.5×10^{10}	1.0×10^{11}	3.5×10^{10}	1.0×10^{11}
bunch crossing time	96 ns		96 ns	
polarisation rise-time	-		30 min.	

Table 3.1: HERA machine parameters

data	P (%)	\mathcal{L} (pb^{-1})
e^+p	+32.6	22.7
e^-p	-40.2	16.4

Table 3.2: Summary of HERA delivered luminosity and polarisation at HERA II

The definition of the coordinate system used in the ZEUS experiment is as follows: the positive z direction is defined as the direction which the proton beam runs, referred also to as the 'forward direction'. The positive x direction is defined as the

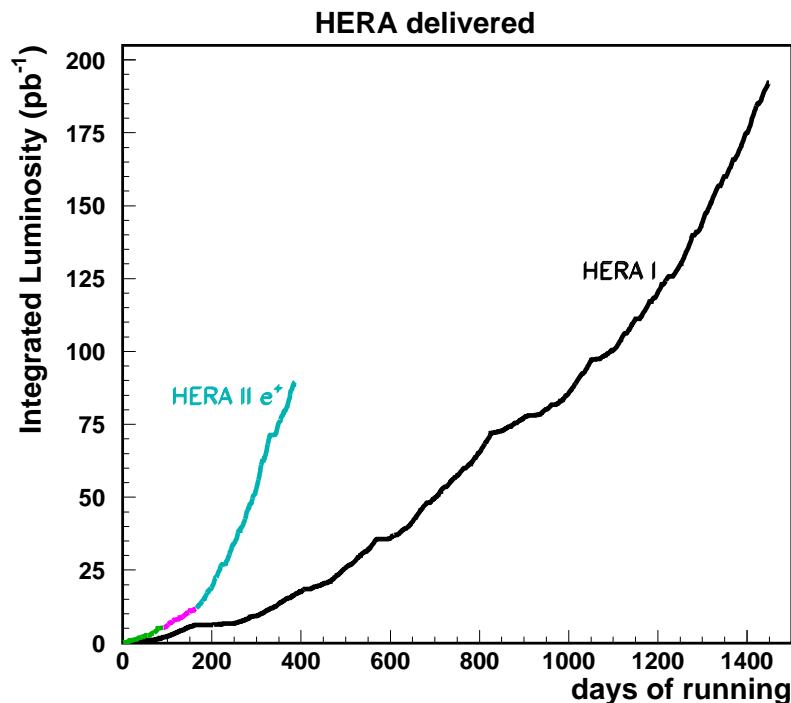


Figure 3.3: Integrated luminosity delivered at HERA I and HERA II

horizontal direction pointing to the centre of the HERA ring. The y direction is determined to correspond with Cartesian coordinate system. The polar angle θ is measured with respect to the positive z axis. The azimuthal angle ϕ is measured with respect to the positive x axis in the x - y plane.

The tracking system consists of the Micro Vertex Detector (MVD), the Central Tracking Detector (CTD), the Forward Tracking Detector (FTD) and the Rear Tracking Detector (RTD). A super conducting solenoidal magnet (SOLENOID) provides the magnetic field of 1.43 T to the CTD. The tracking system is surrounded by the Uranium Scintillator calorimeter (CAL) and the Backing calorimeter (BAC). The Muon chamber (MUON) is located at outermost of the ZEUS detector and is split into three regions, forward (FMUON), barrel (BMUON) and rear (RMUON). Small plastic scintillator counters (C5), small angle rear tracker (SRTD) and Vetowall are used to reject the background due to the proton beam-gas. The Veto Wall detector is situated at about 7.5 m upstream from interaction point. The luminosity monitor (LUMI) was also upgraded together with HERA and installed at $z = -107$ m.

In the rest of this section, the detectors which have the important role in this analysis are described.

Overview of the ZEUS Detector
(longitudinal cut)

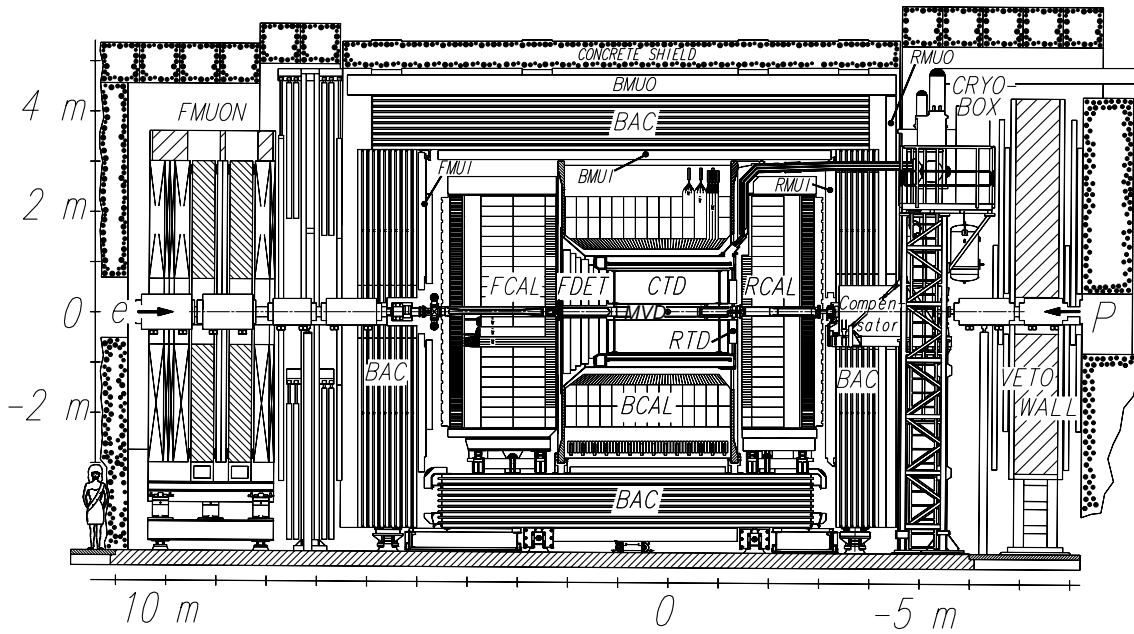


Figure 3.4: Layout (r-z view) of ZEUS detector

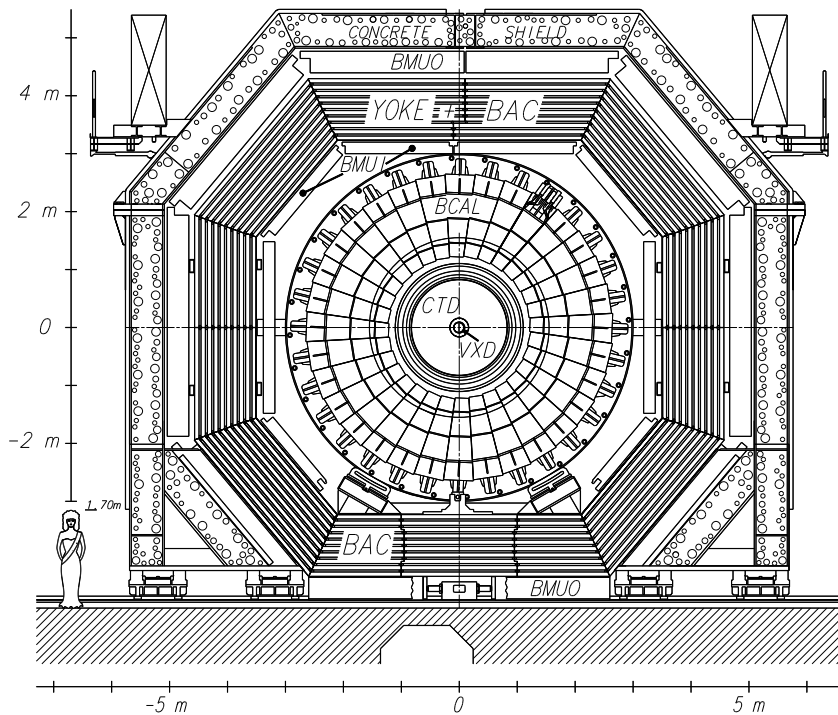


Figure 3.5: Layout (x-y view) of ZEUS detector

3.2.1 Central Tracking Detector (CTD)

The central tracking detector (CTD) [18] is a cylindrical drift chamber operated in magnetic field of 1.43T. The radii of inner and outer are 18.2 and 89.4 cm, respectively. The length in z direction is 241 cm. The CTD consists of 72 cylindrical layers arranged in 9 superlayers. One octant of CTD is shown in Figure 3.6. The superlayers are numbered from innermost to outermost. The gas mixture used in the CTD is Ar(90 %), CO₂ (8 %) and ethane (2 %). The CTD has a Lorentz angle of 45° due to the high magnetic field; the wire plane is rotated by 45° with respect to the radial direction to make the drift direction perpendicular to the wire plane. Wires in superlayers with even numbers have stereo angle of $\pm 5^\circ$ to measure the z position.

The position resolution in r - ϕ plane is 100 – 120 μm and in z -direction is 1.4 mm. The resolution of the CTD for a charged particle going through all superlayers is parameterised as

$$\frac{\sigma(p_T)}{p_T} = 0.0058 p_T \oplus 0.0065 \oplus \frac{0.0014}{p_T}, \quad (3.1)$$

where p_T is transverse momentum.

3.2.2 Uranium scintillator calorimeter (CAL)

ZEUS needs to have a good resolution both for electro-magnetic and hadronic calorimetries. In particular, the good resolution for hadronic energy measurement give a benefit to reconstruct the kinematic variables of CC DIS events as later mentioned in Chapter 5. The ZEUS selected a sandwich-type calorimeter with depleted Uranium(DU) as the absorber and plastic scintillator for active material. The thickness of DU and scintillator plates in one layer is 3.3 mm and 2.6 mm, respectively. The uranium scintillator calorimeter (CAL) [19] is nearly hermetic; covering 99.7 % of solid-angle coverage.

The CAL is mechanically divided into 3 regions, forward(FCAL), barrel(BCAL) and rear(RCAL) as shown in Figure 3.7. The depth of the FCAL, BCAL and RCAL are 7λ , 5λ and 4λ , respectively, where λ is the interaction length. The final state particles are boosted into the forward region due to the asymmetric beam energy, so that the FCAL is thicker. The surfaces of FCAL and RCAL are located at $z = +226.0$ cm and $z = -148.0$ cm, respectively.

Each part of the CAL consists of 24(32) modules for FCAL and RCAL (BCAL). Each module consists of towers. Figure 3.8 shows the one view of module in FCAL.

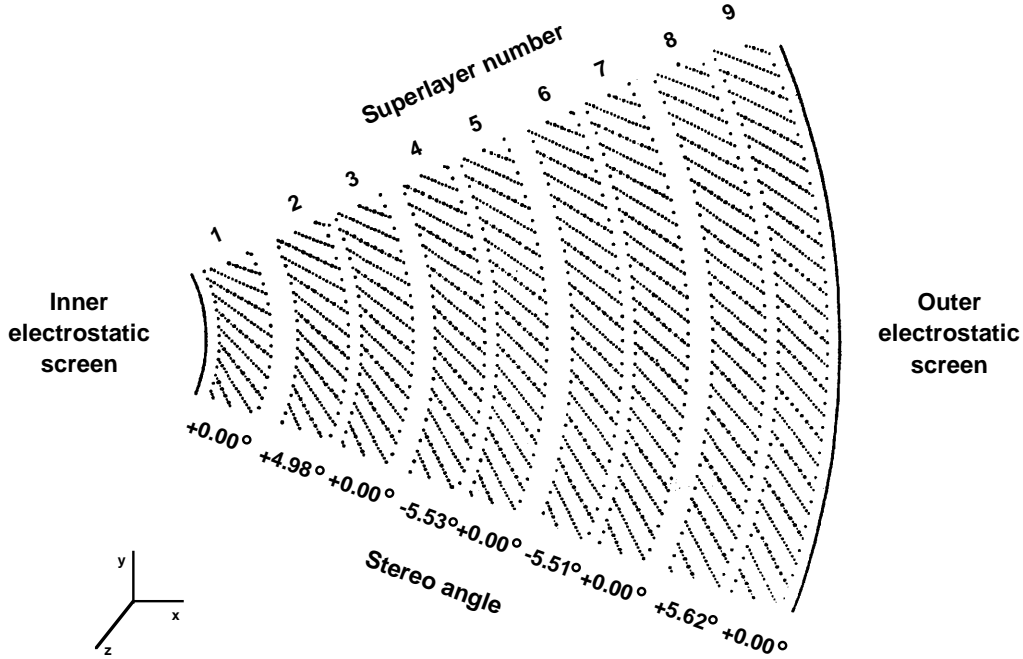


Figure 3.6: CTD wires arrangement

The face size of tower is $20 \times 20 \text{ cm}^2$. One tower is longitudinally divided into 3, a electromagnetic section (EMC) and two hadronic sections (HAC1 and HAC2), for FCAL and BCAL, and an EMC and a HAC for RCAL. The thickness of the EMC section and one HAC section is $\simeq 1\lambda$ and $\simeq 3$ (2 in RCAL) λ , respectively. One EMC tower is further divided into 4 (2 for RCAL) cells horizontally in order to have finer granularity for electro-magnetic particles.

The light from the scintillator is transmitted to wave length shifter(WLS) plates attached on each side of a cell. In the WLS plates, the light from the scintillator is absorbed and re-transmitted to a photomultiplier (PMT). A cell is therefore readout by 2 PMTs.

The energy resolutions for electrons and hadrons were measured at the test beam as

$$\frac{\sigma(E)}{E} = \frac{18\%}{\sqrt{E}} \oplus 1\%, \quad \text{for electrons,}$$

$$\frac{\sigma(E)}{E} = \frac{35\%}{\sqrt{E}} \oplus 2\%, \quad \text{for hadrons,}$$

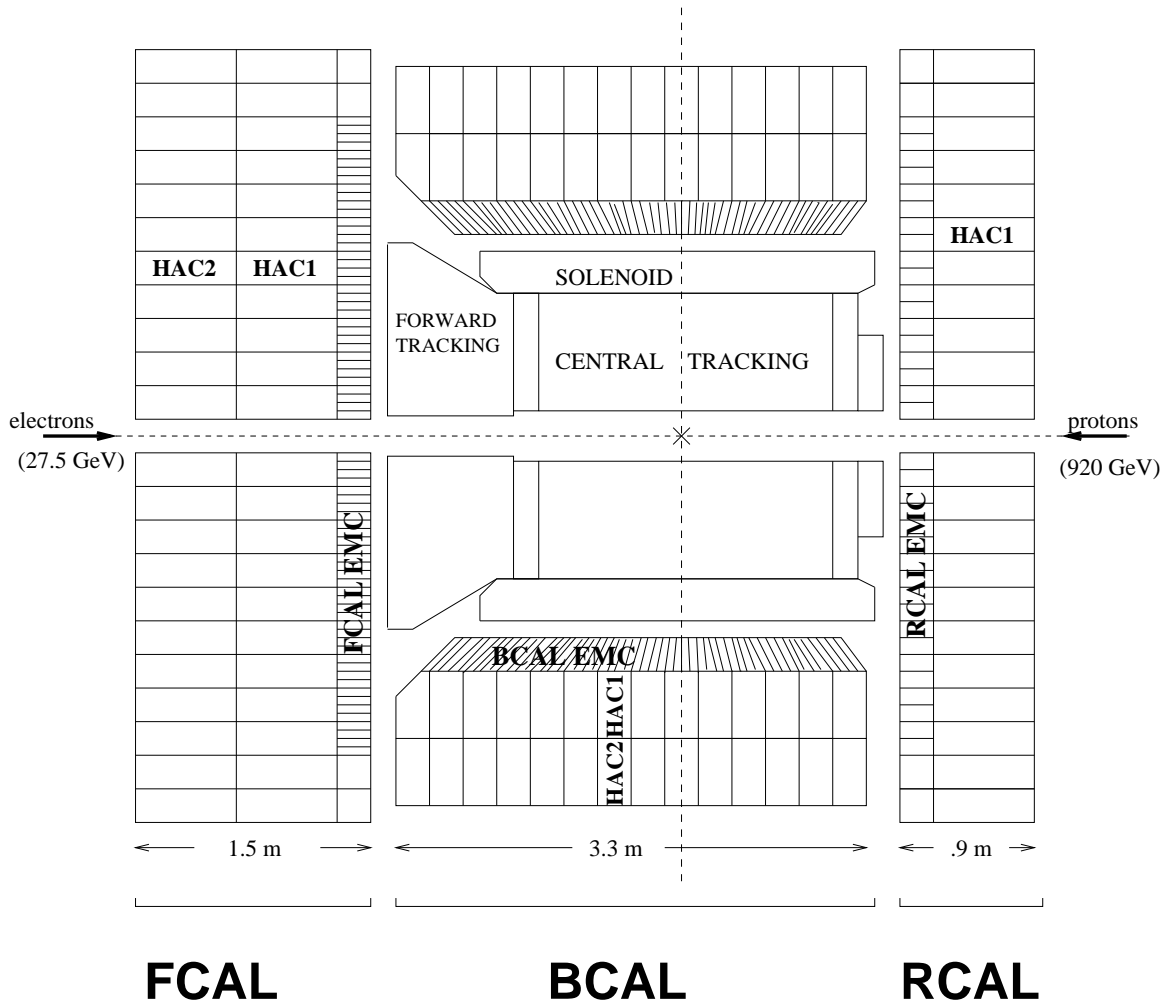


Figure 3.7: A view of the ZEUS calorimeter

where E is an energy in GeV. The ratio of the response to electrons and to hadrons was found to be

$$e/h = 1.00 \pm 0.03,$$

for particles with energy greater than 3 GeV.

3.2.3 Luminosity Monitor

The electron-proton bremsstrahlung process, $ep \rightarrow e'\gamma p$, is used for the luminosity measurement at ZEUS. The luminosity is measured by counting high energy

bremsstrahlung photons. Figure 3.9 shows ZEUS luminosity monitor system[20]. It has 2 calorimeters; a photon calorimeter and an electron calorimeter.

The photon calorimeter is located at $z = -107$ m and at $\theta = 180^\circ$ as shown in Figure 3.9. The photons travel through the proton beam pipe and enter the photon calorimeter. It is a lead-scintillator sampling calorimeter. After the HERA II, in order to protect the calorimeter from the harsh radiation from the synchrotron radiation, the thicker carbon absorber was installed in front of the calorimeter[21]. The energy resolution of the calorimeter became worse due to the absorber. To recover the energy resolution, the two Aerogel-Cherenkov detectors [22] were installed as shown Figure 3.10.

The luminosity (\mathcal{L}) is determined as

$$L = R/\sigma, \quad (3.2)$$

where σ is the theoretical cross section of the bremsstrahlung photon and R is the photon counting rate after background subtraction. The background is mainly from the bremsstrahlung with the residual gas in the beam-pipe, and is estimated from the rate using the non-colliding positron bunches (pilot bunch). R is calculated as

$$R = R_{total} - kR_{pilot}, \quad (3.3)$$

$$k = I^{coll}/I^{pilot}, \quad (3.4)$$

where I^{coll} and I^{pilot} are the total electron current in the colliding bunch and that in the non-colliding bunch, respectively.

On the other hand, the electron is detected by the electron calorimeter located at $z = -25$ m. The information of the electron calorimeter is used to check the systematics on the luminosity measurement.

The systematic uncertainties mainly come from geometrical acceptance (2 - 4 %) and from the event pile-up and energy calibration(2 %) on the measurement of luminosity. Total uncertainty is ~ 5 %.

3.3 C5 counter

Major beam related backgrounds are from the interaction between the proton beam and the residual gas inside the beampipe. C5 counter is small plastic scintil-

lator counter surrounded the beam-pipe and located at -126 cm from the origin of the ZEUS coordinate axes. The produced particles from the beam-gas interaction at upstream are hit to the C5 counters. Since C5 is located upstream, the hit timing of the background is earlier than the hit from the e^+p collisions. Using this time difference, the background events are separated.

3.4 ZEUS data acquisition and trigger system

The ZEUS trigger system[23] consists of three levels, the first level trigger(FLT), the second level trigger(SLT) and the third level trigger(TLT). The diagram of the DAQ system with the trigger is shown in Figure 3.11. The ZEUS trigger system needs to confront with the short bunch crossing time (96 ns) and a large background from the beam-gas events of ~ 100 kHz.

3.4.1 First Level Trigger (FLT)

The first level trigger (FLT) has the task to reduce a trigger rate from the beam crossing rate of 10 MHz to 1 kHz by rejecting most of non- ep backgrounds such as the beam-gas and beam-halo events. The FLT consists of the global first level trigger (GFLT) and the first level component triggers. Each component trigger produces trigger quantities in the pipelined hardware processors and sends them to the GFLT. The GFLT has 64 bits for the output (called 64 slots). Each slot gives yes/no decisions based on the information of FLT components such as CAL and CTD. If the condition of a event corresponds to at least one of 64 slots, the positive decision is sent to the component readout system 46 crossings after the interaction.

In the component readout all data is stored in analog- or digital pipelines for every bunch crossing at 96 ns intervals. Receiving the FLT decision, the component select the corresponding data from the pipelines.

3.4.2 Second Level Trigger (SLT)

The second level trigger (SLT) consists of the global second level trigger(GSLT) and the SLT components. At SLT, more accurate calculation than FLT can be performed by CPUs using the readout data. The GSLT has the tasks to combine the results from SLT components and to make result if the event is taken, or not. The SLT is designed to reduce the rate from 1 kHz in the FLT level to 100 Hz. After a positive decision of the SLT data are sent to the event builder (EVB).

3.4.3 Third Level Trigger (TLT)

The third level trigger (TLT) is a computer farm. At the TLT level, the information of all components and the code of offline are usable for the event reconstruction to improve on the SLT selection. The TLT has a task to select the interesting physics events. The rate after the TLT is to about 3 Hz.

3.5 Polarimeter

The degree of the polarisation is measured by two polarimeters, the Transverse Polarimeter (TPOL)[15] and the Longitudinal Polarimeter(LPOL)[16]. The method of the polarisation measurement at the HERA is based on the Compton scattering of circularly polarised photons from pulsed high intensity laser beam.

The differential cross section of the Compton scattering of circularly polarised photons off polarised positions can be written in the laboratory frame as

$$\frac{d\sigma^2}{dE_\gamma d\phi} = \Sigma_0(E) + S_3(P_Y \Sigma_{2Y}(E) \sin \phi + P_Z \Sigma_{2Z}(E)), \quad (3.5)$$

where S_3 is circular laser polarisation (+ for left-handed and – for right-handed laser photons). P_Y and P_Z are transverse and longitudinal polarisation of positrons. $\Sigma_{0(1,2Y,2Z)}$ are the factors which depend only on the scattered photon's energy. Therefore the difference of the cross section between the right and left-handed laser light scattered off polarised positrons can be written as

$$\frac{d\sigma^2}{dE_\gamma d\phi}(R - L) = 2(C_T + C_L), \quad (3.6)$$

$$C_T = P_Y \Sigma_{2Y}(E) \sin \phi, \quad (3.7)$$

$$C_L = P_Z \Sigma_{2Z}(E), \quad (3.8)$$

where C_L corresponds to the average energy asymmetry for the longitudinally polarised positrons, and C_T denotes the spatial asymmetry for the transversely polarised positrons. The LPOL measures the C_L and the TPOL C_T .

3.5.1 Transverse polarimeter (TPOL)

TPOL is located in the HERA-B experimental hall as shown in Figure 3.2, where the positron is transversely polarised. The overview of the TPOL is shown in Figure 3.12. A A_r^+ laser, which has a wavelength of 514.5 nm and the polarisation of up to 99.5%, is collided with positrons at interaction point(IP) with the crossing angle of 3.1 mrad. The back scattered photons produced at IP travel along the positron beam pipe and are separated from the positron beam with a magnet at the point of 60 m from the IP.

TPOL calorimeter is located at 65 m away from the IP. The calorimeter which is sandwiched of the tungsten(6.2 mm) and scintillator(2.6 mm), is separated into the upper and lower halves. The calorimeter can measure the vertical position of the incoming photon (y) through the signal asymmetry in the two CAL (η),

$$\eta = \frac{E_U - E_D}{E_U + E_D}, \quad (3.9)$$

where E_U and E_D are the energies of the upper and lower halves, respectively. The polarisation is given by,

$$P = \int dE_\gamma d\phi \frac{C_T}{2 \sum_{2Y}(E) \sin \phi} \frac{d\sigma^2}{dE_\gamma d\phi} (R - L) \quad (3.10)$$

$$= \frac{1}{A} (\langle \eta_L \rangle - \langle \eta_R \rangle) \quad (3.11)$$

where A is analysing power which convolutes the response of the calorimeter.

The exact relation between η and y (called ' $\eta - y$ transformation') depends on the transverse shower development in the calorimeter and was measured at test beam. But the uncertainty gives the largest contribution to the systematic error. To reduce the uncertainty, the Pb pre-radiator, silicon strip detector and the scintillating fibre detector have been installed in front of the calorimeter as shown in Figure 3.13. The photons produce the pair creation of e^+e^- in the pre-radiator ($\sim 1 X_0$). The silicon detector provides a in-situ calibration of the $\eta - y$ transformation by giving a direct measurement of position (y). The scintillating fibre detector is used to calibrate y position of the silicon detector and to monitor the radiation damage of the silicon strip detector due to the synchrotron radiation.

3.5.2 Longitudinal polarimeter (LPOL)

LPOL is located near HERMES experiment as shown in Figure 3.2. The overview of LPOL is shown in Figure 3.14. The laser beam of Nd : YAG (Neodim:Yttrium Aluminium Garnet) is used in LPOL. The back scattered photons travel about 54 m to the calorimeter. LPOL calorimeter consists of four optically isolated $\text{NaBi}(\text{WO}_4)_2$ crystals. The two lead pre-shower were installed in front of the calorimeter. Compton photons generate a electromagnetic shower in the lead pre-shower and the crystals. The total energy from the photons deposits in the four crystals. The polarisation is given by the formula using energy asymmetry and analysing power A as

$$P = \frac{1}{A} \frac{\langle E_L \rangle - \langle E_R \rangle}{\langle E_L \rangle + \langle E_R \rangle}, \quad (3.12)$$

$$(3.13)$$

where $\langle E_L \rangle$ and $\langle E_R \rangle$ denote the average energies of the left- and right-handed laser in the calorimeter. The analysing power convolutes the energy resolution.

3.5.3 Polarisation for this analysis

The two polarimeters measure the polarisation per minute as shown in Figure 3.15. The value of polarisation for this analysis is extracted by re-weighting the measured polarisation with the luminosity. The polarisation values from the autumn of 2003 until summer of 2004 is shown in Figure 3.16. The average positive and negative polarisation of this period are +32.6 % and -40.2 %, respectively. And the systematic uncertainty ($\delta P/P$) from LPOL and TPOL are 1.6 – 5%¹ and 3.5%, respectively.

¹The calorimeter of LPOL was not usable since June of 2004, after radiation damage. The systematic uncertainty in this period increased to 5 %.

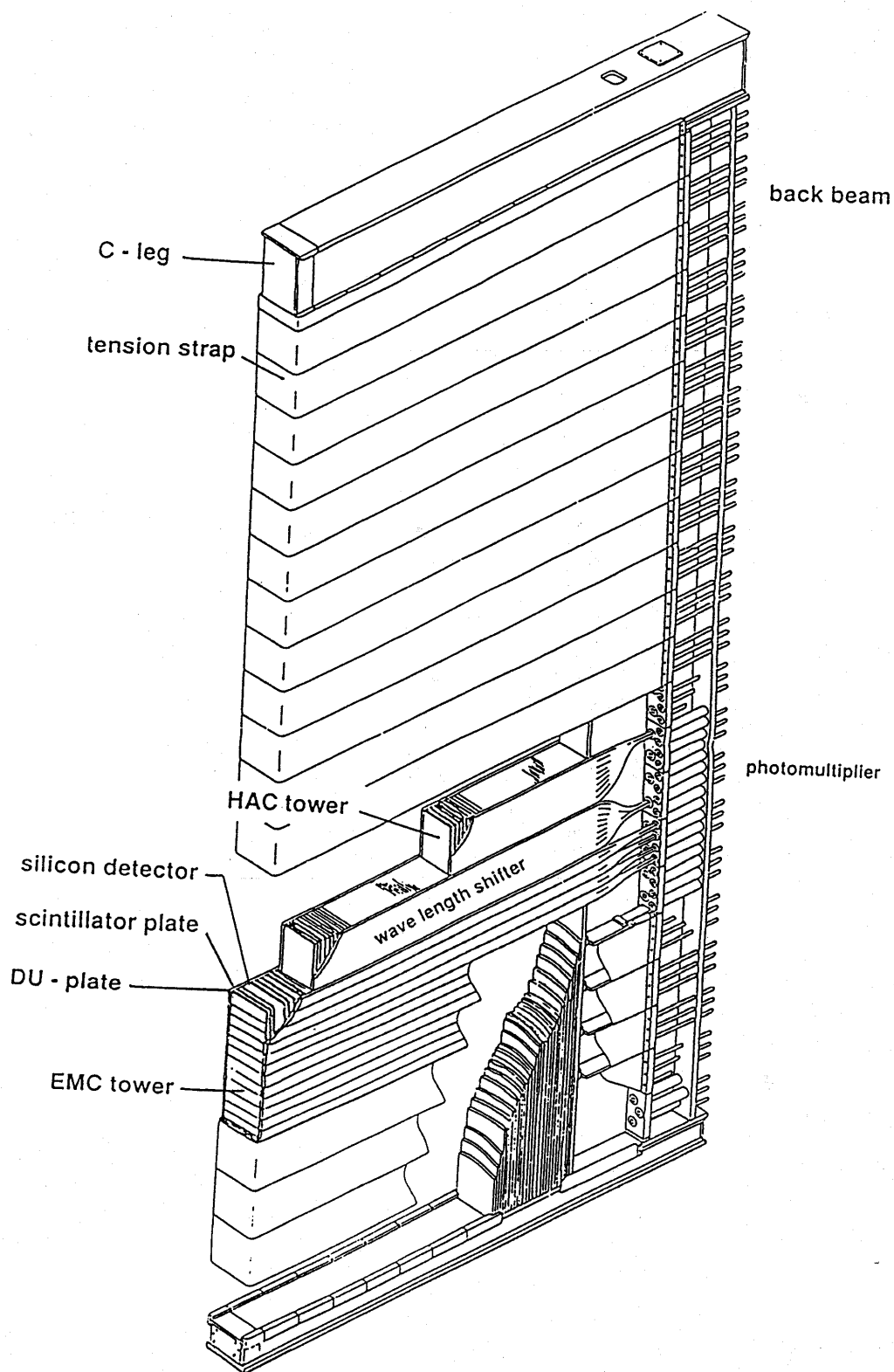


Figure 3.8: A module of the ZEUS calorimeter

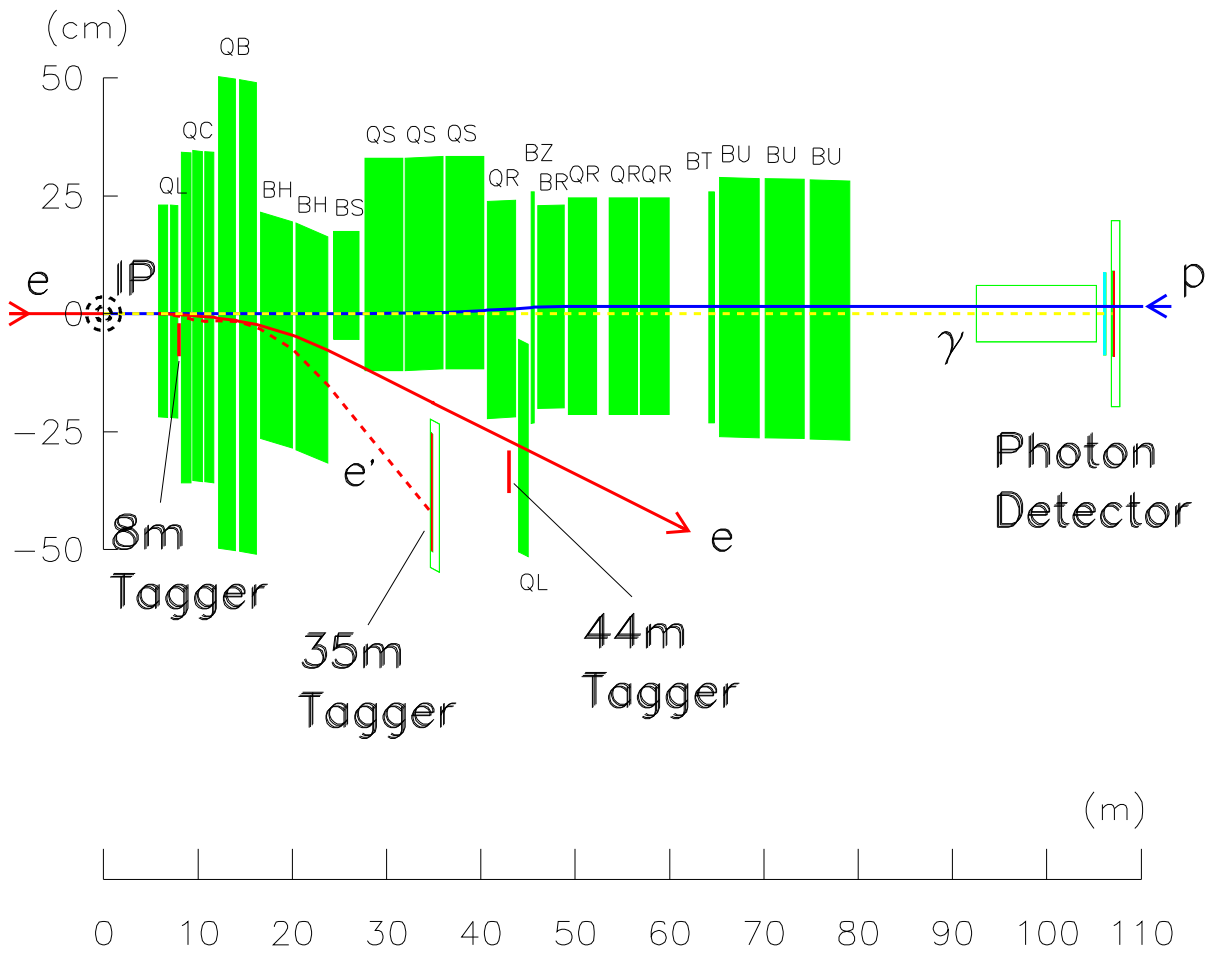


Figure 3.9: Luminosity detectors

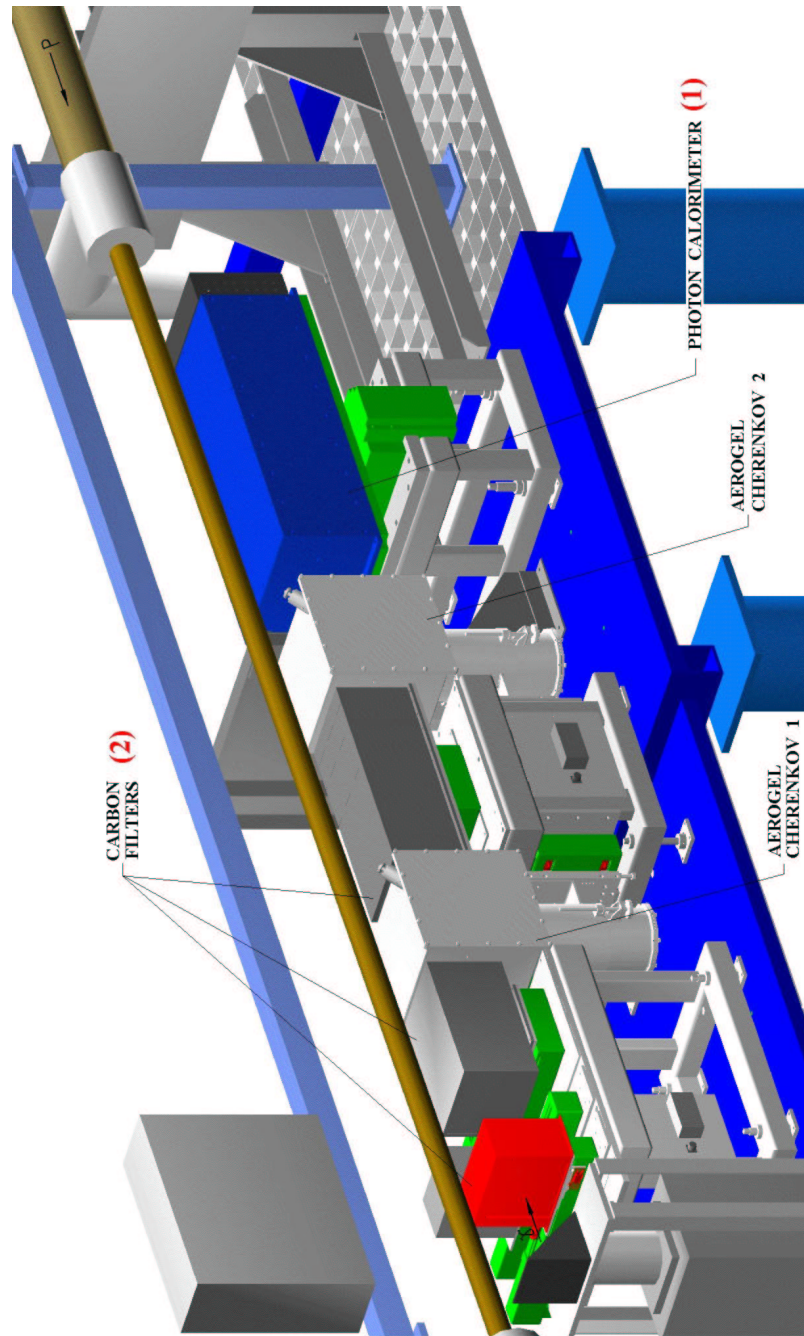


Figure 3.10: Luminosity monitors

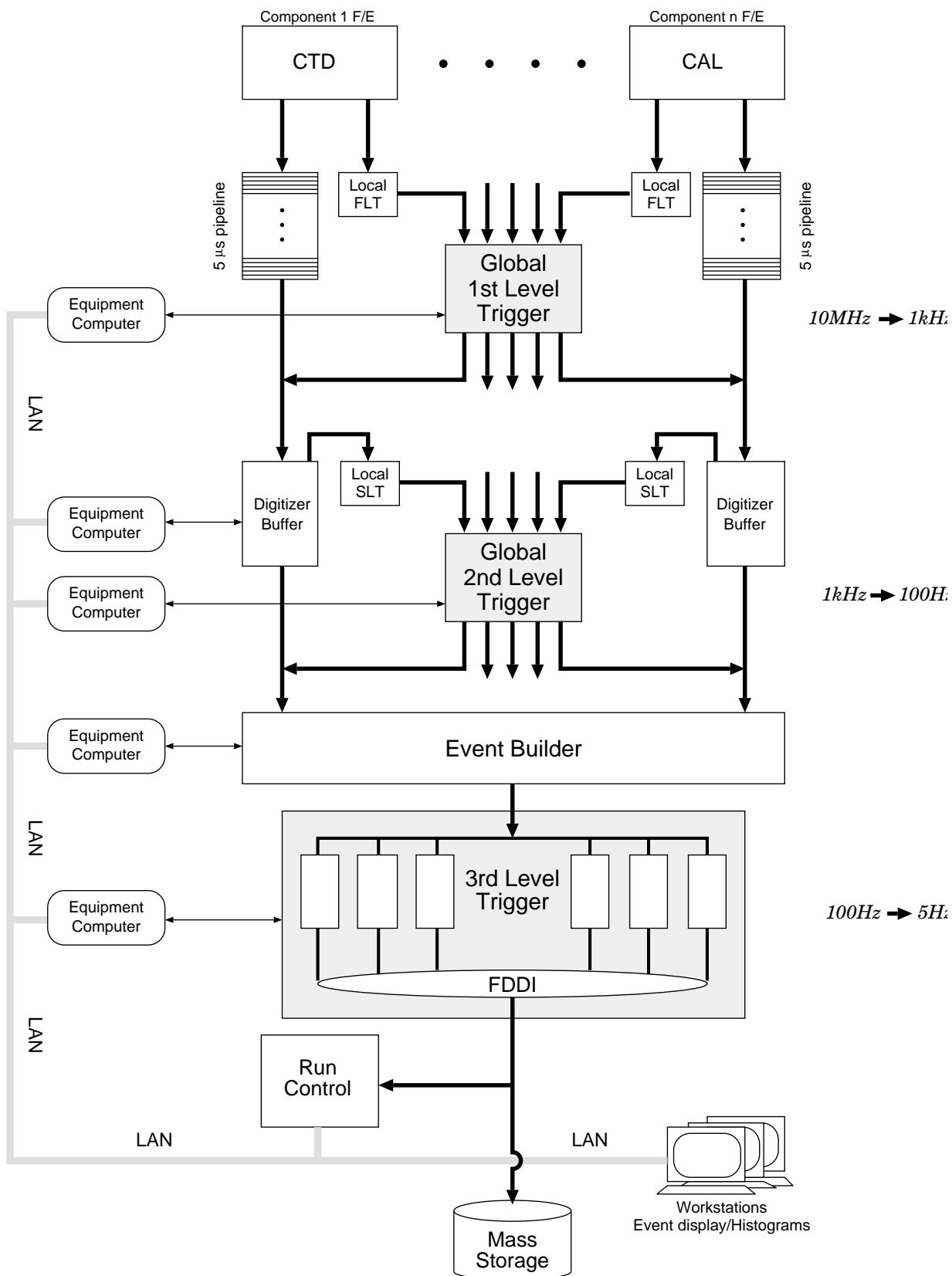
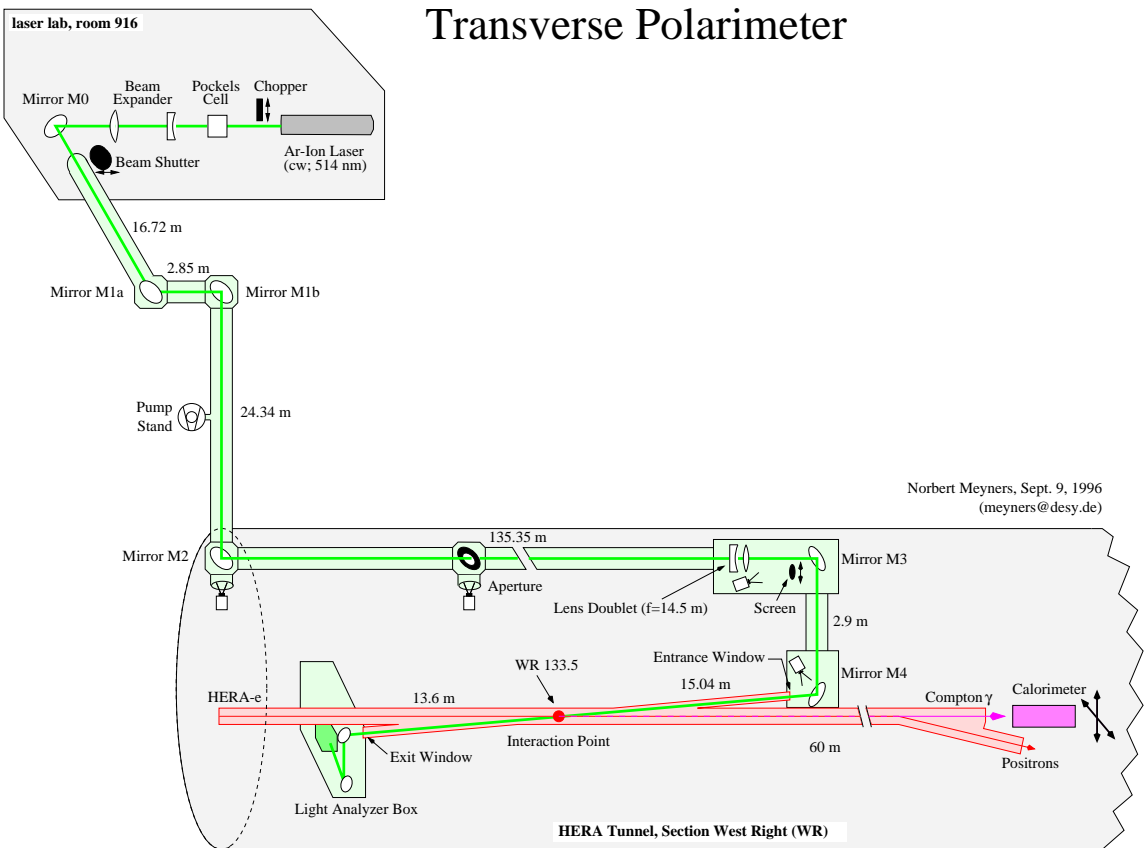



Figure 3.11: Schematic diagram of the ZEUS trigger and DAQ system



Marc Beckmann  1998

10

Figure 3.12: Transverse Polarimeter

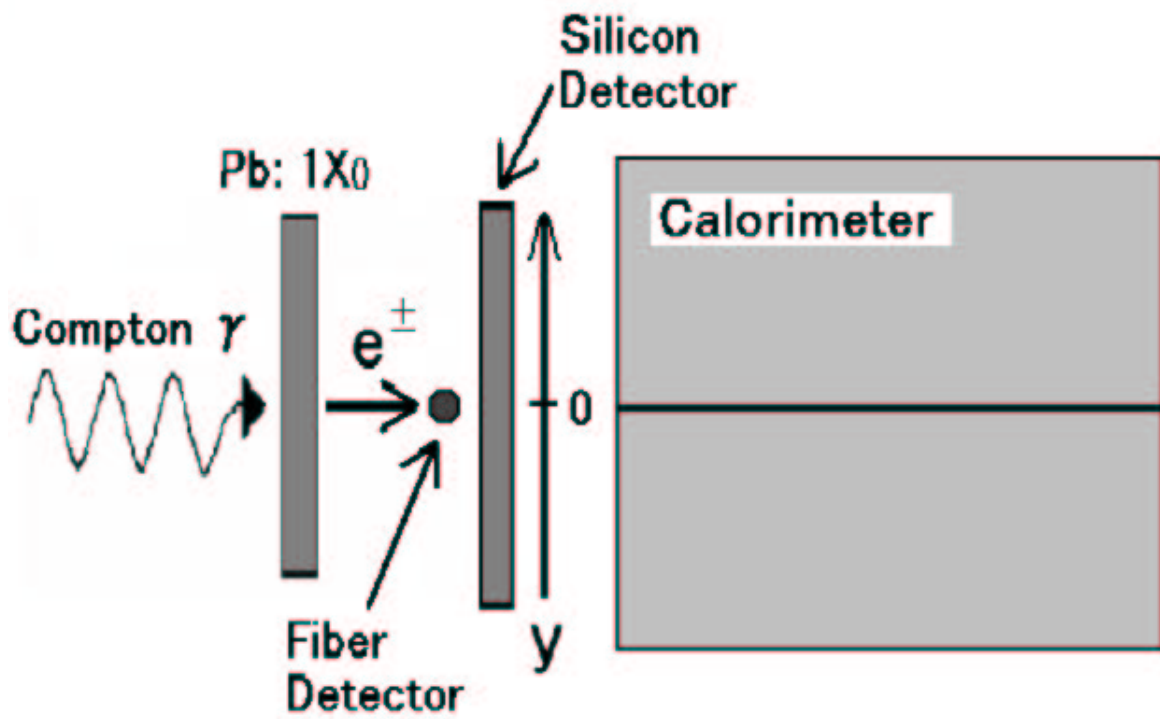


Figure 3.13: Calorimeter, Silicon strip detector and Scintillating fibre detector in the transverse polarimeter.

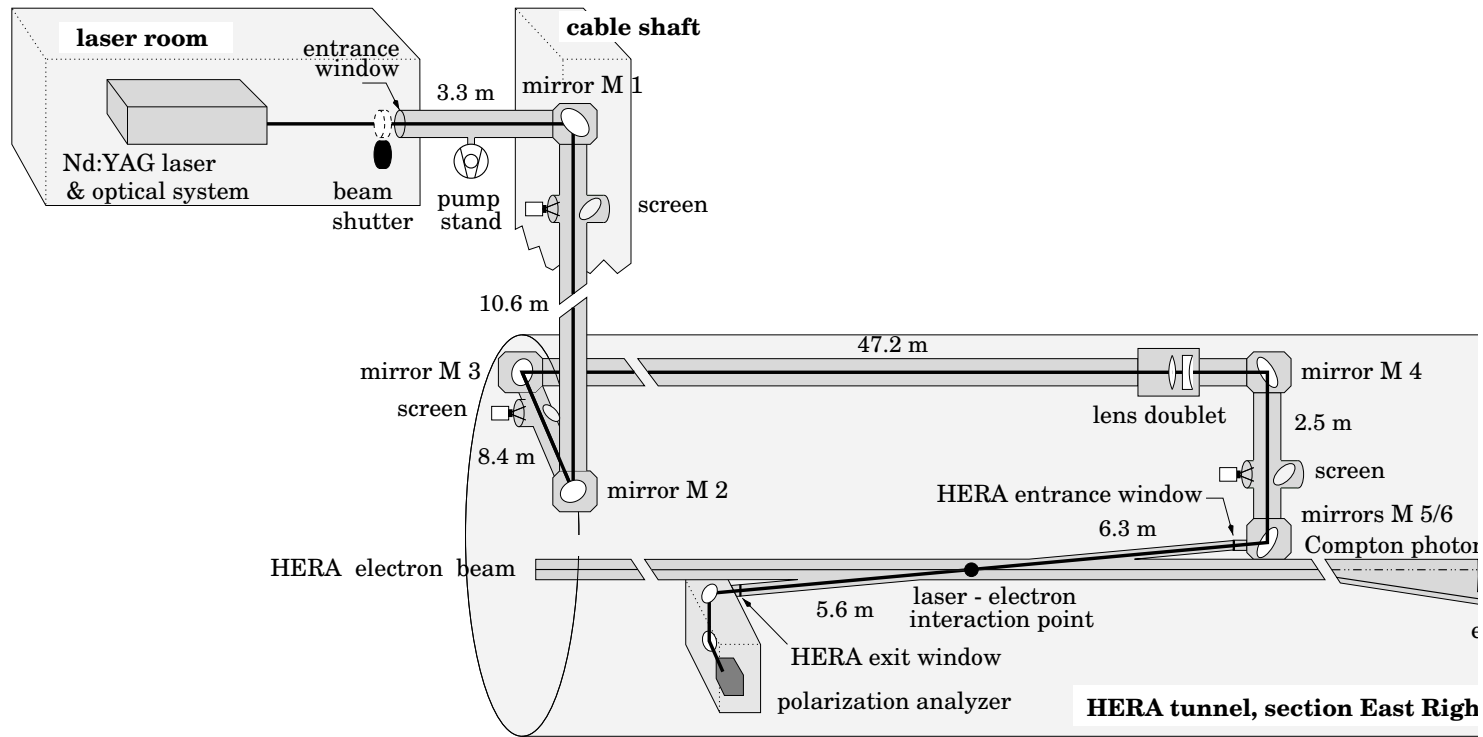


Figure 3.14: Longitudinal Polarimeter

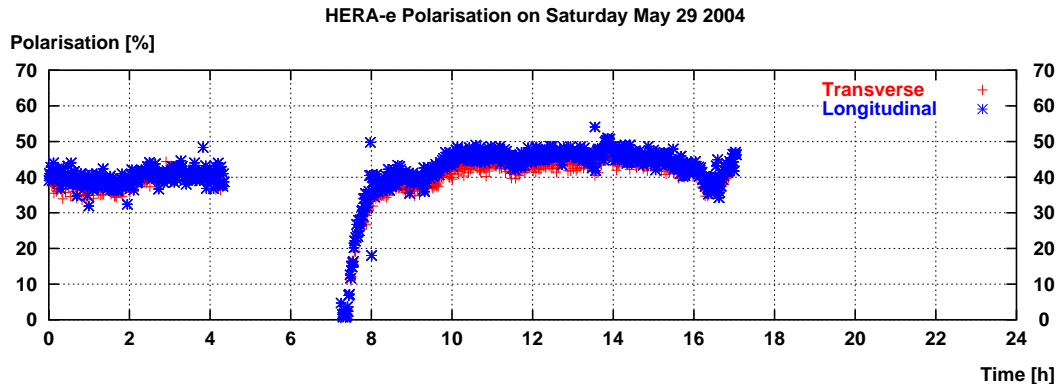


Figure 3.15: polarisation of the positron beam in one fill

Average HERA polarisation (longitudinal polarimeter)

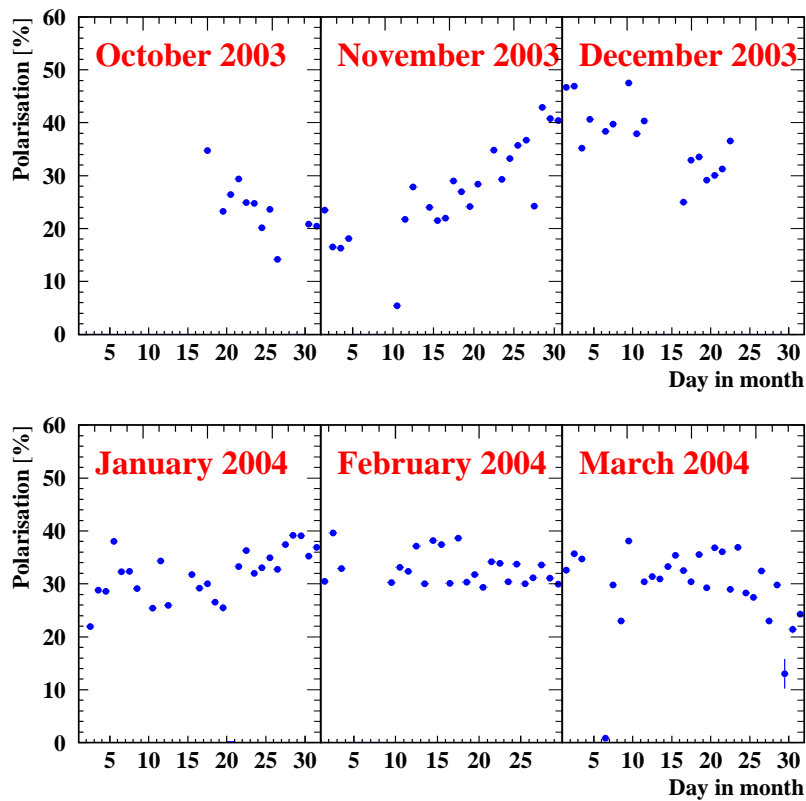


Figure 3.16: HERA average positron polarisation for each day

Chapter 4

Monte Carlo simulation (MC)

In order to measure the cross section, we have to understand well the detector response, i.e its resolution and acceptance. Since it is difficult directly to estimate them from the real data, the Monte Carlo simulation (MC) is used. The MC is also used to estimate the background.

The generated MC events go through a detector simulation and trigger simulation. They are reconstructed using the same offline reconstruction codes as used for the real data.

4.1 DIS Event Generator

e^+p DIS MC events are generated using the program DJANGO1.3[7], which is an interface of two kinds of programs, the electro-weak part (HERACLES4.6.3[8]) and the hadron part (LEPTO6.5.1[9] or ARIADNE[10]). HERACLES handles the initial state radiation from the incoming positron, propagator corrections, and two boson exchange processes.

The leading order parton level process is $V^*q \rightarrow q'$, where V^* denotes a virtual vector boson γ/Z or W , and q and q' are a quark and the scattered quark, respectively. This hard scattering process is generated according to the cross section prediction with a parton density function (CTEQ5D is used in this analysis) by the LEPTO or ARIADNE.

The QCD cascade is also simulated in LEPTO. The MEPS (Matrix Elements and Parton Shower) model is implemented. The first order QCD processes such as the QCD Compton process (QCDC), $V^*q \rightarrow qg$ and the boson gluon fusion process (BGF), $V^*g \rightarrow q\bar{q}$ are taken into account in the matrix element (ME). The QCD effects in the higher order such as the processes $q \rightarrow qg$, $g \rightarrow gg$, $g \rightarrow q\bar{q}$, are taken into account in the parton shower (PS) model.

In the ARIADNE, the Colour Dipole Model (CDM) is adopted instead of the MEPS.

The struck quark and parton remnant are described as the colour dipole which can radiate gluon.

4.2 Signal Monte Carlo

CC MC samples with the CDM and MEPS are used in this analysis. The uncertainty of the parton shower model can be estimated by comparing these two generators. Events are generated in several Q^2 regions. The list of CC MC samples are shown in Table 4.1.

MC sample	σ (pb)	N_{gen}
$Q^2 > 10 \text{ GeV}^2$	44.9	24960
$Q^2 > 100 \text{ GeV}^2$	39.7	24928
$Q^2 > 5000 \text{ GeV}^2$	3.29	14715
$Q^2 > 10000 \text{ GeV}^2$	0.706	5000
$Q^2 > 20000 \text{ GeV}^2$	0.064	4970

Table 4.1: Charged Current Monte Carlo samples; N_{gen} denotes the number of generated events.

4.3 Event generators for background processes

To estimate non-CC backgrounds, several kind of MC samples are used. They are summarised in Table 4.2.

4.3.1 Photoproduction

Photoproduction(PhP) denotes that a quasi-real photon interacts with the proton (γp interactions). Since the processes is in $Q^2 \sim 0$, normally the scattered positron escapes in the beam pipe. Ideally there is no missing transverse momentum in these processes. However, the PhP cross section is huge so that the imperfect response of the CAL and/or the missing energy from neutrino and muon from the heavy quark decays cause the potential backgrounds of the CC analysis.

Two kinds of PhP processes are involved as shown in Figure 4.1; one is the direct-PhP processes where the photon directly interacts with a parton, and the other is the resolved PhP where the photon acts as a source of partons for the hard scattering.

MC sample	Generator level cut	σ (pb)	N_{gen}
Resolved PhP	$E_T > 18 \text{ GeV}$ or $P_T > 6 \text{ GeV}$	$1.16 \cdot 10^5$	349136
	$E_T > 20 \text{ GeV}$ or $P_T > 6 \text{ GeV}$	$7.92 \cdot 10^4$	1831637
	$E_T > 30 \text{ GeV}$ or $P_T > 6 \text{ GeV}$	$1.19 \cdot 10^4$	3016182
Direct PhP	$E_T > 30 \text{ GeV}$ or $P_T > 6 \text{ GeV}$	$2.83 \cdot 10^3$	99944
NC DIS	$Q^2 > 100 \text{ GeV}$	$8.12 \cdot 10^3$	939629
W production			
$e^+ \rightarrow e^+W^+X(DIS)$		0.490	49967
$e^+ \rightarrow e^+W^+X(resolved)$		0.106	9995
$e^+ \rightarrow e^+W^-X(DIS)$		0.401	49910
$e^+ \rightarrow e^+W^-X(resolved)$		0.0874	10000

Table 4.2: Background Monte Carlo

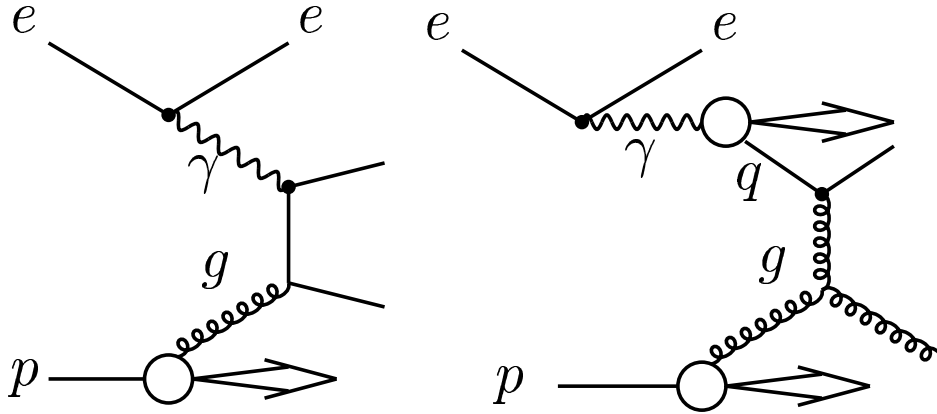


Figure 4.1: Diagrams of direct(left) and resolved(right) photoproduction

4.3.2 Neutral current DIS

NC DIS events can have a missing transverse momentum if the energy of the hadron jet or the scattered positron are not detected by the calorimeter well due to the energy resolution and the crack of the calorimeter etc. NC DIS samples generated using DJANGO.

4.3.3 Di-lepton production

A diagram for di-lepton pair production is shown in Figure 4.2. If muon pair is produced in the final state, the muons go through the calorimeter with little energy deposit. And if a lepton pair is tau pair, taus decay accompanying with ν_τ . Then

this neutrino can not be detected in the calorimeter. So di-tau process can also be background for CC DIS events. Di-muon and di-tau MC samples are generated with LPAIR[12].

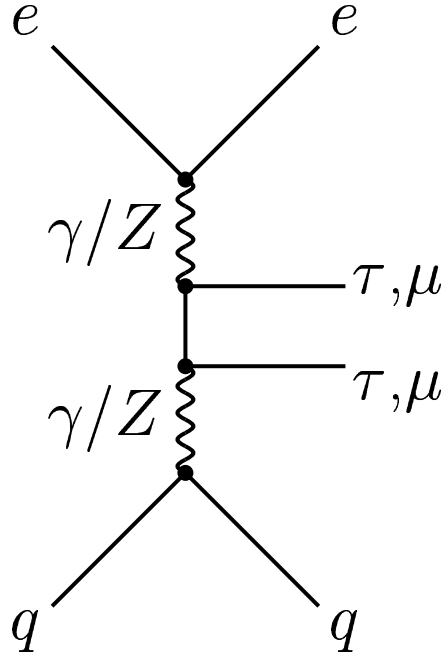


Figure 4.2: A diagram of the di-lepton process

4.3.4 W production

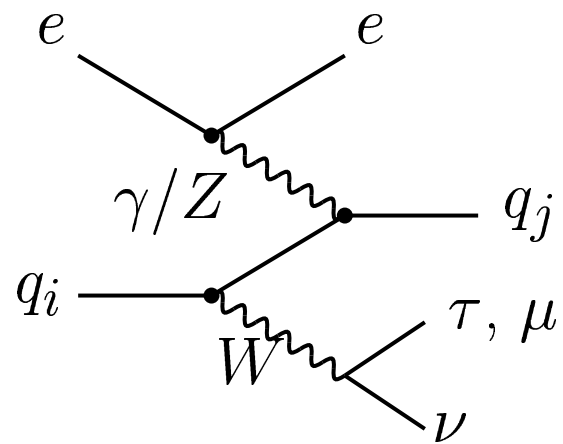
The W boson produced in the final states decays to a lepton and a neutrino. The missing transverse momentum due to the neutrino occurs in a event. There are neutral current and charged current processes in the W production as the follows,

$$e^+p \rightarrow e^+W^\pm X, \quad (4.1)$$

$$e^+p \rightarrow \nu W^\pm X, \quad (4.2)$$

where X denotes the hadronic system. The charged current process is negligible comparing to the neutral current one because of its small cross section. We consider the neutral current process which is shown in Figure.4.3 as background source against CC DIS events.

W production MC samples are generated with EPVEC[11].

Figure 4.3: A diagram of W production

Chapter 5

RECONSTRUCTION OF KINEMATICS

5.1 Reconstruction methods

There are two independent kinematic variables for inclusive DIS, such as Q^2 and x . It is possible to measure energy and angle of scattered lepton and also those of hadron system. Using these four variables, there are various kinematic reconstruction methods of Q^2 and x . Two kinematics reconstruction methods are used in this analysis; the Jacquet-Blondel method [24] and the double angle method [25]. The former is for CC DIS events and the latter is for NC DIS. In this chapter, the kinematic reconstruction methods are introduced.

5.1.1 The Jacquet-Blondel method

In the Jacquet-Blondel method, kinematic variables are reconstructed solely from the hadronic reconstruction. By summing the four momenta of all detected particles except the scattered lepton, the hadronic system $P_h = (E_h, P_{x,h}, P_{y,h}, P_{z,h})$ is calculated. The kinematic variables are determined from P_h and positron beam energy (E_e) in the following formula:

$$y_{JB} = \frac{(E - P_z)_h}{2E_e}, \quad (5.1)$$

$$Q_{JB}^2 = \frac{P_{T,h}}{1 - y_{JB}}, \quad (5.2)$$

$$x_{JB} = \frac{P_{T,h}}{s y_{JB} (1 - y_{JB})}, \quad (5.3)$$

where $P_{T,h}$ and $(E - P_z)_h$ are

$$P_{T,h} = \sqrt{P_{x,h}^2 + P_{y,h}^2}, \quad (5.4)$$

$$(E - P_z)_h \equiv E_h - P_{z,h}. \quad (5.5)$$

5.1.2 The Double Angle method

In NC events, the hadronic system and scattered positron can be detected in the ZEUS detector. For high Q^2 events, the double angle method using both of the angles of the scattered positron (θ_e) and the hadronic system (γ_h) is the most accurate method for the kinematic reconstruction. The hadronic energy, E_h and γ_h are defined as follows:

$$\cos \gamma_h \equiv \frac{P_{T,h}^2 - (E - P_z)_h^2}{P_{T,h}^2 + (E - P_z)_h^2}, \quad (5.6)$$

$$E_h \equiv \frac{P_{T,h}}{\sin \gamma_h}. \quad (5.7)$$

In the double angle method, the kinematic variables, Q^2 , x and y are determined using θ_e and γ_h as

$$Q_{DA}^2 = 4E_e^2 \frac{\sin \gamma_h (1 + \cos \theta_e)}{\sin \gamma_h + \sin \theta_e - \sin(\theta_e + \gamma_h)}, \quad (5.8)$$

$$x_{DA} = \frac{E_e \sin \gamma_h + \sin \theta_e + \sin(\theta_e + \gamma_h)}{E_p \sin \gamma_h + \sin \theta_e - \sin(\theta_e + \gamma_h)}, \quad (5.9)$$

$$y_{DA} = \frac{Q_{DA}^2}{sx_{DA}}, \quad (5.10)$$

where the E_p is the proton beam energy. An important advantage of the double angle method is, since it relies on the ratio of the energy measurements, that the uncertainty from the absolute energy scale is much reduced. In this analysis, NC DIS events are simultaneously reconstructed with the above methods to calibrate the energy scale.

5.2 Energy reconstruction

In this analysis, CC DIS events are reconstructed by the Jacquet-Blondel method using energy deposit of the CAL. We make clusters from CAL cells with energy deposit, and then energy corrections due to dead material etc are implemented. In this section, these corrections are introduced.

5.2.1 Noise suppression for the CAL

As the first step, unphysical energy deposits are removed. There are two main sources; signals from the uranium radioactivity and discharge of PMTs.

In order to reject noise cells with the radioactivity of the uranium, EMC (HAC) cells with energy below 60 (110) MeV are not used in this analysis. In addition, the thresholds are raised to 80 (140) MeV for EMC (HAC) cells, if there are no energy deposit in the surrounding cells. These thresholds were determined using events with unpaired positron and proton bunches collected by the random trigger [27].

The discharging of a PMT (called PMT spark) can happen time to time and give a fake large energy. Since a CAL cell is equipped with 2 PMTs, this kind of noise are rejected by requiring the following condition:

$$\begin{aligned} \text{if } (E_{PMT1} + E_{PMT2}) < 1 \text{ GeV,} \\ |E_{PMT1} - E_{PMT2}| > 0.49 (E_{PMT1} + E_{PMT2}) + 0.03, \end{aligned} \quad (5.11)$$

where E_{PMT1} and E_{PMT2} are the energy of the right PMT and the left one, respectively. Hot cells with bad PMTs or electronic read-out problem are monitored during the data taking and not used in the offline analysis.

5.2.2 Clustering of energy deposits

In order to improve the energy resolution of the CAL, clusters are made to obtain the energy deposits nearly equal to that of real particle. When their energy deposits are summed up, the clustering is performed in two steps [26].

In the first step, we make clustering in two dimensional plane, separately for EMC, HAC1 and HAC2. If the energy of a cell is greater than any one of its surrounding cells, the cell is taken as a seed of a cluster. The surrounding cells with less energy are grouped in the cluster.

In the second step, these cluster in the three CAL sections are combined. A probability function of two clusters originating from a single particles, are made as a function of distance in the $(\theta$ and $\phi)$ plane using a pion MC sample.

5.2.3 Energy corrections for the CAL clusters

After the clustering, energy corrections are needed in order to remove several detector effects (Dead material correction, Back-Splash correction) [28].

Dead material correction

The inactive material between the interaction point and CAL causes the energy loss of the particles before entering to the CAL. This effect is corrected separately for electromagnetic cluster and hadronic cluster since the electromagnetic particles (γ, e) develop shower at early stage. The electromagnetic and hadronic clusters are defined as

$$\text{electromagnetic cluster : } f_{EMC} = 1, \quad (5.12)$$

$$\text{hadronic cluster : } f_{EMC} < 1, \quad (5.13)$$

where f_{EMC} is the fraction of cluster energy in the EMC section to the total. The correction factor is functions of the cluster energy, E_{clstr} , and the radiation length, X_0 , of the inactive material in front of CAL. Further, after the above correction, the energy of hadronic cluster (E_{clstr}^{cor}) needs extra correction, since hadronic cluster loses energy by ionisation before initiating a shower. For hadronic cluster with $E_{clstr}^{cor} < 7$ GeV, the correction was estimated using MC. The correction factor was obtained as the ratio between E_{clstr}^{cor} and true cluster energy, E_{clstr}^{tru} , as function of the f_{EMC} .

Back-Splash correction

When a high energy particle hits the FCAL or the forward beam-pipe, many secondary particles are produced and some of them can splash backward to the detector. Although the back-splashed particles have low energy, this effect is non-negligible when the most of primary particles are going forward and γ and y are low[28].

The *Back-Splash correction* is studied with a MC sample of NC DIS with $Q^2 > 400$ GeV. Basically, isolated cells in the rear direction are removed. The clusters are discarded as the back splash if they satisfy

$$E_{clstr} < 3 \text{ GeV}, \quad (5.14)$$

$$\theta_{clstr} > \gamma_{max} \quad \text{or} \quad D > D_{max}, \quad (5.15)$$

where E_{clstr} and θ_{clstr} are the energy and the polar angle of the cluster, respectively. D is the spatial distance at the surface of the CAL to the next cluster with $E > 3 \text{ GeV}$. The thresholds γ_{max} and D_{max} depend on γ_h as follows:

$$\gamma_{max} = \begin{cases} 0.151 + 1.372 \gamma_h, & \gamma_h < 1.95, \\ 2.826 + 0.259 (\gamma_h - 1.95), & \gamma_h > 1.95, \end{cases} \quad (5.16)$$

$$D_{max} = 24.3 + 224.7 \gamma_h - 196.4 \gamma_h^2 + 92.6 \gamma_h^3 - 15.59 \gamma_h^4, \quad (5.17)$$

with γ_{max} , γ_h in radian and D_{max} in cm.

5.2.4 Reconstruction of charged current kinematic variables

Most of kinematic variables are reconstructed with four momentum of the clusters, $(E^{clstr}, p_x^{clstr}, p_y^{clstr}, p_z^{clstr})$, and vertex point. Note that cluster's invariant mass is set to the mass of a pion. The missing transverse momentum $P_{T,miss}$ and $(E - P_z)^{tot}$ is calculated by

$$P_{T,miss} = \sqrt{(\sum_i p_x^{clstri})^2 + (\sum_i p_y^{clstri})^2}, \quad (5.18)$$

$$(E - P_z)^{tot} = \sqrt{\sum_i (E^{clstri} - p_z^{clstri})}. \quad (5.19)$$

And using these variables, y , x and Q^2 are determined one by one from Eq. 5.1-5.3. $P_{T,miss}$ corresponds to $P_{T,h}$ in Eq. 5.4, and $(E - P_z)^{tot}$ corresponds to $(E - P_z)_h$ in Eq. 5.5. In addition, following two variables, γ_0 and $P_{T,miss}(-1ir)$ are used in the charged current event selection. γ_0 is obtained with all cells of CAL and nominal vertex position (0,0,0). $P_{T,miss}(-1ir)$ is calculated with the cells in CAL excluding the first inner ring of FCAL.

Global energy correction

In order to check that the calculated $P_{T,miss}$ and $(E - P_z)^{tot}$ of MC represent those of real data, we check using NC DIS real and MC samples. The energies reconstructed by the Double Angle method and Jacquet-Blondel one are compared.

$$E_q^{DA} = \frac{P_T^{DA}}{\sin \gamma_h} = \frac{\sqrt{Q_{DA}^2(1 - y_{DA})}}{\sin \gamma_h}. \quad (5.20)$$

The difference of E_q^{DA} between MC and data amounts 5 ~ 10 % around $\gamma_h = 0.6$ (2.3) between FCAL(BCAL) and BCAL(RCAL). $P_{T,miss}$ and $(E - Pz)_h$ of MC events are re-weighted to data and we calculate the kinematic variables.

5.3 Vertex reconstruction

It is important to accurately measure the interaction point for the reconstruction of kinematic variables. The z vertex position is primarily measured by using the CTD tracks [29]. However, since the scattered neutrino is not detected in ZEUS detector in CC events, the usable tracks for the vertex measurement are limited for events that have low hadronic angle. Most of the tracks from hadronic system are outside of CTD acceptance and the vertex reconstruction will be poor. A method to measure the vertex using FCAL timing is developed [31] and used for such events.

Vertex reconstruction by FCAL timing

The longitudinal size of the positron bunch is much small comparing to that of the proton bunch. An ep collisions occurs while the electron 'point-like' beam is travelling through the proton bunch. Therefore, vertex position is fully correlated where the interacting proton is located in the bunch. For example, if the proton is located at +30 cm from the centre of the bunch, interaction occurs at $Z = +15$ cm and generated particles arrive at FCAL earlier by 1 ns and if it is -30 cm from the centre, the particles arrive later by 1 ns. (Note that we regard the velocity of beam as the speed of light). In this way, we can know the vertex position from the FCAL timing.

We explain this method here. The timing of each FCAL cell is tuned such that the particles come from the nominal interaction point ($z = 0$) is zero. The expected cell timing of FCAL, T_{cell} , is related with z_{vtx} as follows:

$$T_{cell} = \frac{1}{c} \left((z_{nomi} - z_{vtx}) - \sqrt{x_{cell}^2 + y_{cell}^2 + (z_{cell} - z_{vtx})^2} - \sqrt{x_{cell}^2 + y_{cell}^2 + z_{cell}^2} \right), \quad (5.21)$$

where $(x_{cell}, y_{cell}, z_{cell})$ is the position of cell. c is the velocity of light, and z_{nomi} is the nominal z position and hence $z_{nomi} = 0$. With this relation, z_{vtx} is measured from each FCAL cell i , $z_{vtx}^{cell i}$. The z -vertex Z_{vtx}^{FCAL} is obtained with the weighted sum as follows:

$$Z_{vtx}^{FCAL} = \frac{\sum_i \frac{1}{\sigma_i^2} z_{vtx}^{cell i}}{\sum_i \frac{1}{\sigma_i^2}}. \quad (5.22)$$

Comparison of the z -vertex from the CTD and the FCAL-timing

The calibration for Z_{vtx}^{FCAL} was done with real NC DIS events. The resolution is found to be 9.7 cm. The efficiency and resolution of vertex measured by CTD and FCAL timing in CC DIS sample are shown in Figure.5.1 as function of hadronic angle reconstructed by the nominal vertex, γ_0 . In both of efficiency and resolution, FCAL timing vertex get better than CTD vertex in low γ_0 . In this analysis, CTD vertex is required to events with the region $\gamma_0 > 0.4$ (called high- γ_0 event), and FCAL timing vertex in the region $\gamma_0 < 0.4$ (called low- γ_0). CC DIS event selection is implemented separately for high- γ_0 and low- γ_0 .

Vertex distribution of MC

The vertex distribution of the real data fluctuates run by run reflecting the beam drift of the HERA operation. It is important to use the same distribution for MC in order to use MC samples for acceptance correction. The vertex distribution is measured with NC DIS events. The two polarisation data have different Z distribution as shown in Figure 5.2. The MC events is re-weighted differently for the two polarisation data sample to match to the measured distribution.

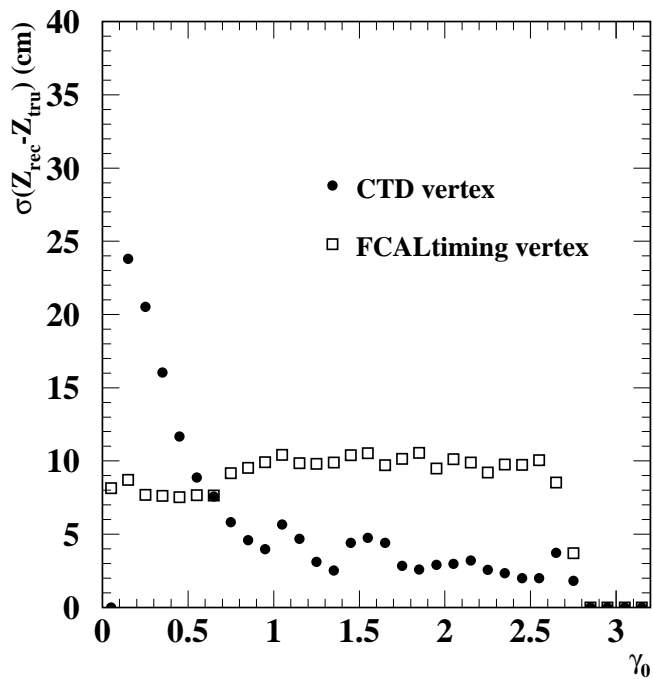
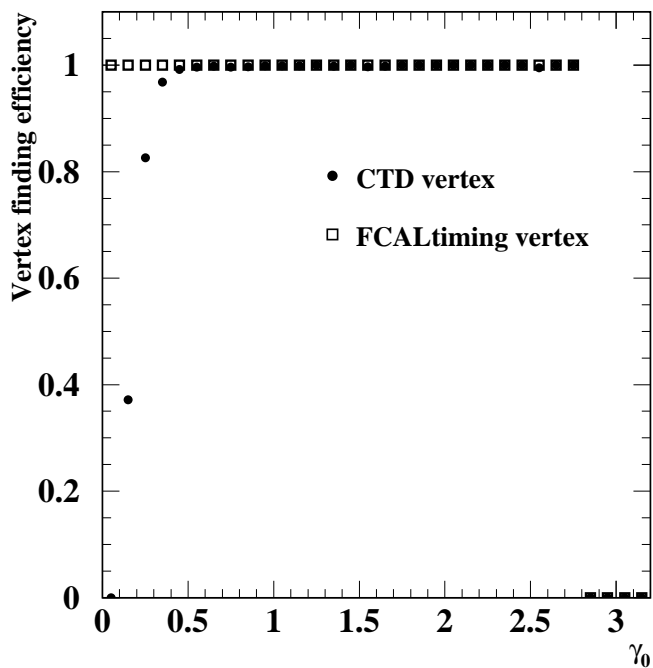


Figure 5.1: Efficiency (top) and resolution (bottom) of CTD and FCAL timing vertices determined with MC sample are shown. Dots and squares denotes for CTD and FCAL timing vertex, respectively.

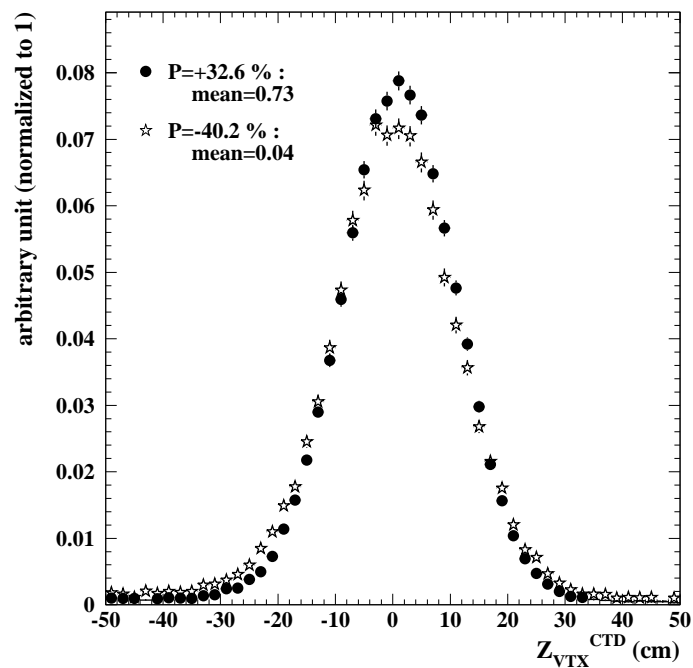


Figure 5.2: Z vertex distribution of NC real data at $P = +32.6\%$ and $P = -40.2\%$: closed circles are for data $P = +32.6\%$ and stars are for $P = -40.2\%$

Chapter 6

EVENT SELECTION

In this chapter, the selection procedures are explained. The most distinguishable signature of the CC event is a large missing transverse momentum ($P_{T,miss}$) from the escaping neutrino. Since $Q^2 \sim P_{T,miss}^2$, lower $P_{T,miss}$ threshold is desirable to measure wider Q^2 and y region. However, by lowering the $P_{T,miss}$ threshold, many non- e^+p process and non- e^+p backgrounds are contained. Complicated rejection algorithms are then needed to further suppress these backgrounds.

6.1 Trigger requirement

6.1.1 FLT selection

FLT is fired with $P_{T,miss}^{FLT}$ measured by CAL FLT and with additional requirement of CTD tracks. $P_{T,miss}^{FLT}$ is missing transverse momentum calculated with all CAL cells with a hardware processor in CAL FLT. CC candidates are required to satisfy at least one of the follows (slot60):

slot60 :

$$1. \quad P_{T,miss}^{FLT} \geq 5 \text{ GeV and } E_T^{FLT} \geq 5 \text{ GeV and } N_{good-trk}^{FLT} \geq 1 \\ \text{and TightTrackVeto,} \quad (6.1)$$

$$2. \quad P_{T,miss}^{FLT} \geq 8 \text{ GeV and } N_{trk}^{FLT} \geq 1 \text{ and TightTrackVeto,} \quad (6.2)$$

$$3. \quad P_{T,miss}^{FLT} \geq 11 \text{ GeV and } E_{FCALth}^{FLT} \geq 10 \text{ GeV} \\ \text{and TightTrackVeto,} \quad (6.3)$$

where the E_T^{FLT} is total transverse energy excluding two rings of the calorimeter

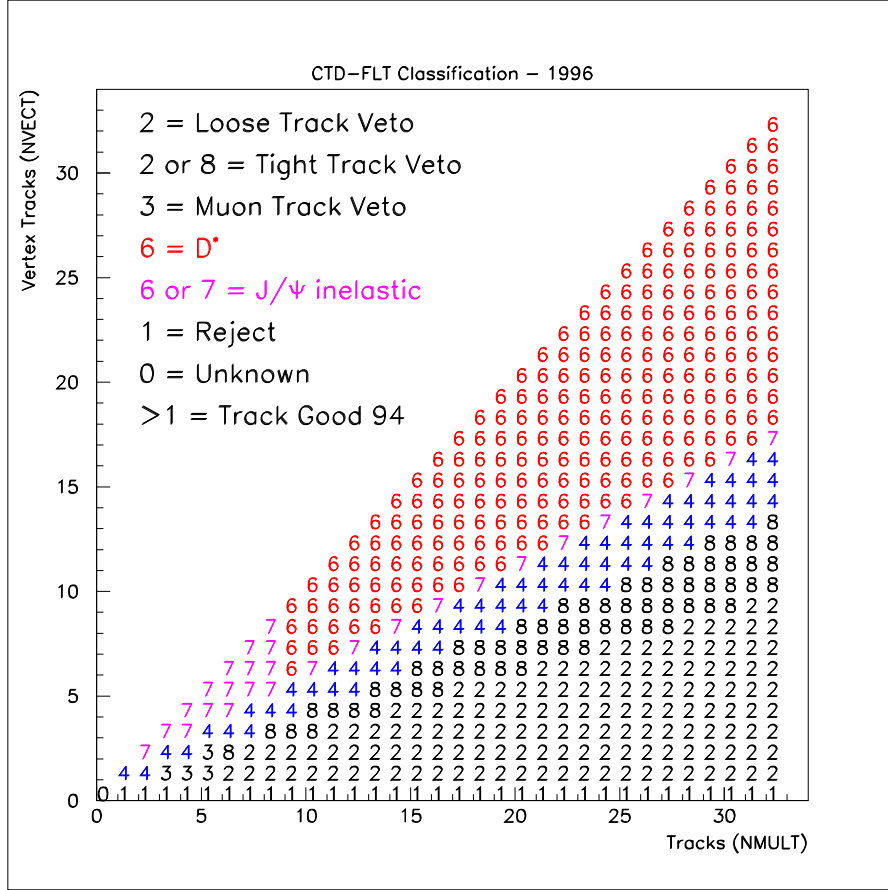


Figure 6.1: CTD track classification at FLT level

cells closest to the FCAL beam pipe. $N_{good-trk}^{FLT}$ and N_{trk}^{FLT} denote the numbers of CTD tracks which come from the nominal interaction point and all CTD tracks at FLT level, respectively. The first two logics require at least one CTD track keeping low $P_{T,miss}^{FLT}$ threshold, while the third logic use CAL information only to keep an acceptance for no CTD track event. *Tight Track Veto* is to reject events with many CTD tracks not originating from the interaction region. Figure 6.1 shows CTD FLT class (TrkClass) using $N_{good-trk}^{FLT}$ and N_{trk}^{FLT} . In *Tight Track Veto*, events are rejected if TrkClass is 2 or 8. This *Tight Track Veto* is newly implemented since 2004 in order to cope with the high trigger rate from the beam-gas. Inefficiency due to 'Tight Track Veto' is about 9 % which is estimated with NC events[32].

In addition to those trigger logics with $P_{T,miss}$, five trigger logics are also used to increase the trigger efficiency of CC events. They are defined as:

- slot39* : $E_{BEMC}^{FLT} \geq 3$ GeV and *Bisoe* and $N_{good-trk}^{FLT} \geq 1$ and *LooseTrackVeto*
slot40 : $E_{EMC}^{FLT} \geq 25$ GeV and *TightTrackVeto*
slot41 : $E_T^{FLT} \geq 30$ GeV and *TightTrackVeto*
slot43 : $E_T^{FLT} \geq 12$ GeV and $N_{good-trk}^{FLT} \geq 1$ and *TightTrackVeto*
slot44 : ($E_{BEMC}^{FLT} \geq 10$ GeV or $E_{RCAL}^{FLT} \geq 3$ GeV) and *Bisoe* and $N_{good-trk}^{FLT} \geq 1$
 and *TightTrackVeto*

where the E_{EMC}^{FLT} is the energy sum of EMC section excluding the three inner rings of the FCAL and the innermost ring of the RCAL in all calorimeter components. E_{BEMC}^{FLT} and E_{RCAL}^{FLT} are the sum of EMC section of BCAL and RCAL excluding the innermost ring, respectively. *Bisoe* denotes there is a isolated positron in BCAL. 'Loose Track Veto' rejects events with *TrkClass* = 2. In order to decrease the trigger rate, no hit with beam-gas timing is required in C5, *Vetowall* and *SRTD*.

6.1.2 SLT selection

At the SLT, at first, in order to veto the background, we require CAL timing cuts for all generated events as follows:

$$\begin{aligned}
 |T_F^{SLT}| &< 8 \text{ ns}, \\
 |T_R^{SLT}| &< 8 \text{ ns}, \\
 |T_G^{SLT}| &< 10 \text{ ns}, \\
 T_{UP}^{SLT} - T_{DO}^{SLT} &> -10 \text{ ns}, \\
 T_F^{SLT} - T_R^{SLT} &< 8 \text{ ns},
 \end{aligned}$$

where $T_{F(R,G)}^{SLT}$ is the averaged timing of FCAL (RCAL,GCAL which is the global calorimeter). T_{UP}^{SLT} and T_{DO}^{SLT} are the averaged timing of the upper and lower halves of CAL.

And CC events are triggered when they satisfy the following two logics (S1 and S2):

- S1. (*CCtimeOK* or *CCCTDOK*) and *NoOffBeamProton*

$$\begin{aligned}
 CCtimeOK &: |T_G^{SLT}| < 7 \text{ ns and } N_{PMT}^G > 1 \\
 NoOffBeamProton &: |P_y^{SLT}| > 3 \text{ GeV or } P_{T,miss}^{SLT} > 15 \text{ GeV or} \\
 &P_{T,miss}^{SLT}(-ir) > 6 \text{ GeV or } P_{T,miss}^{SLT} > 0.06 \cdot P_Z^{SLT} \\
 CCCTDOK &: N_{trk}^{SLT} \geq 1 \text{ and } Z_{utx}^{SLT} < 100 \text{ cm}
 \end{aligned}$$

- S2. CC1 or CC2 or CC3 or CC4.

$$\begin{aligned}
\text{CC1 : } & P_{T,miss}^{SLT} > 6 \text{ GeV and } E_T(-2ir) > 6 \text{ GeV and } N_{good-trk}^{SLT} > 1 \\
\text{CC2 : } & P_{T,miss}^{SLT} > 9 \text{ GeV and } P_{T,miss}^{SLT}(-1ir) > 8 \text{ GeV and } E_{FCAL}^{SLT} > 20 \text{ GeV} \\
\text{CC3 : } & P_{T,miss}^{SLT} > 9 \text{ GeV and } (P_{T,miss}^{SLT})^2 > 2.31 * E_T^{SLT} \text{ and } E_{FCAL}^{SLT} > 80 \text{ GeV} \\
\text{CC4 : } & E^{SLT} - P_Z^{SLT} > 6 \text{ GeV and } (P_{T,miss}^{SLT})^2 > 2.25 * E_T^{SLT} \text{ and } N_{good-trk}^{SLT} > 1,
\end{aligned}$$

where N_{PMT}^G is number of PMTs of the global calorimeter. P_y^{SLT} is y component of the vector momenta calculated from all cells with energy deposited in the calorimeter. CC1 and CC4 are logics for high- γ_0 and for low- γ_0 CC2 and CC3 are available logics.

6.1.3 TLT selection

We require some CAL timing cuts to reject non- ep background events as follows,

$$\begin{aligned}
|T_F^{TLT}| &< 8 \text{ ns,} \\
|T_R^{TLT}| &< 6 \text{ ns,} \\
|T_G^{TLT}| &< 8 \text{ ns,} \\
|T_F^{TLT} - T_R^{TLT}| &< 8 \text{ ns,}
\end{aligned}$$

where the superscript ' TLT ' denotes TLT level variables. E_{tot}^{TLT} is the total energy of CAL. Further, at the TLT, CC candidates are required to pass at least one of the following logics:

$$\begin{aligned}
\text{EXO_TLT_2} & : P_{T,miss}^{TLT} > 6 \text{ GeV and } |Z_{vtx}^{TLT}| < 60 \text{ cm and } UDTIMEOK, \\
\text{EXO_TLT_6} & : P_{T,miss}^{TLT} > 8 \text{ GeV and } (E_{FCAL}^{TLT} > 10 \text{ GeV or } N_{good-trk}^{TLT} > 0) \text{ and} \\
& \text{not(OffBeamProton) and not(BeamGasVertex) and} \\
& \text{(not(TooManyBeamGasTracks) or (TwoTrackGoodVertex)) and} \\
& \text{(CTDHits < 2500 or } P_{T,miss}^{TLT} > 10 \text{ GeV) and } UDTIMEOK,
\end{aligned}$$

where the Z_{vtx}^{TLT} is the z coordinate of the measured interaction vertex. The sub-logics are defined as

$$\begin{aligned}
UDTimeOK &= \text{not}(N_{PMT}^{U,TLT} \geq 2 \text{ and } E^{U,TLT} > 1.0 \text{ GeV and} \\
&N_{PMT}^{D,TLT} \geq 2 \text{ and } E^{D,TLT} > 1.0 \text{ GeV and} \\
&|T^{U,TLT} - T^{D,TLT}| > \max(8 \text{ ns}, 3 \sqrt{T_{ERR}^{U,TLT^2} + T_{ERR}^{D,TLT^2}}),
\end{aligned}$$

$$\begin{aligned}
OffBeamProton &= P_{T,miss}^{TLT}(-ir) < 10 \text{ and } P_{T,miss}^{TLT} < 25 \text{ and } P_{T,miss}^{TLT} < 0.7 E_T^{TLT} \text{ and} \\
&(E - P_Z)^{TLT} < 10 \text{ and } P_{T,miss}^{TLT} < 0.08 \cdot P_Z^{TLT} \text{ and } |P_y| < 4.
\end{aligned}$$

$$\begin{aligned}
TooManyBeamGasTracks &= N_{BGtrk}^{TLT} \geq 5 \text{ and } N_{trk}^{TLT} \geq 25 \\
TwoTrackGoodVertex &= GoodVertex \text{ and } N_{vtx-trk}^{TLT} \geq 2
\end{aligned}$$

where the N_{PMT}^U and N_{PMT}^D are number of PMTs with a signal in upper half and lower one, respectively. And the $E^{U(D),TLT}$, $T_{ERR}^{U(D),TLT}$ and $T^{U(D),TLT}$ are energy, resolution of the average timing and timing of in upper(lower) half of CAL, respectively. The requirement of the difference between up and lower of CAL is against cosmic-ray events. And the *BeamGasTracks* and *GoodVertex* are defined as follows,

$$\begin{aligned}
BeamGasTracks &= D_Z^{CA} < -80 \text{ cm} \\
GoodVertex &= |Z_{vtx}^{TLT}| < 60 \text{ cm and } R_{vtx} < 10 \text{ cm},
\end{aligned}$$

where D_Z^{CA} denotes the Z -distance from the closest approach to the primary vertex. R_{vtx} is a radius from the primary vertex to the nominal vertex (0,0,0).

6.1.4 pre-selection

We require pre-selection cut as follows:

$$P_{T,miss} > 7 \text{ GeV}, \quad (6.4)$$

$$P_{T,miss}(-1ir) > 7 \text{ GeV}. \quad (6.5)$$

6.2 Kinematic region

Q^2 cut and y cut are required to restrict the kinematic region such that the background contamination is low and the resolution for the kinematic quantities is good.

In this analysis, the thresholds are set to

$$Q_{JB}^2 > 200 \text{ GeV}^2, \quad (6.6)$$

$$y_{JB} < 0.9. \quad (6.7)$$

6.3 Selection for high- γ_0 and low- γ_0 events

Events are first classified into two categories using γ_0 . High- γ_0 sample is event with $\gamma_0 > 0.4$ and low- γ_0 sample is event with $\gamma_0 < 0.4$. Different event selection is implemented for each sample. For the high- γ_0 events, the hadronic system is detected inside the CTD; hence the CTD tracking information is used for vertex reconstruction and event selection. On the other hand, for the low- γ_0 , the hadronic system is detected in the forward region of the ZEUS detector and not out of the CTD; hence the CTD tracking information is not used for the low- γ_0 events. As mentioned in Section 5.3, for low- γ_0 sample, the z vertex reconstructed by FCAL-timing is used.

6.3.1 Selection for high- γ_0 events

Missing transverse momentum requirement

The CC candidates are selected by requiring a large missing transverse momentum. The high- γ_0 events must satisfy the following condition:

$$P_{T,miss} > 12 \text{ GeV}, \quad (6.8)$$

$$P_{T,miss}(-1ir) > 10 \text{ GeV}. \quad (6.9)$$

Figure 6.2 shows the distributions of $P_{T,miss}$ and $P_{T,miss}(-1ir)$. After these requirements, MC describes MC well.

In the following figures (6.2-6.4), the distribution are shown for the event samples after imposing all selection cuts except for those with the variables and data in figures represent all e^+p data.

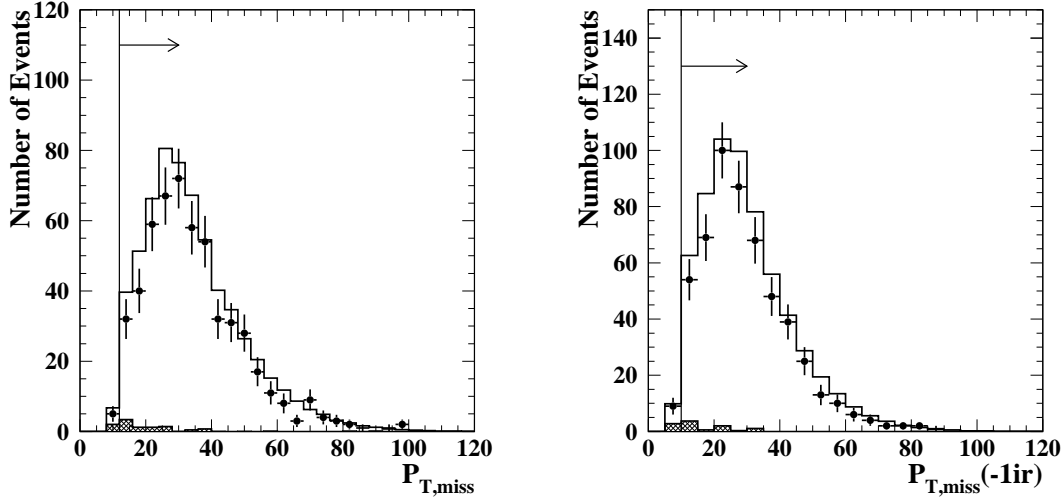


Figure 6.2: Missing transverse momentum $P_{T,miss}$ (left) and $P_{T,miss}(-1ir)$ (right) distributions for high- γ_0 sample; closed circles are the all e^+p data and the solid histograms are the total of the CC MC and the PhP MC. The PhP MC expectation is shown as the hatched histogram. They are after applying all the selection excepting both of $P_{T,miss}$ and $P_{T,miss}(-1ir)$ requirements.

Vertex requirement

The Z vertex position is measured using the CTD for high- γ_0 events. We required the Z vertex as

$$-50 \text{ cm} < Z_{vtx}^{CTD} < 50 \text{ cm}. \quad (6.10)$$

Figure 6.3 shows the distribution of Z vertex. Data and MC at the Z vertex region between -50 cm to $+50$ cm are in good agreement.

Photoproduction (PhP) background rejection

The photoproduction (PhP) events normally have di-jets and no missing transverse momentum. However if the heavy quark is in the final state and if it decays into the neutrino and lepton, the $P_{T,miss}$ becomes large. Besides, since PhP cross section is large, this is the most important background.

In CC DIS event, transverse energy flow is collimated in the direction of $P_{T,miss}$ more than in PhP background. In order to reject the photoproduction background, $P_{T,miss}/E_T$ is required as

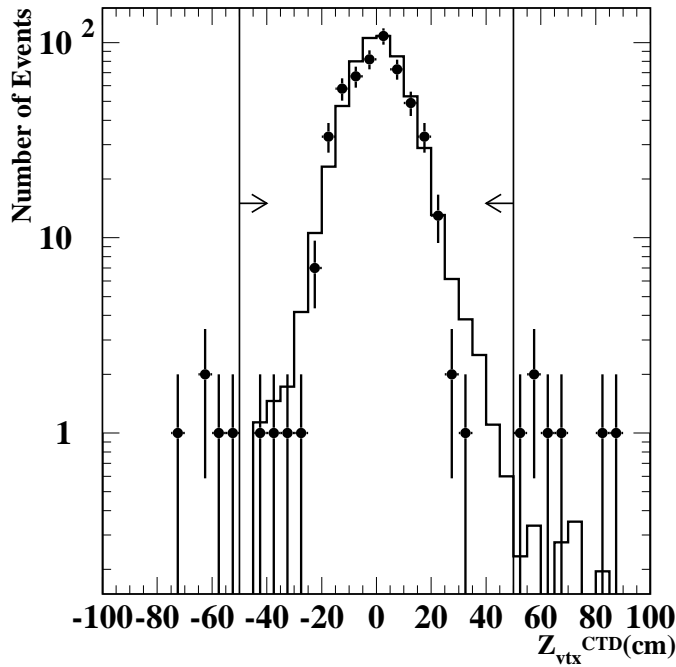


Figure 6.3: The Z vertex distribution measured by CTD for high γ_0 events; the closed circles denote all e^+p data and the solid histogram denotes the CC MC. This is after applying all the selection except for this Z vertex requirement.

$$P_{T,miss}/E_T > 0.55, \text{ if } P_{T,miss} < 20 \text{ GeV}, \quad (6.11)$$

$$P_{T,miss}/E_T > 0.4, \text{ if } 20 \text{ GeV} < P_{T,miss} < 30 \text{ GeV}. \quad (6.12)$$

$P_{T,miss}/E_T$ distributions are shown in Figure 6.4.

Tracking cuts against beam-gas events

The tracking information from CTD is useful to reject beam-gas events. The beam-gas events have a small fraction of clean tracks called '*good track*' comparing to CC DIS events. To study the character of the beam-gas events, beam-gas enriched sample is selected by looser selection as follows:

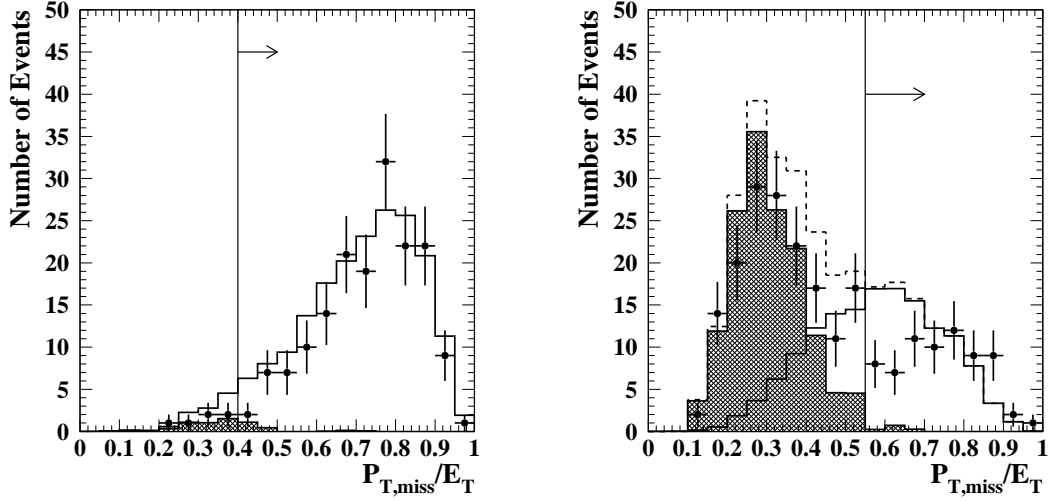


Figure 6.4: $P_{T,miss}/E_T$ distributions; Left and right distributions are for events with $20 < P_{T,miss} < 30\text{GeV}$ and $P_{T,miss} < 20\text{GeV}$, respectively. Closed circles are all e^+p data and the solid histograms are the total of the CC MC and the PhP MC. The PhP MC expectation is shown as the hatched histogram. They are after all selection except for both of PHP rejections (Eq.6.11-6.12)

$$P_{T,miss} > 7 \text{ GeV instead of } P_{T,miss} > 12 \text{ GeV}, \quad (6.13)$$

$$P_{T,miss}(-1ir) > 7 \text{ GeV instead of } P_{T,miss} > 10 \text{ GeV}, \quad (6.14)$$

$$Q^2 > 50 \text{ GeV}^2 \text{ instead of } Q^2 > 200 \text{ GeV}. \quad (6.15)$$

$$\text{no tracking cut} \quad (6.16)$$

$P_{T,miss}$ distribution of the sample is shown in Figure 6.5. Comparing CC MC, data has a large excess at low $P_{T,miss}$. These events have many tracks not originated from the event vertex. We therefore apply the tracking cut with number of tracks (N_{TRK}) and number of good tracks (N_{TRK}^{good}) as

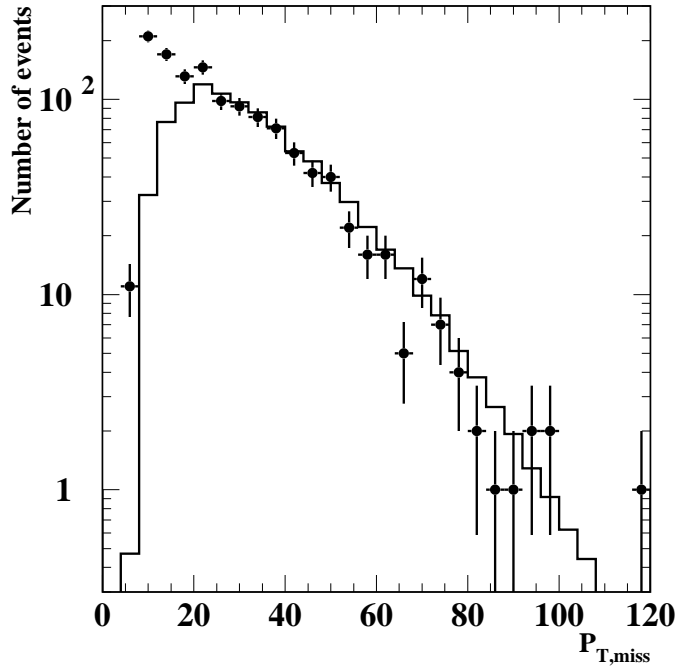


Figure 6.5: The $P_{T,miss}$ distribution of beam-gas enriched sample; the dots represent the beam-gas enriched sample selected from all e^+p data and the solid histogram denotes CC MC. This is after applying the enriched sample selection except for tracking cut defined in Eq. 6.17-6.20.

For events with $P_{T,miss} > 25$ GeV,

$$N_{trk}^{good} \geq 1, \quad (6.17)$$

$$N_{trk}^{good} > 0.25 (N_{trk}^{all} - 20), \quad (6.18)$$

For events with $P_{T,miss} < 25$ GeV,

$$N_{trk}^{good} \geq 7, \quad (6.19)$$

$$N_{trk}^{good} > 0.1 (N_{trk}^{all} + 30), \quad (6.20)$$

The *good track* is defined as a vertex fitted track which has the transverse momentum of $P_T^{trk} > 0.2$ GeV and is detected in the polar angle θ^{trk} from 15° to 164° . Figure 6.6 and Figure 6.7 show the tracking cuts for $P_{T,miss} < 25$ GeV and for $P_{T,miss} > 25$ GeV, respectively. After the tracking cuts, it is found that MC and DATA are in good agreement. In low $P_{T,miss}$ region, beam-gas background events

has tracking quality similar to CC DIS events. Many CC DIS events is rejected in order to remove the backgrounds.

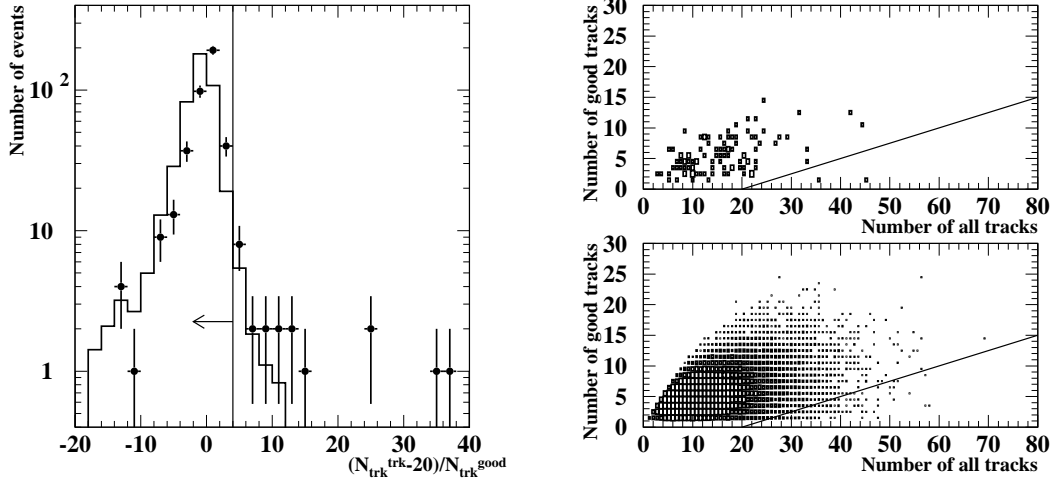


Figure 6.6: Tracking cut for events with $P_{T,miss} > 25$ GeV: one(left) and two(right) dimensional distributions of the tracking cut for events with $P_{T,miss} > 25$ GeV. Left: closed circles are the all e^+p data and the solid histogram is the CC MC. Right upper denotes the beam-gas enriched data and the right lower denotes the CC MC. The solid line represents threshold of this cut. They are after applying all the selection except for the tracking cut (Eq.6.17-6.18)

$\Delta\phi$ cut

In this analysis, $P_{T,miss}$ is measured with the CAL but it is also possible to calculate $P_{T,miss}$ with the *good tracks*. The ϕ difference of the two measurement is useful to reject not only the beam-gas overlapping the e^+p physics events but also the PhP and NC events.

We require as

$$|\Delta\phi| < 1.0 \text{ radian for events with } P_{T,miss} < 30 \text{ GeV}, \quad (6.21)$$

$$|\Delta\phi| < 2.0 \text{ radian for events with } P_{T,miss} > 30 \text{ GeV}. \quad (6.22)$$

Two distributions as shown in Figure 6.8 are $d\phi$ distributions for $P_{T,miss} < 30$ GeV and $P_{T,miss} > 30$ GeV, respectively.

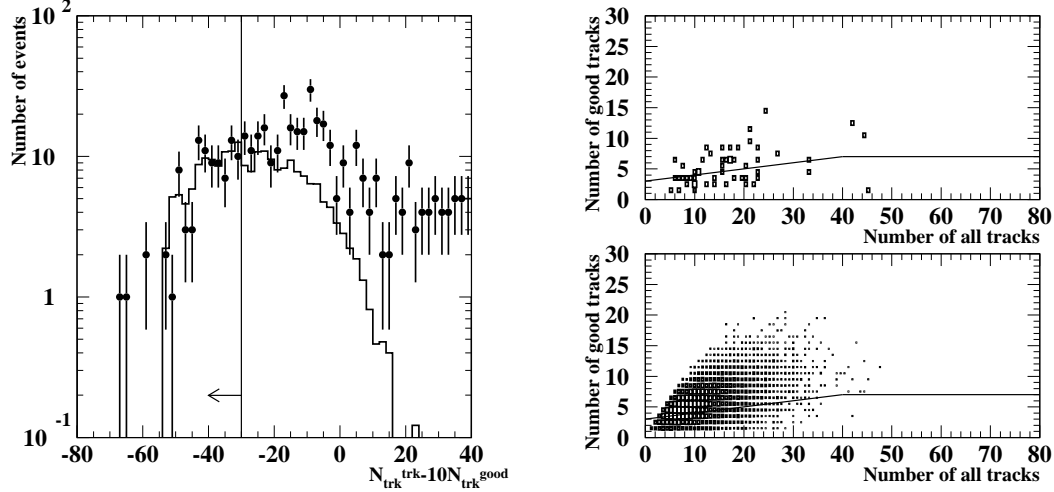


Figure 6.7: Tracking cut for events with $P_{T,miss} < 25$ GeV: One(left) and two(right) dimension distributions of the tracking cut for events with $P_{T,miss} < 25$ GeV. Left: Closed circles are the all e^+p data and the solid histogram is the CC MC. Right upper denotes the beam-gas enriched data and the right lower denotes the CC MC. The solid line represents threshold of this cut. They are after applying all the selection except for the tracking cut (Eq. 6.19-6.20)

NC DIS event rejection

NC DIS events have possibility to have $P_{T,miss}$ due to missing a part of the energy of electron or hadronic system. The character of NC DIS events is to have the scattered positron. A neural network program (SINISTRA95[33]) is used to identify the scattered positron in the calorimeter. Some variables concerning NC DIS events rejection are shown in Figure 6.9. We reject events which satisfy all of the following conditions:

1. $P_{T,miss} < 30$ GeV, (6.23)

2. $(E - P_Z)^{tot} > 30$ GeV, (6.24)

3. $E_e > 4$ GeV, (6.25)

4. $E_{cone} - E_e < 5$ GeV, (6.26)

5. $P_e^{trk}/E_e > 0.25$, (if $15^\circ < \theta_e < 164^\circ$) (6.27)

6. $E_T^e > 2$ GeV, (if $\theta_e > 164^\circ$) (6.28)

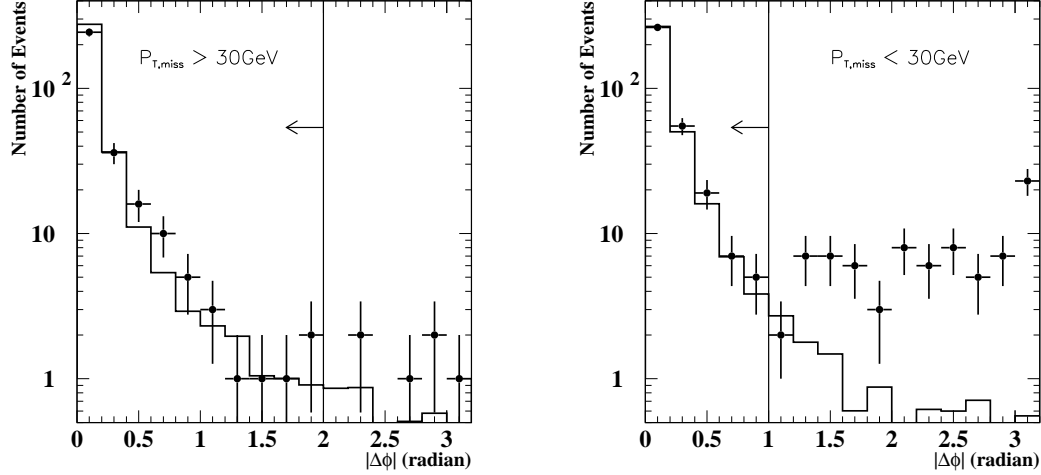


Figure 6.8: $d\phi$ distributions; The left plot is for $P_{T,miss} < 30$ GeV and the right one is for $P_{T,miss} > 30$ GeV after applying all CC selection except for tracking cut and $\delta\phi$. The dots denotes the all e^+p data and the solid histogram denotes CC MC. They are after applying all the selection except for the $\Delta\phi$ cut.

where E_e is the energy of the scattered positron candidate. E_{cone} denotes the energy within $R = \sqrt{\delta\phi^2 + \delta\eta^2} < 0.8$ around the scattered positron. P_e^{trk} , θ_e^{trk} and E_T^e are the momentum, polar angle and transverse energy of the positron track in CTD, respectively.

6.3.2 Selection for low- γ_0 events

Missing transverse momentum requirement

For the low- γ_0 sample, the higher thresholds of $P_{T,miss}$ and $P_{T,miss}(-1ir)$ than for high- γ_0 sample are required, since selection variables with CTD tracking can not be used. The low- γ_0 events must satisfy the following condition:

$$P_{T,miss} > 14 \text{ GeV}, \quad (6.29)$$

$$P_{T,miss}(-1ir) > 12 \text{ GeV}. \quad (6.30)$$

The distributions are shown in Figure 6.10. We observed MC represent data well.

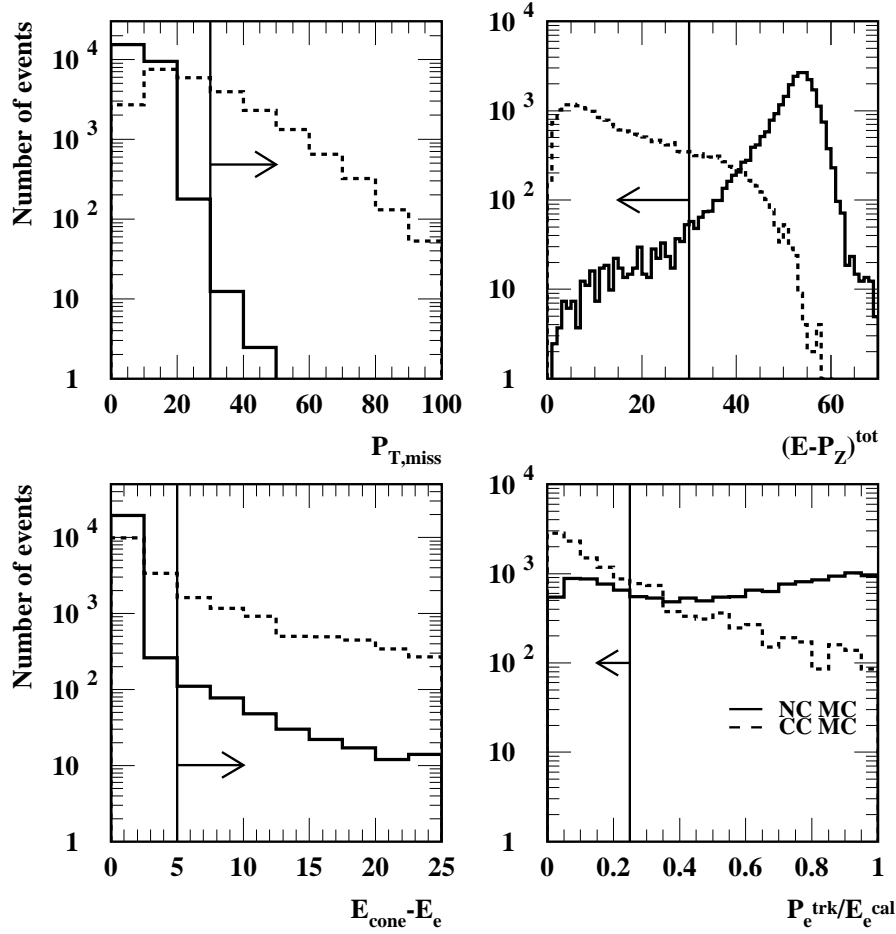


Figure 6.9: NC-DIS rejection distributions; The distributions of $P_{T,miss}$ (left upper), $(E - P_Z)^{tot}$ (right upper), E_e (left middle), $E_{cone} - E_e$ and P_e^{trk}/E_e^{CAL} are shown. The solid and dashed histograms denote NC DIS MC and CC DIS MC, respectively. They are after applying all the selection except for the NC DIS rejection.

Vertex requirement

The Z vertex position is measured using the FCAL-timing for low- γ_0 sample. The Z vertex is required as

$$-50 \text{ cm} < Z_{vtx}^{FCALt} < 50 \text{ cm}, \quad (6.31)$$

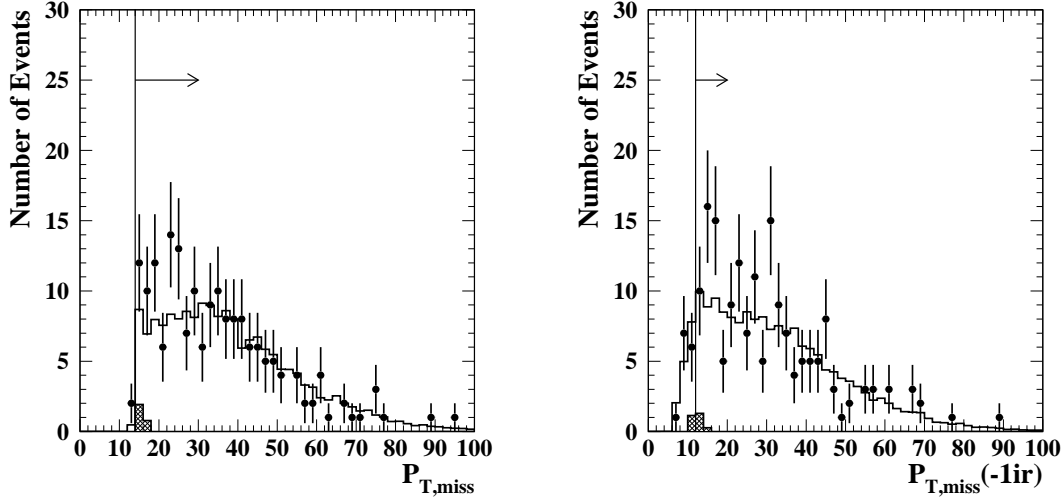


Figure 6.10: Missing transverse momentum $P_{T,miss}$ (left) and $P_{T,miss}(-1ir)$ (right) distribution for low- γ_0 sample; Closed circles are the all e^+p data and the solid histograms are the total of the CC MC and the PhP MC . The PhP MC expectation is shown as the hatched histogram. They are after applying all the selection excepting both of $P_{T,miss}$ and $P_{T,miss}(-1ir)$ requirements.

where Z_{vtx}^{FCALt} denotes Z vertex measured with FCAL-timing. Figure 6.11 shows Z vertex distribution.

Halo-muon rejection

The backgrounds from halo-muon and cosmic-muon events can be larger in low- γ_0 region than in high- γ_0 because of the lack of tracking cuts. Therefore, using the fact that the CAL cluster size of muons is generally small, additional rejection was implemented.

Muon tends to have larger energy deposit in HAC2 than EMC and HAC1. For cosmic muon , especially, it crosses many outer CAL cells to deposit large energy. Therefore, the following cuts are imposed on FCAL energy sharing. We require that event satisfies with all following conditions,

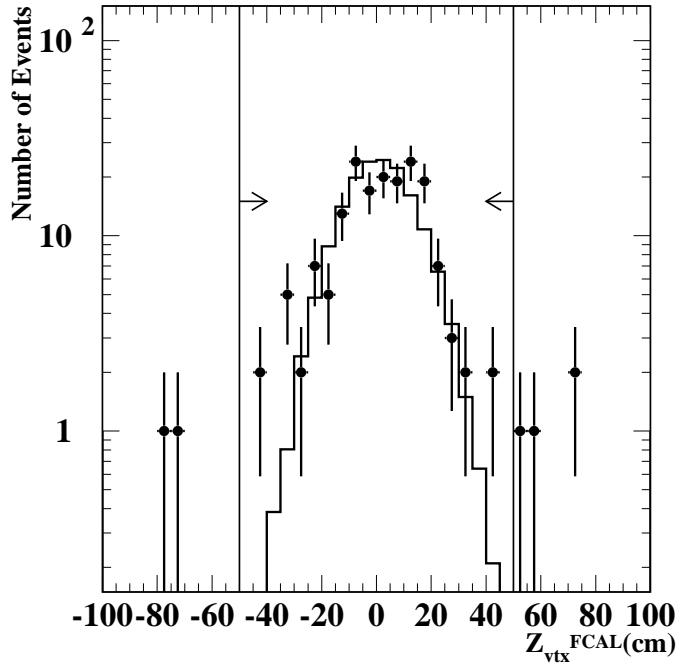


Figure 6.11: The Z-vertex distribution measured using FCAL-timing for low- γ_0 events; Closed circles are the all e^+p data and the solid histograms is the CC MC. They are after applying all selection excepting Z vertex requirement.

$$E_{FCAL}^{EMC}/E_{FCAL} > 0.1, \quad (6.32)$$

$$E_{FCAL}^{HAC1}/E_{FCAL} > 0.1, \quad (6.33)$$

$$E_{FCAL}^{HAC2}/E_{FCAL} < 0.5, \quad (6.34)$$

where E_{FCAL}^{EMC} , E_{FCAL}^{HAC1} and E_{FCAL}^{HAC2} are energy of EMC, HAC1 and HAC2 in FCAL, respectively. E_{FCAL} is the total energy of FCAL. These energy fractions are shown in Figure 6.12.

Another rejection algorithm is implemented based on the size of energy deposit in FCAL. The cell which has the largest transverse energy in FCAL is selected as the seed cell of the cluster. Then if the neighbouring cells has energy more than 100 MeV, the cell is merged to the cluster. This procedure is repeated until the cluster

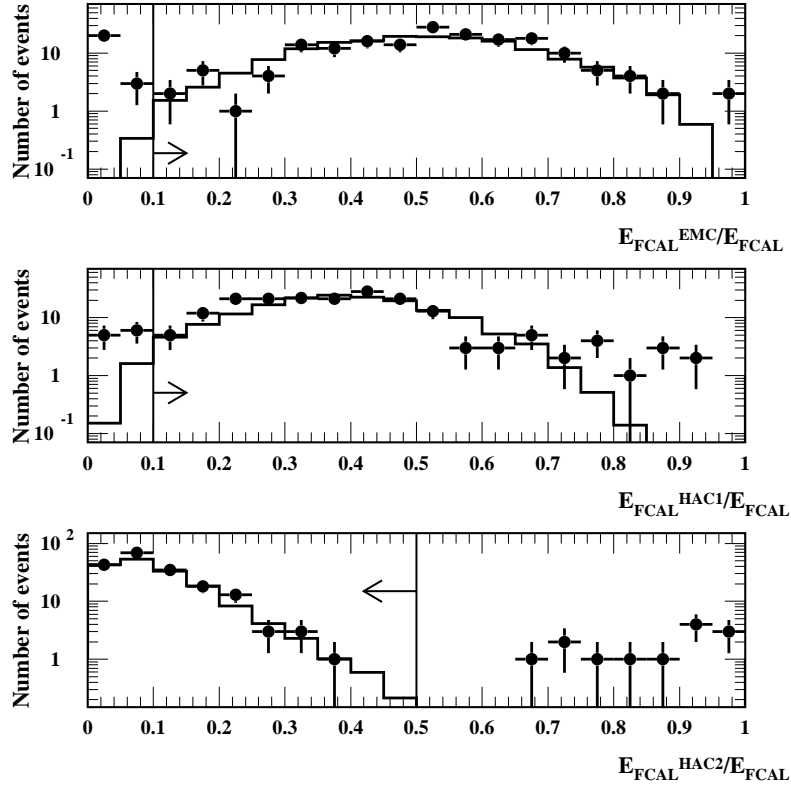


Figure 6.12: Energy fractions in FCAL; Closed circles are the all e^+p data and the solid histograms are the CC MC. They are after applying all the selection except for these requirements (Eq.6.32-6.34).

stops growing. Then, if no CTD track is associated to this cluster, we reject events that satisfy all the following cuts:

$$N_{wid}^{md} > 2, \quad (6.35)$$

$$N_{wid}^{tw} > 2, \quad (6.36)$$

$$E_T^{wid} > 10 \text{ GeV}, \quad (6.37)$$

$$R_{aso} < 0.1 \text{ GeV} \quad (6.38)$$

where N_{wid}^{md} and N_{wid}^{tw} are the cell widths of cluster in module and tower. E_T^{wid} denotes the cluster size calculated using the cluster's cells averaged by the transverse energy against the cluster centre. Halo-muon background generally can be deposit energy

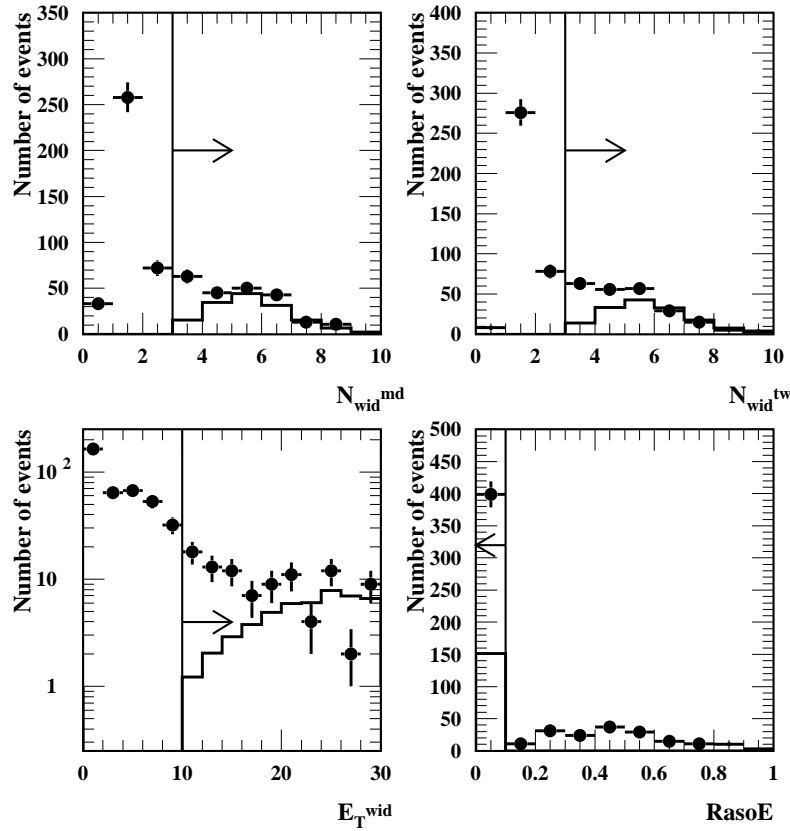


Figure 6.13: Cluster size distributions in FCAL for low- γ_0 sample; Closed circles are the all e^+p data and the solid histograms are the CC MC. The PhP MC expectation is shown as the hatched histogram. They are after applying all the selection excepting the halo muon rejections described in Eq.6.35-6.38.

at RCAL. $Raso$ is the RCAL energy deposit associated to this cluster, and is defined as

$$Raso \equiv \sum_i^{\sqrt{(x_i-x_0)^2+(y_i-y_0)^2} < 30 \text{ cm}} E_i, \quad (6.39)$$

where the x_0 and y_0 means the x and y position of FCAL seed cluster. i runs over all RCAL cells that satisfy $\sqrt{(x_i-x_0)^2+(y_i-y_0)^2} < 30$ cm. The distributions of their variables are shown in Figure 6.13.

6.4 Non- ep background rejection

6.4.1 Halo-muon and Cosmic-muon rejection with HAC fraction

As mentioned in halo-muon rejection for low- γ_0 events in Subsection 6.3.2, the showers due to hadronic system and due to lepton as halo-muon and cosmic-muon differently spread in CAL. The energy deposit due to halo-muon and cosmic-muon are narrower than hadronic shower as CC DIS events. So the energy deposit in HAC section is also smaller than hadronic shower. We require for both high- and low- γ_0 sample as follows:

$$1. \text{ if } E_{BCAL} > 5 \text{ GeV, then } E_{BCAL}^{HAC}/E_{BCAL} > 0.9, \quad (6.40)$$

$$2. \text{ if } E_{RCAL} > 5 \text{ GeV, then } E_{RCAL}^{HAC}/E_{RCAL} > 0.9, \quad (6.41)$$

where the $E_{BCAL(RCAL)}^{HAC}$ is the total energy deposit of HAC in BCAL.

6.4.2 Spark rejection

When one of the two PMTs in a cell has a discharge, a large energy deposit is fakely observed. Such event tends to have large $P_{T,miss}$. In order to reject the spark events overlapping with other backgrounds, we reject the spark events with one of the following cuts:

$$1. \quad \frac{E_{T,cell}^{max}}{E_T} > 0.8(0.7), \quad (6.42)$$

$$2. \quad \frac{P_{T,miss}(-_{cell}^{max})}{P_{T,miss}} < 0.2(0.3), \quad (6.43)$$

$$3. \quad 0.5 < \frac{P_{T,miss}(-_{cells}^{imbal})}{P_{T,miss}} < 2.0, \quad (6.44)$$

where $E_{T,cell}^{max}$ is the transverse energy of the cell with the maximum transverse energy. $P_{T,miss}(-_{cell}^{max})$ is $P_{T,miss}$ calculated using all cells except for the cell with the maximum transverse energy. $P_{T,miss}(-_{cells}^{imbal})$ denotes $P_{T,miss}$ calculated using all cells except for the cells with a large imbalance which is defined as

$$Imbl = \left| \frac{E_{PMT1} - E_{PMT2}}{E_{PMT1} + E_{PMT2}} \right| > 0.8. \quad (6.45)$$

If one of the two PMTs in the cell has a discharge, the imbalance of two PMTs is very large.

6.4.3 CAL timing cut

CAL timing is useful to reject non-*ep* backgrounds and is already required in TLT level. Further, the tighter thresholds of CAL timing cut were applied after tuning the threshold with NC real data excluding a electron candidate. So that these NC real data reproduce CC events since CAL timings calculated using hadronic system only.

Events are required to satisfy all the following conditions:

$$|T_F| > 5 \text{ ns and } E_F > 3 \text{ GeV and } N_F \geq 2, \quad (6.46)$$

$$|T_F| > 6 \text{ ns and } E_F > 0.6 \text{ GeV and } N_F \geq 2, \quad (6.47)$$

$$(T_B > 5 \text{ ns or } T_B < -5 \text{ ns}) \text{ and } E_B > 3 \text{ GeV and } N_B \geq 2, \quad (6.48)$$

$$(T_R > 7 \text{ ns or } T_R < -5 \text{ ns}) \text{ and } E_R > 1.5 \text{ GeV and } N_R \geq 2, \quad (6.49)$$

$$|T_G| > 5 \text{ ns and } E_G > 0.6 \text{ GeV and } N_G \geq 2, \quad (6.50)$$

$$(T_F^U > 6 \text{ ns or } T_F^U < -5 \text{ ns}) \text{ and } E_F^U > 4 \text{ GeV and } N_F^U \geq 2, \quad (6.51)$$

$$|T_F^D| > 7 \text{ ns and } E_F^D > 3 \text{ GeV and } N_F^D \geq 2, \quad (6.52)$$

$$(T_B^U > 6 \text{ ns or } T_B^U < -5 \text{ ns}) \text{ and } E_B^U > 5 \text{ GeV and } N_B^U \geq 2, \quad (6.53)$$

$$|T_B^D| > 6 \text{ ns and } E_B^D > 3 \text{ GeV and } N_B^D \geq 2, \quad (6.54)$$

$$|T_G^U| > 5 \text{ ns and } E_G^U > 4 \text{ GeV and } N_B^U \geq 2, \quad (6.55)$$

$$|T_G^D| > 6 \text{ ns and } E_G^D > 6 \text{ GeV and } N_B^D \geq 2, \quad (6.56)$$

$$|T_F^U - T_F^D| > 6 \text{ ns and } \min(E_F^U, E_F^D) > 3 \text{ GeV and } \min(N_F^U, N_F^D) \geq 2, \quad (6.57)$$

$$|T_B^U - T_B^D| > 6 \text{ ns and } \min(E_B^U, E_B^D) > 3 \text{ GeV and } \min(N_B^U, N_B^D) \geq 2, \quad (6.58)$$

$$|T_R^U - T_B^D| > 6 \text{ ns and } \min(E_R^U, E_R^D) > 1 \text{ GeV and } \min(N_R^U, N_R^D) \geq 2, \quad (6.59)$$

$$|T_G^U - T_G^D| > 6 \text{ ns and } \min(E_G^U, E_G^D) > 2 \text{ GeV and } \min(N_G^U, N_G^D) \geq 2, \quad (6.60)$$

$$(T_F - T_R > 6 \text{ ns or } T_F - T_R < -7 \text{ ns}) \text{ and } \min(E_F, E_R) > 1.5 \text{ GeV,} \\ \text{and } \min(N_F, N_R) \geq 2, \quad (6.61)$$

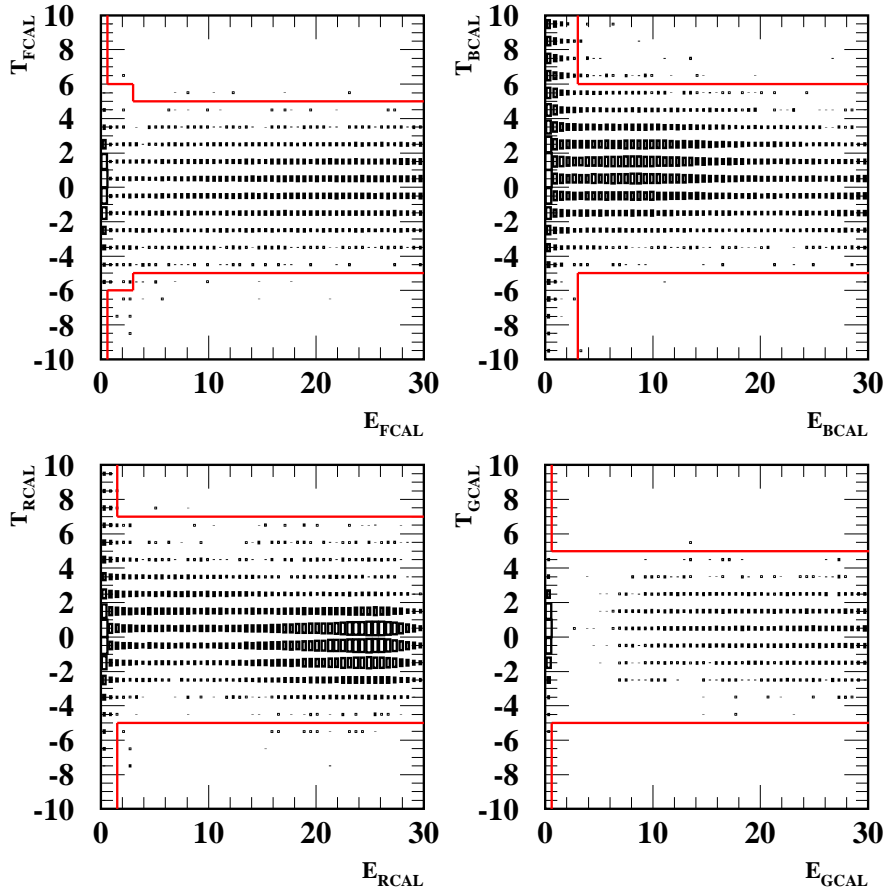


Figure 6.14: The correlation of energy, E , and CAL timing, T , in FCAL,BCAL, RCAL and global calorimeter

where the subscript ' F, B, R, G ' denote FCAL, BCAL, RCAL and GCAL, respectively. And superscripts U and D are the upper and lower halves of CAL. These cuts are composed of an CAL timing T , the number of signalled PMTs N and total Energy of CAL, E .

Solid lines denote the above threshold of each condition(Eq.6.47-6.61) in Figure 6.14-6.17. Figure 6.14 shows the correlation of energy and timing in each section and global CAL with NC real data excluding a electron candidate(Eq.6.47-6.50). Asymmetric timing cuts are applied in BCAL and RCAL due to shift to positive direction. Figure 6.15 shows the correlation between energy and CAL timing in the upper and lower halves of CAL(Eq.6.52-6.56). The differences between the upper and lower halves of CAL are shown in Figure 6.16(Eq.6.58-6.61). The requirements

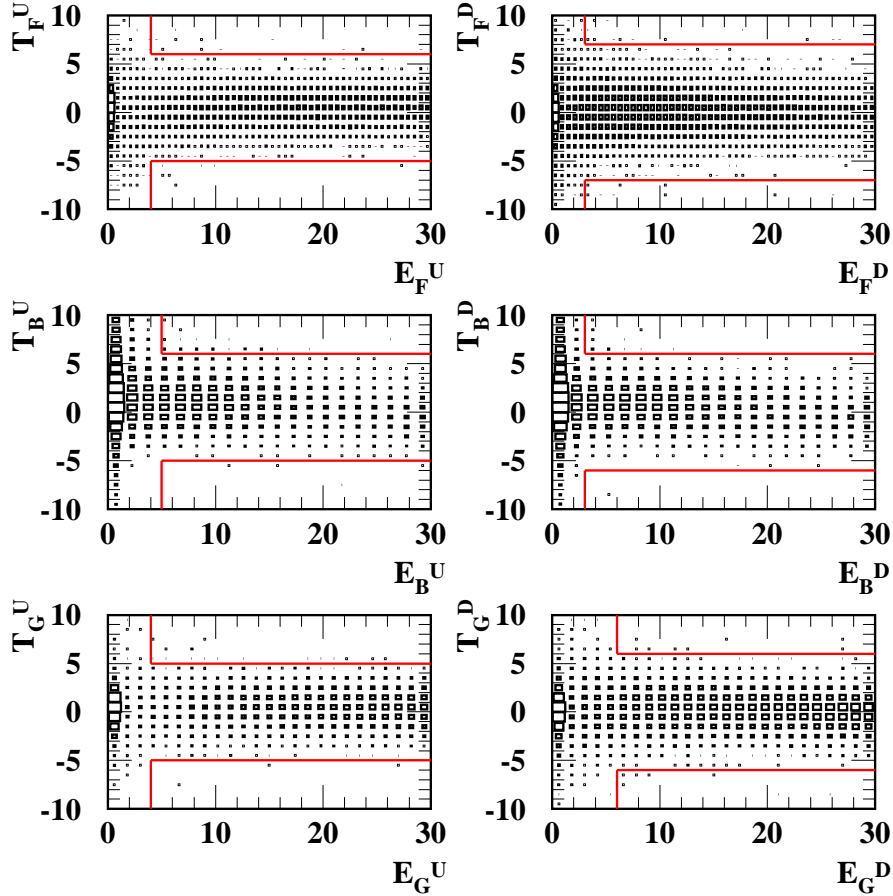


Figure 6.15: The correlation between energy and CAL timing in the upper and lower of halves of CAL.

of the CAL timing difference between the upper and lower halves of CAL are strong cut against cosmic-ray. In order to reject halo-muon events, the timing difference between FCAL and RCAL(6.17) is required in Eq.6.61.

6.4.4 Summary of CC DIS selection

Various selection criteria are introduced in this chapter. After all selection, we visually rejected 11(7) events as cosmic or halo-muon event in $P = +32.6$ (-40.2) % data. Finally, 519 and 182 CC DIS candidates are observed for e^+p data with $P = +32.6$ % and $P = -40.2$ %, respectively. The scattered plot in the Q^2 and

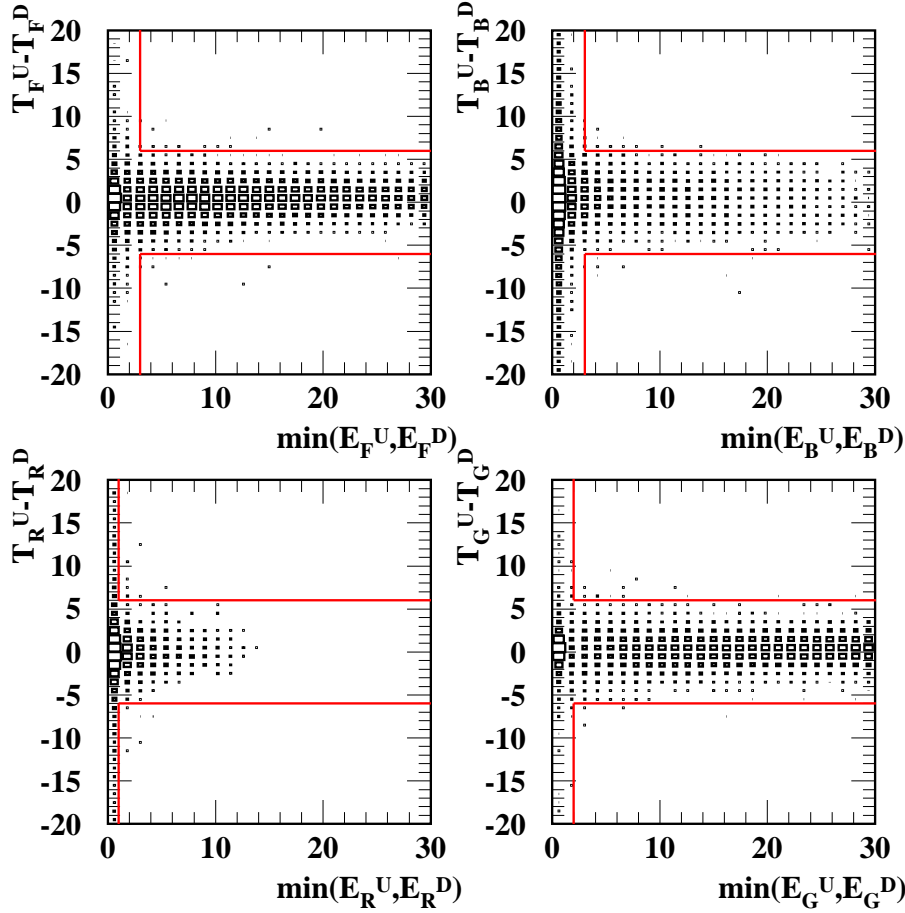


Figure 6.16: The correlation between energy and CAL timing in the upper and lower halves of CAL.

x plane for them is shown in Figure 6.18. The distributions ($P_{T,miss}$, Q^2 , x , y , $P_{T,miss}/E_T$ and Z_{vtx}^{CTD}) for the final CC candidates are shown in Figure 6.19. It is found that MC describes data well.

In order to show the effect of each selection, efficiency, \mathcal{E}_{sel} , is defined as follows:

$$\mathcal{E}_{sel} = \frac{\text{Number of events generated in the bin and passed the event selection}}{\text{Number of events generated in the bin}}. \quad (6.62)$$

Table 6.1 is summaries the efficiency of each slot from MC and remaining number of

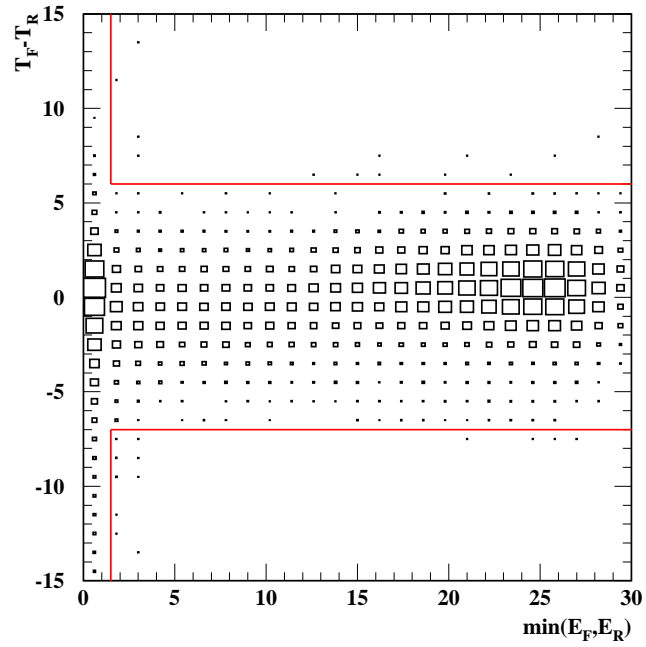
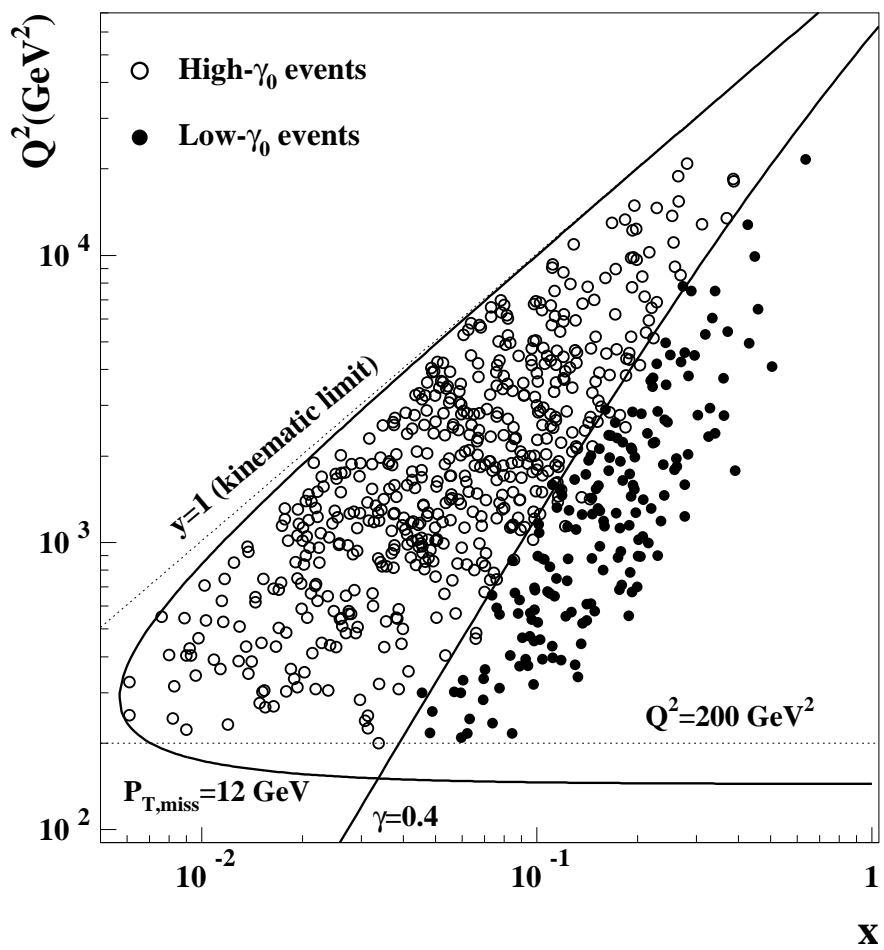


Figure 6.17: The correlation between energy and CAL timing in the upper and lower halves of CAL.

data events after each cut. The difference of efficiency between the two polarisations is due to the difference of the vertex distribution, as mentioned in Section 5.3. After all selection, the efficiencies of both two data samples become around 53 %.

Systematic items	$P = +32.6 \%$		$P = -40.2 \%$	
	MC(\mathcal{E}_{sel} %)	DATA(event)	MC(\mathcal{E}_{sel} %)	DATA(event)
FLT	82.2	–	80.8	–
SLT	81.9	–	80.5	–
TLT	81.9	–	80.4	–
pre-selection	80.1	290084	78.7	190935
vertex requirement	79.2	42316	77.8	28562
kinematics requirement	75.3	21089	73.9	13187
$P_{T,miss}$ and $P_{T,miss}(-1ir)$	72.0	13946	70.7	8385
PhP rejection	64.3	11553	63.2	6577
NC DIS rejection	64.2	11531	63.1	6558
Tracking cut	55.7	6500	54.6	3751
$d\phi$ cut	55.0	6041	54.0	3588
Halo- and Cosmic-muon rejection	54.1	1103	53.1	347
Non- e^+p rejection	54.1	544	53.1	197
CAL-timing cut	53.7	530	52.7	189
eye-scanning	53.7	519	52.7	182

Table 6.1: A summary of selection cuts and their efficiencies

Figure 6.18: The scattered plots of final CC candidates in the Q^2 - x plane

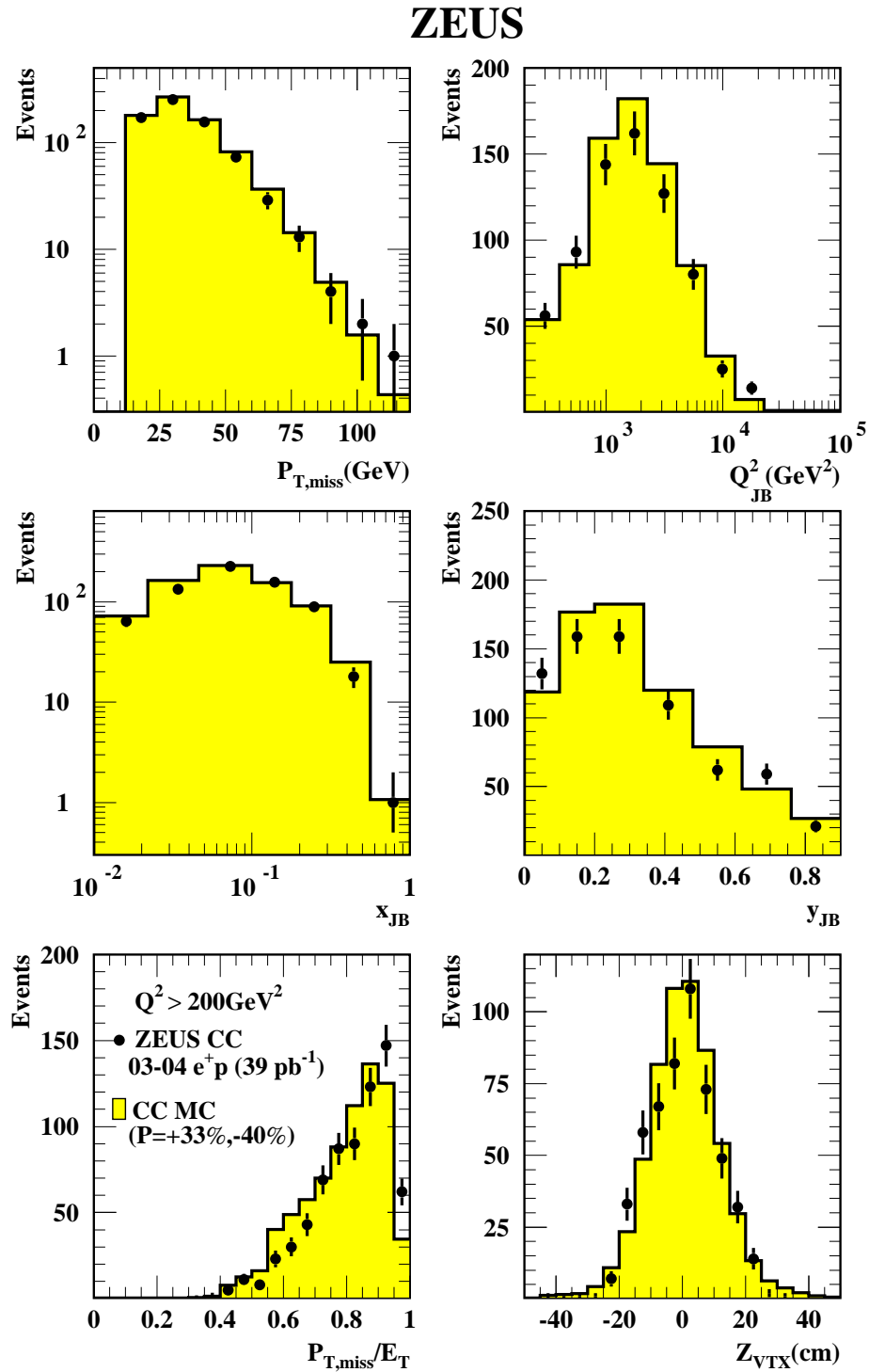


Figure 6.19: Distributions of CC final candidates: histogram denotes CC MC and closed circles denote CC final candidates.

Chapter 7

CROSS SECTION MEASUREMENTS

In this chapter, the procedures to measure the charged current DIS cross section are presented in detail. The measurements of the total cross section and single differential cross section are done through 'unfolding' steps as background subtraction, acceptance correction and radiative correction. The statistical and systematic uncertainties are also discussed here.

7.1 Outline

The measured distributions shown in Figure 6.19 are different with the true ones due to detector effects. The cross section is extracted bin by bin of the various kinematic variables correcting for their effects. The measured average cross section σ_i^{rad} for the i -th bin of kinematic variables X can be written as

$$\sigma_i^{rad} \equiv \frac{\int_i \frac{d\sigma_i}{dX_i} dX}{\int_i dX}, \quad (7.1)$$

$$= \frac{N_i^{data} - N_i^{bg}}{\mathcal{A}\mathcal{L}}, \quad (7.2)$$

where N_i^{data} and N_i^{bg} are the number of observed data events and estimated background events in the i -th bin, respectively. \mathcal{L} is the total integrated luminosity. \mathcal{A} is acceptance correction. The superscript 'rad' is put in order to explicitly state that the measured cross section is a subject to the electroweak radiative correction. It is preferable to convert to the Born level cross section, to make a comparison to the theory. The procedure is described in Section 7.5. Finally, the differential cross section at the bin centre, $\frac{d\sigma}{dX}|_{X=X_c}$ is obtained (see Section 7.6).

7.2 Bin definition for differential cross section

The single differential cross sections are measured as a function of Q^2 , x and y . Their bin size is determined as follows. It is preferable to make the bin size as narrow as possible to make a comparison with the theories, but the statistical error and the migration effects limit at a certain point. The binning is determined with the bin width of several times of the kinematic resolution.

Since $Q^2 \propto P_{T,miss}^2$, the $\Delta Q^2/Q^2$ is almost constant. It is, therefore natural to logarithmically divide the Q^2 bins for single differential cross section $d\sigma^2/dQ^2$ measurements. The Q^2 range 200 – 60000 GeV² are divided in nine bins. First eight bins divide the Q^2 range, 200 – 22494 GeV², with same width in $\log Q^2$. The highest Q^2 bin covers the Q^2 range, 22494 – 60000 GeV². For the single differential cross section $d\sigma/dx$, seven bins are used for the whole x range, 0.01 – 1.0. First the x range of 0.01 – 0.1 is divided by three bins with equal width in $\log x$. The other four bins divide x range of 0.1 – 1.0 with equal width in $\log x$. For the single differential cross section $d\sigma/dy$, total seven bins divide y range of 0.0 – 0.9. Since the y distribution is steeper at low y , the y range of 0.0 – 0.2 is divided into two bins with equal width and y range 0.2 – 0.9 is into five bins with equal width. The resolutions of measured Q^2 , x and y are shown in Figure 7.1-7.3.

7.3 Background estimation

The background contamination was estimated using various MC samples, NC DIS, PhP and W production. Table 7.3 shows the amount of background contamination. The effects from NC DIS and W production were found to be very small ($\leq 0.1\%$). The PhP was found to be the largest background source, giving 4 % contamination to data for $P = +32.6\%$ and 7 % for $P = -40.2\%$ in the lowest Q^2 bin. The contamination is larger for negative polarisation sample, simply because the signal (CC) cross section is smaller while PhP cross sections is independent to the polarisation. The PhP cross section predicted by the MC has a large uncertainty because it is leading-order (LO) calculation. The uncertainty is investigated in the later Section 7.8.4.

7.4 Acceptance correction

At measuring the cross section, the acceptance correction is needed in order to correct detector acceptance and migration effects. As seen in Figure 6.19, the CC

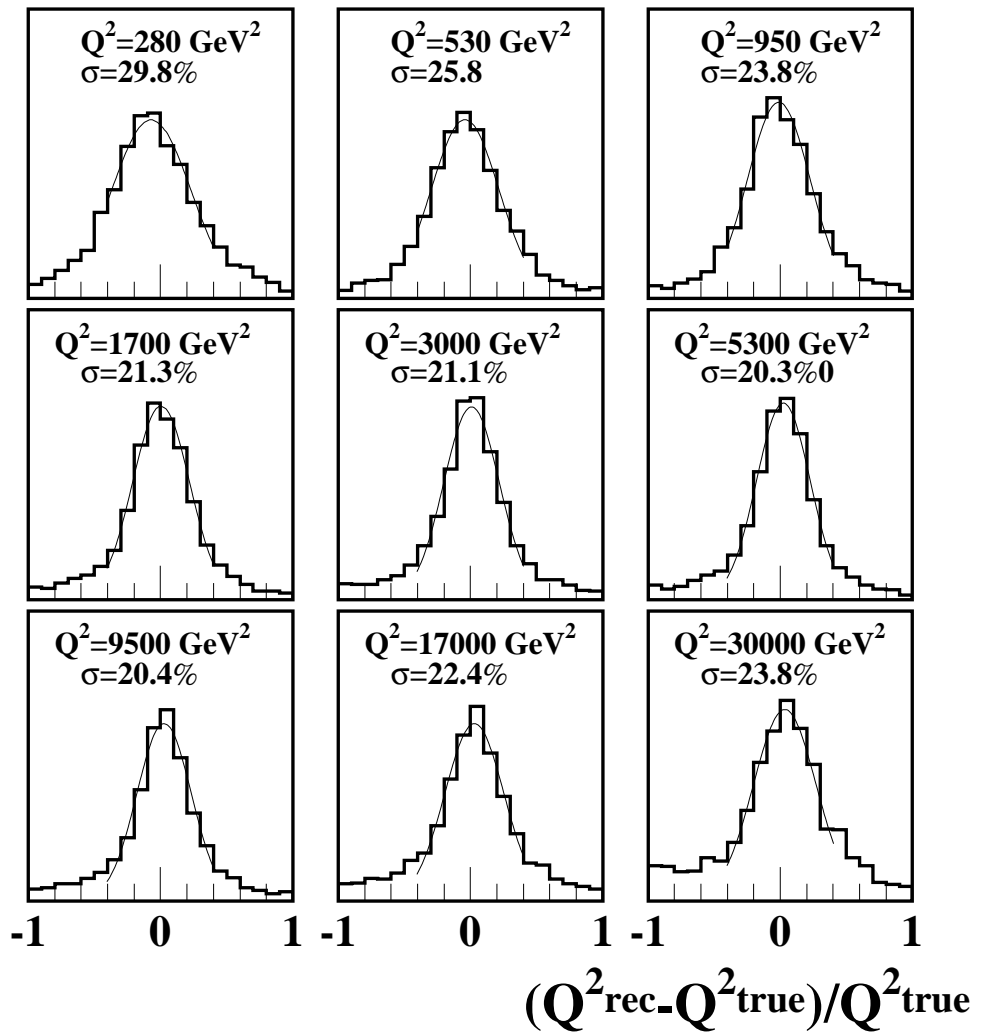


Figure 7.1: The resolution of the measured Q^2 is shown in each bin of Q^2_{true}

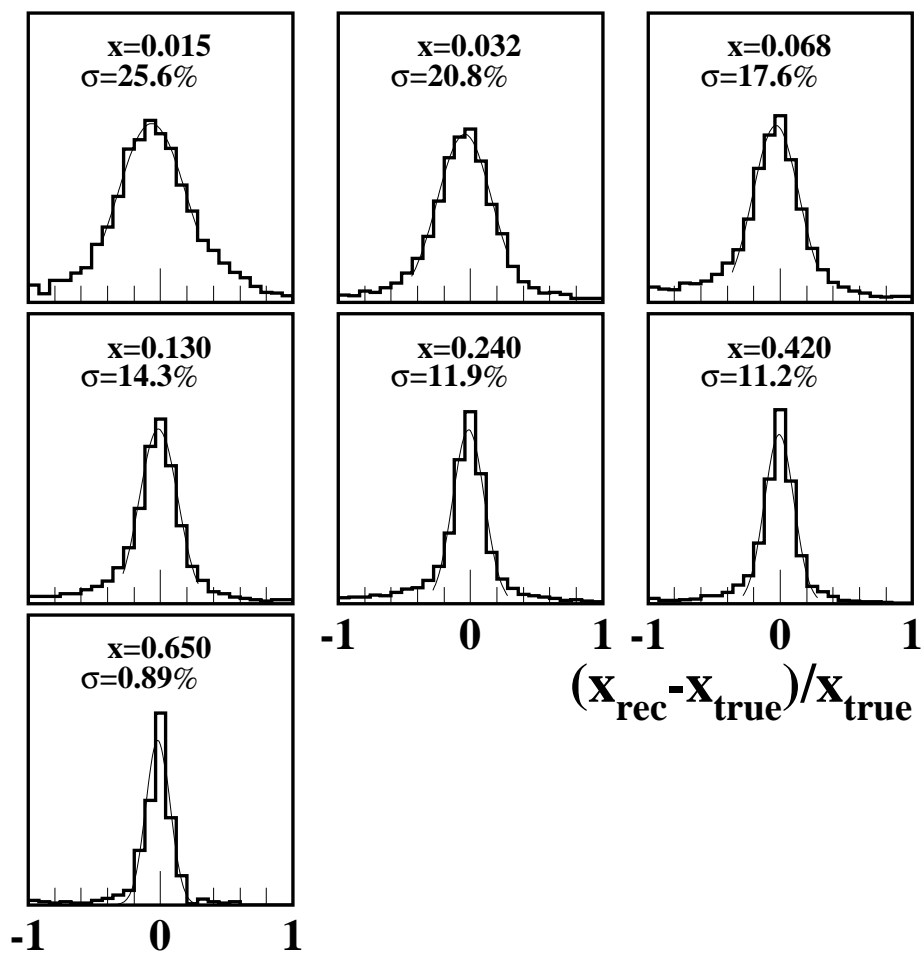


Figure 7.2: The resolution of the measured x is shown in each bin of x_{true}

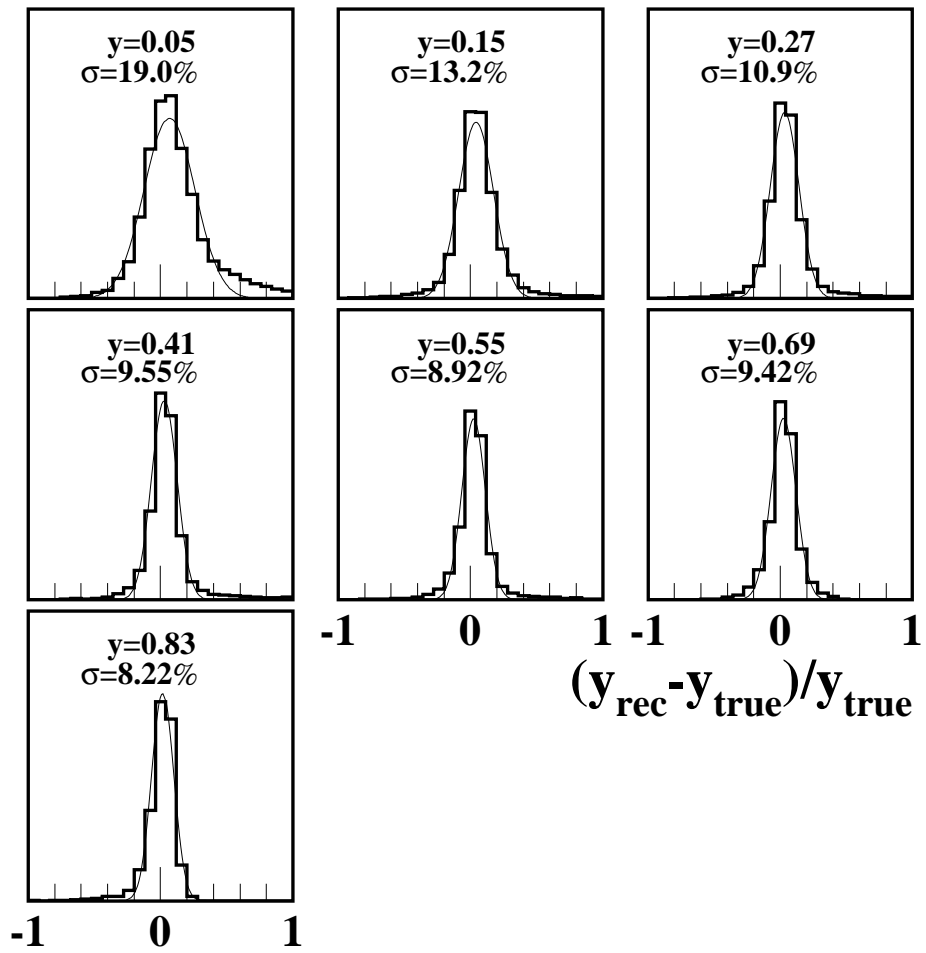


Figure 7.3: The resolution of the measured y is shown in each bin of y_{true}

Q^2 range (GeV^2)	N_{obs}	N_{PhP}	N_{NC}	N_{W^\pm}	N_{bg}
200- 400	40	1.55	0.0	0.0	1.55
400- 711	67	0.09	0.0	0.0	0.09
711- 1265	101	0.75	0.0	0.0	0.76
1265- 2249	119	0.13	0.0	0.0	0.13
2249- 4000	96	0.63	0.181	0.0	0.81
4000- 7113	68	0.0	0.0	0.0	0.0
7113- 12469	18	0.0	0.0	0.0	0.0
12469- 22494	10	0.0	0.0	0.0	0.0
22494- 101274	0	0.0	0.0	0.0	0.0
Total	519	3.15	0.18	0.0	3.34
Q^2 range (GeV^2)	N_{obs}	N_{PhP}	N_{NC}	N_{W^\pm}	N_{bg}
200- 400	16	1.09	0.0	0.0	1.09
400- 711	26	0.07	0.0	0.0	0.07
711- 1265	43	0.59	0.0	0.0	0.59
1265- 2249	43	0.11	0.0	0.0	0.11
2249- 4000	31	0.41	0.12	0.0	0.53
4000- 7113	12	0.0	0.0	0.0	0.0
7113- 12469	7	0.0	0.0	0.0	0.0
12469- 22494	4	0.0	0.0	0.0	0.0
22494- 101274	0	0.0	0.0	0.0	0.0
Total	182	2.27	0.12	0.0	2.39

Table 7.1: Number of background event expected by MC samples. Upper table is results for $P = +32.6\%$ and lower is for $P = -40.2\%$. N_{bg} denotes sum of all background.

MC describes the measured distribution fairly well. The acceptance \mathcal{A} for each bin is estimated with the CC MC. In the MC, true values of the kinematic variables are known. By making the histograms both for generated (true) values and measured values, acceptance correction is calculated in bin-by-bin as

$$\mathcal{A} = \frac{\text{Number of events measured in the bin}}{\text{Number of events generated in the bin}}. \quad (7.3)$$

As a measure of the behaviour of the correction, efficiency (\mathcal{E}) and purity (\mathcal{P}) are also defined as

$$\mathcal{E} = \frac{\text{Number of events generated and measured in the bin}}{\text{Number of events generated in the bin}}, \quad (7.4)$$

$$\mathcal{P} = \frac{\text{Number of events generated and measured in the bin}}{\text{Number of events measured in the bin}}. \quad (7.5)$$

The efficiency \mathcal{E} is further separated to selection efficiency \mathcal{E}_{sel} as defined in Section 6.4.4 and migration efficiency \mathcal{E}_{mig} as

$$\mathcal{E} = \mathcal{E}_{sel} \times \mathcal{E}_{mig},$$

where \mathcal{E}_{mig} is

$$\mathcal{E}_{mig} = \frac{\text{Number of events generated and measured in the bin}}{\text{Number of events generated in the bin and passed the event selection}}. \quad (7.6)$$

The \mathcal{E}_{sel} , \mathcal{E} , and \mathcal{A} of the two data sets with the different polarisation, $P = +32.6\%$ and $P = -40.2\%$, are shown in Figure 7.4-7.6. The behaviour of acceptance correction in each distributions are smooth. The acceptance falls to about 20% in low Q^2 since selection efficiency is low due to the tight tracking cut. The differences between the two polarisations come from the difference of the vertex distribution, as mentioned in Section 5.3.

7.5 Born cross section

The Born level cross section is obtained by correcting the effect using the radiative correction factor \mathcal{C}_i^{rad} as follows:

$$\sigma_i^{Born} = \sigma_i^{rad} \cdot \mathcal{C}_i^{rad}, \quad (7.7)$$

\mathcal{C}_i^{rad} is determined as

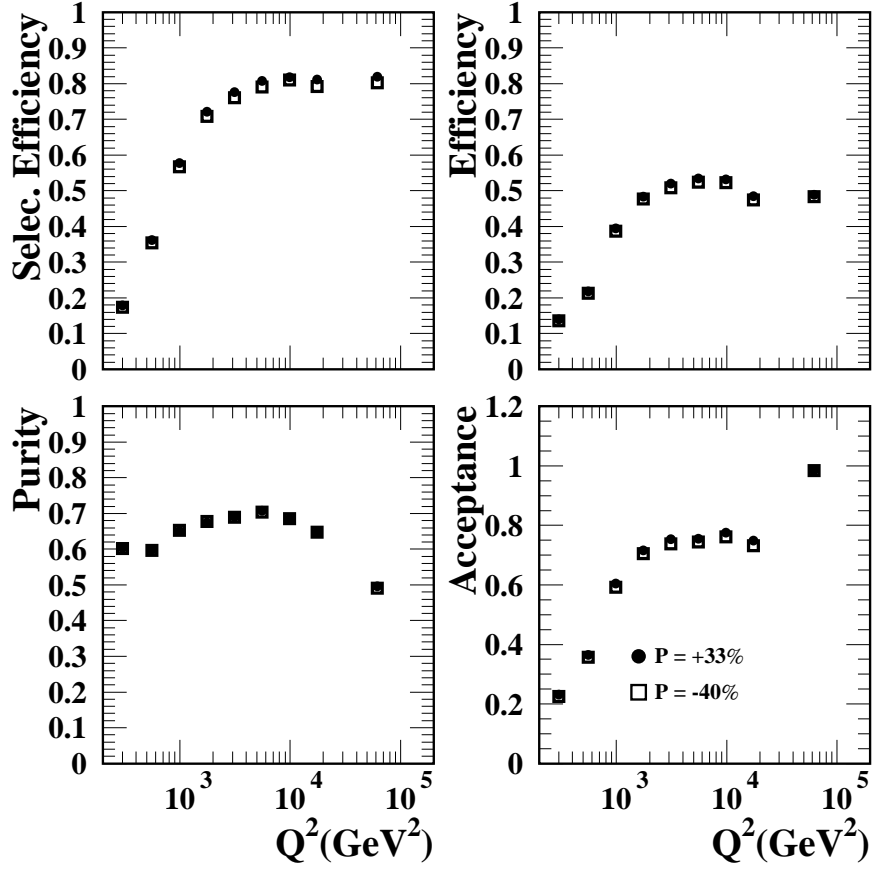


Figure 7.4: Selection efficiency(left-upper), Efficiency(right-upper), Purity(left-lower) and Acceptance(right-lower) in each bin of Q^2 are shown. Closed circle denotes data with $P = + 32.6 \%$ and opened square with $P = - 40.2 \%$

$$C_i^{rad} = \frac{\sigma_i^{Born(SM)}}{\sigma_i^{rad(SM)}}, \quad (7.8)$$

where $\sigma_i^{Born(SM)}$ and $\sigma_i^{rad(SM)}$ are the integrated Standard Model(SM) cross section in Born level and radiative level, respectively. The $\sigma_i^{rad(SM)}$ is the cross section at generating MC events and $\sigma_i^{Born(SM)}$ is determined using DJANGO.

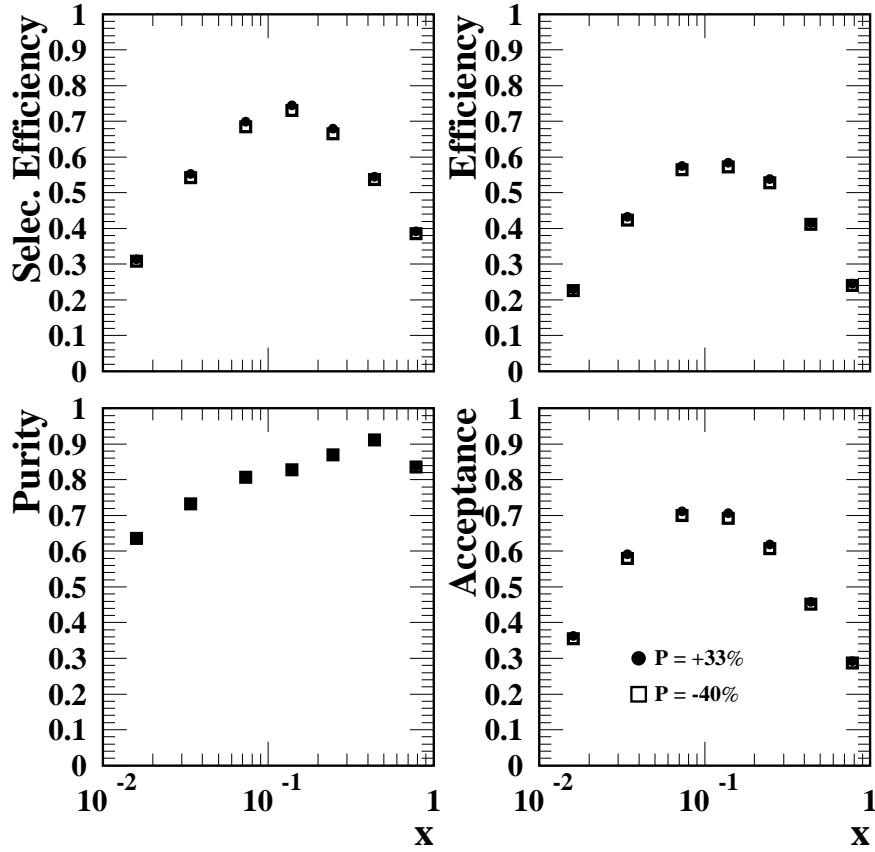


Figure 7.5: Selection efficiency(left-upper), Efficiency(right-upper), Purity(left-lower) and Acceptance(right-lower) in each bin of x are shown. Closed circle denotes data with $P = + 32.6 \%$ and opened square with $P = - 40.2 \%$

7.6 Bin centring correction

In order to measure the differential cross section at a bin centring point in the bin, a bin centring correction is needed. For the differential cross section in Q^2 this bin centring correction factor was defined as

$$C_i^{centre} = \frac{d\sigma_i^{Born(SM)}(Q^2)}{dQ^2} \Big|_{Q^2=Q_c^2}. \quad (7.9)$$

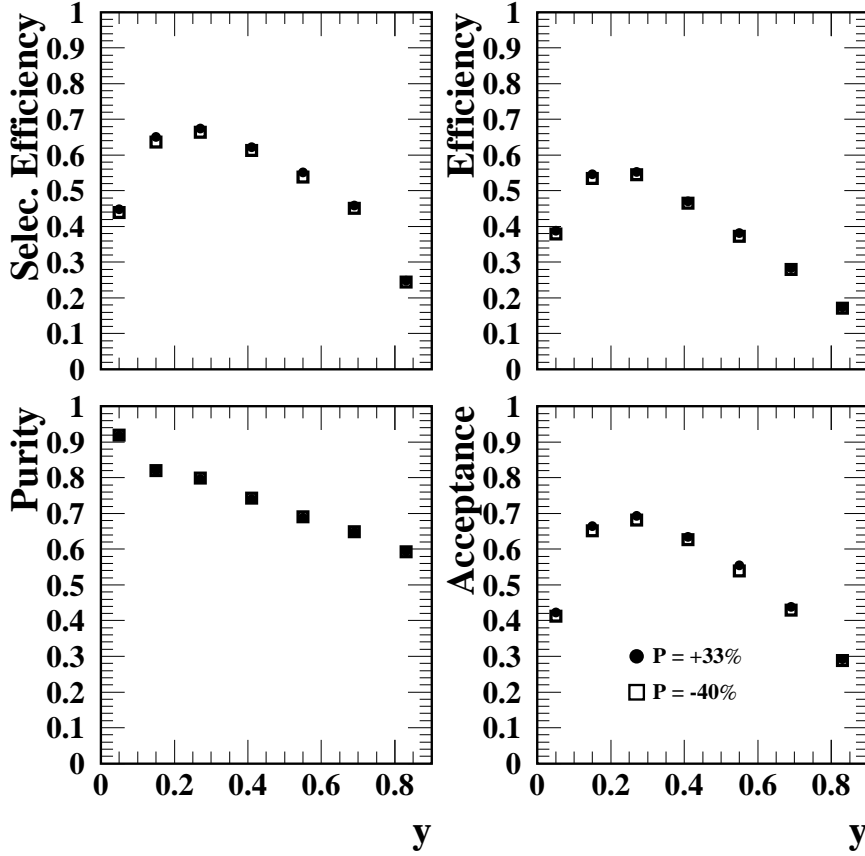


Figure 7.6: Selection efficiency(left-upper), Efficiency(right-upper), Purity(left-lower) and Acceptance(right-lower) in each bin of y are shown. Closed circle denotes data with $P = + 32.6 \%$ and opened square with $P = - 40.2 \%$

where the upper term, $d\sigma_i^{Born(SM)}(Q^2)/dQ^2|_{Q^2=Q_c^2}$, is the SM Born level differential cross section at the bin centring point Q_c^2 . Hence, the Born level differential cross section in Q^2 at the bin centring point Q_c^2 is obtained as

$$\frac{d\sigma_i^{Born}(Q^2)}{dQ^2}|_{Q^2=Q_c^2} = C_i^{centre} \sigma_i^{Born}(\Delta Q^2). \quad (7.10)$$

Combining Eq.7.9 and Eq.7.10, the Born level differential cross section can be written as follows:

$$\frac{d\sigma_i^{Born}(Q^2)}{dQ^2}\Big|_{Q^2=Q_i^2} = \frac{\sigma_i^{Born}}{\sigma_i^{Born(SM)}} \cdot \frac{d\sigma_i^{Born(SM)}}{dQ^2}\Big|_{Q^2=Q_i^2} \quad (7.11)$$

7.7 Total cross section

As shown in Figure 6.19, MC describes data well in all kinematic phase space. Therefore, we can measure total cross section. The procedure is the same to the differential cross section. we consider the region of $Q^2 > 200\text{GeV}^2$ and $y > 0.9$ as one bin and the cross section is measured in the region $Q^2 > 200\text{ GeV}^2$ and $y < 0.9$. \mathcal{A} and \mathcal{E} are 0.56 and 0.55 for data with $P = +32.6\%$, respectively. For data with $P = -40.2\%$, \mathcal{A} and \mathcal{E} are 0.55 and 0.54, respectively. We extrapolate y region from 0.9 to 1.0 using DJANGO.

7.8 Systematic uncertainties

The source of systematic uncertainties in this analysis are categorised to five items, the calorimeter energy scale, the selection procedure, MC dependence, trigger efficiency and background subtraction. The uncertainties due to them are estimated. In particular, the uncertainty for the total cross section is summarised at the end of this section to be used in the discussion in Section 7.8.6.

7.8.1 Calorimeter energy scale

The reconstruction of kinematic variables for CC DIS events fully depends on the energy measurements with the calorimeter as mentioned in Section 5.1. So the energy scale of CAL gives a large effect to the cross section. The uncertainty in the absolute scale of the hadronic energy measurement was studied by comparing the reconstructed hadronic transverse momenta by the Jacquet-Blondel method and the Double Angle method using the NC DIS samples [34][35]. The uncertainty is found to be at most 2 % for the FCAL and the BCAL, and 3 % for the RCAL. The systematic uncertainty is estimated by changing the energy scale in the reconstruction for the MC sample as

$$\delta_{\pm} = \frac{N_{\pm}^{MC} - N_0^{MC}}{N_0^{MC}}, \quad (7.12)$$

where δ_{\pm} is the fractional systematic errors. The N_{\pm}^{MC} and N_0^{MC} represent the number of MC events with and without shifting the CAL energy scale. The energy scale in the MC was varied by $\pm 2\%$ in FCAL and BCAL, and by $\pm 3\%$ in RCAL separately. And then we estimate total uncertainty from CAL energy scale by quadratic summation. Figure 7.7 shows dominant sources are FCAL for high x and BCAL for high y , which are understood from the direction of the hadronic system.

7.8.2 Selection procedures

Many thresholds are set in the event selection. If the MC does not perfectly describe the real world, the bin-by-bin correction method used in this analysis gives systematic bias. This is estimated by changing thresholds in the various selection. Table 7.8.2 shows the summary of the systematic check categories and their varied thresholds for the selection variables. The varied amounts of thresholds are basically determined by the resolution of the variables. The uncertainty on the cross section due to the selection threshold variation was obtained from the difference between the nominal acceptance correction and the acceptance correction calculated with the threshold variation as follows:

$$\delta i = \frac{\mathcal{A}^i - \mathcal{A}^0}{\mathcal{A}^0}, \quad (7.13)$$

where \mathcal{C}_{acc}^i is the acceptance correction with the threshold variation and \mathcal{C}_{acc}^0 is the acceptance correction unfolded with the nominal selection.

Systematic uncertainties due to main selection threshold are shown in Figure 7.8. The largest uncertainty comes from the shift of N_{track}^{good} threshold in the tight tracking cut. It reached to 25 % at low Q^2 bins ($Q^2 < 400 \text{ GeV}^2$).

7.8.3 Monte Carlo fragmentation model

The acceptance is calculated using MC with the colour dipole model (CDM) for the fragmentation. As mentioned in Section 4.1, the matrix element parton shower (MEPS) describes QCD effect of the higher order better than CDM. Systematic uncertainty due to the fragmentation is estimated by comparing MEPS and CDM. Systematic uncertainty is defined as

$$\pm \delta_{frag.} = \pm \left| \frac{\mathcal{A}_{MEPS} - \mathcal{A}_{CDM}}{\mathcal{A}_{CDM}} \right|. \quad (7.14)$$

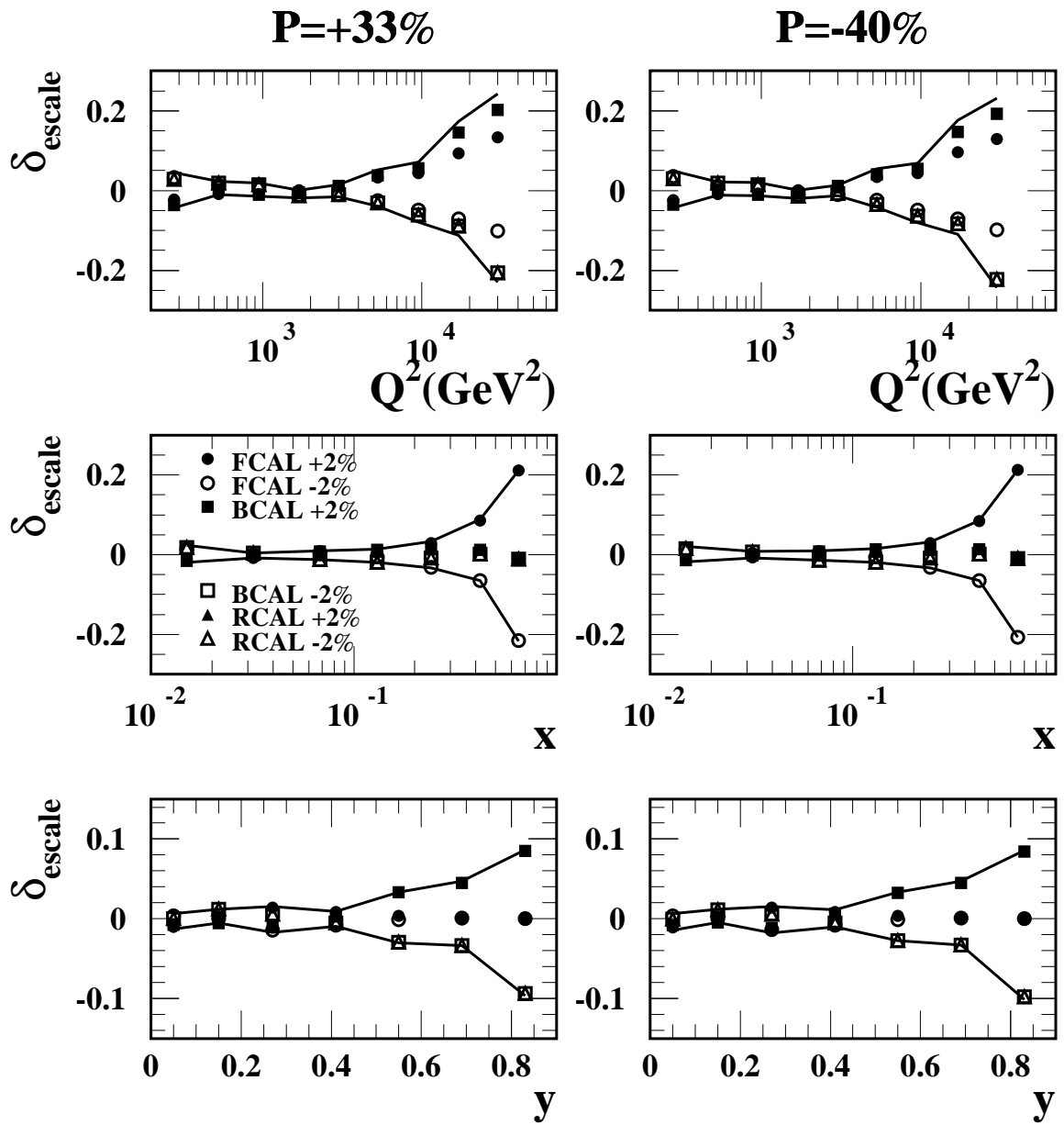


Figure 7.7: Systematic uncertainty due to the calorimeter energy scale: Line denotes total uncertainty from the calorimeter energy scale.

The large uncertainty is 6 % in low Q^2 region, 3 % in low x region. In the whole y region, the uncertainty is 2 ~ 6 %.

Selection	Shifted threshold
$P_{T,miss}$ for high- γ_0	12 ± 1.2 GeV
$P_{T,miss}$ for low- γ_0	14 ± 1.4 GeV
$P_{T,miss}(-1ir)$ for low- γ_0	12 ± 1.2 GeV
$P_{T,miss}$ for $P_{T,miss}/E_T$ cut	20 ± 2.0 GeV
$P_{T,miss}/E_T$ for high- γ_0	0.4 ± 0.04
$P_{T,miss}$ for the tight tracking cut	25 ± 2.5 GeV
P_T^{trk} for good track definition	$0.2 + 0.02$ GeV
θ^{trk} for good track definition	$15 + 1.5^\circ$
Tight tracking cut	$N_{trk}^{good} \rightarrow N_{trk}^{good} - 1$
Tight tracking cut	$N_{trk} \rightarrow N_{trk} + 1$
$ d\phi $ cut for $P_{T,miss} > 30$ GeV	2.0 ± 0.2 radian
$ d\phi $ cut for $P_{T,miss} < 30$ GeV	1.0 ± 0.1 radian

Table 7.2: Systematic check categories and varied threshold of selection variables

7.8.4 Background subtraction

The dominant background source is the PhP event at low Q^2 . Figure 7.9 shows the $P_{T,miss}/E_T$ distribution of the high- γ_0 events with $200 < Q^2 < 400$ GeV², which are selected using all the selection except for $P_{T,miss}/E_T$ cut. At low $P_{T,miss}/E_T$, a peak from the PhP is clearly seen. Since the absolute cross section of PhP MC is known to have a large uncertainty, the cross section is evaluated by using this distribution. The χ^2 is defined as

$$\chi^2 \equiv \sum_i \frac{(N_{data}^i - f_{PhP} \cdot (N_{res}^i + N_{dir}^i) - N_W^i - f_{CC} \cdot N_{CC}^i)^2}{(\delta N_{data}^i)^2 + f_{PhP}^2 \cdot (\delta N_{res}^i + \delta N_{dir}^i)^2 + (\delta N_W^i)^2 + f_{CC}^2 (\delta N_{CC}^i)^2}, \quad (7.15)$$

where N_{data} , N_{res} , N_{dir} , N_W and N_{CC} are the number of the data, the resolved PhP MC, the direct PhP MC, the single W production MC and the CC MC events, respectively. The superscript means i -bin. The f_{CC} introduced to constrain the total number of events; i.e.

$$f_{CC} \equiv \frac{\sum_i (N_{data}^i - f_{PhP} \cdot (N_{res}^i + N_{dir}^i) - N_W^i)}{\sum_i N_{CC}^i}. \quad (7.16)$$

The fit resulted in f_{PhP} is 0.57 ± 0.09 . Therefore, it seems that the PhP MC overestimate the cross section by 40 %. To be conservative, the systematic uncertainty for the CC cross section is obtained using the normalisation factor shifted by ± 40 % from the MC prediction as

$$\delta_{\pm}^{PhP} = \frac{N_{obs}^{MC,\pm} - N_{obs}^{MC,0}}{N_{obs}^{MC,0}}, \quad (7.17)$$

where the $N_{obs}^{MC,\pm}$ and $N_{obs}^{MC,0}$ are the number of events expected with all MC as

$$N_{obs}^{MC,\pm} = (1 \pm 0.4) \cdot (N_{res}^i + N_{dir}^i) + N_W^i + N_{CC}^i, \quad (7.18)$$

$$N_{obs}^{MC,0} = N_{res}^i + N_{dir}^i + N_W^i + N_{CC}^i. \quad (7.19)$$

The systematic uncertainty for the total cross section is 0.2(0.4) % on the data with $P = +32.6(-40.2)$ %. The largest error is 1.5(3) % in the lowest Q^2 bin, 0.3(0.7) % in the lowest x bin, and 0.5(1.0) % in the lowest y bin for the data with $P = +32.6(-40.2)$ %, respectively. The difference of the error between the polarisation comes from the number of CC events expected by MC, N_{CC}^i . Because only this number is affected by the polarisation.

7.8.5 Trigger efficiency

CC DIS events are mainly selected with $P_{T,miss}^{FLT}$ at the FLT. Since $P_{T,miss}^{FLT}$ resolution is worse than the offline analysis level, it is important to check the efficiency of the threshold. Figure 7.10 shows the FLT trigger slot60 efficiency measured using events triggered by the slot44, where the $P_{T,miss}^{FLT}$ is not used in the selection.

$\mathcal{E}_{eff}^{slot60}$ is defined as

$$\mathcal{E}_{eff}^{slot60} = \frac{\text{Number of events triggered by both the slot60 and slot44}}{\text{Number of events triggered by the slot44}}. \quad (7.20)$$

The efficiencies for both MC and DATA are fitted with a turn on curve, \mathcal{F} , with a form of

$$\mathcal{F} = 0.5 \cdot \tanh\left(\frac{P_{T,miss} - p}{q}\right) + 0.5, \quad (7.21)$$

where p and q represent the point where the efficiency turns on to 0.5 and the slope of the curve, respectively. The difference of fitted turn on curve between DATA and MC is treated as the uncertainty due to the FLT efficiency.

In the MC sample, the events passed with only slot60 are re-weighted with the difference w . Since slot40 requires at least one good track, the $P_{T,miss}^{FLT}$ threshold tested in this procedure is 5 or 8 GeV as seen in Eq.6.1 and 6.2. For event without track the threshold is higher to 11 GeV (Eq. 6.3). Therefore, in the re-weighting, event with/without a good track needs to be treated differently.

- For events with at least one good tracks,

$$w = \frac{\mathcal{F}_{data}}{\mathcal{F}_{MC}}, \quad (7.22)$$

$$= \frac{0.5 \cdot \tanh\left(\frac{P_{T,miss} - p_{DATA}}{q_{DATA}}\right) + 0.5}{0.5 \cdot \tanh\left(\frac{P_{T,miss} - p_{MC}}{q_{MC}}\right) + 0.5}, \quad (7.23)$$

- For events with no good tracks,

$$w = \frac{\mathcal{F}_{data}}{\mathcal{F}_{MC}}, \quad (7.24)$$

$$= \frac{0.5 \cdot \tanh\left(\frac{P_{T,miss} - (p_{DATA} + 3)}{q_{DATA}}\right) + 0.5}{0.5 \cdot \tanh\left(\frac{P_{T,miss} - (p_{MC} + 3)}{q_{MC}}\right) + 0.5}. \quad (7.25)$$

The systematic uncertainty due to the FLT trigger efficiency is estimated by the difference of the acceptance correction between with or without the re-weighting factor, w , which is obtained using the sample selected with the SLT, TLT, vertex requirement, $P_{T,miss}/E_T > 0.4$ cut, NC rejection and halo muon rejection. The uncertainty was below 0.1 % and was neglected.

7.8.6 Summary for systematic uncertainty

Various systematic uncertainties have been checked in this section. Figure 7.11 shows the systematic uncertainties as function of Q^2 , x , y . The largest effects which

are observed in the bins of lowest Q^2 and lowest x are about 25 %. These are due to the shifted of N_{track}^{good} threshold in the tight tracking cut for measurement. At high Q^2 and high x , the uncertainty of the CAL energy scale becomes the dominant source. The systematic uncertainties for the total cross section are summarised in Table 7.3. The largest systematic uncertainty is about 6 % due to the selection threshold, from the tight tracking cut.

Systematic items	$P = +32.6 \%$	$P = -40.2 \%$
CAL energy scale	$+0.68$ -0.69 %	± 0.68 %
Selection	± 6.2 %	± 6.2 %
Fragmentation	± 0.93 %	± 0.66 %
Trigger efficiency	negligible	negligible
Background Subtraction	± 0.18 %	± 0.40 %
total	± 6.3 %	± 6.5 %

Table 7.3: Systematic uncertainties for the total cross section

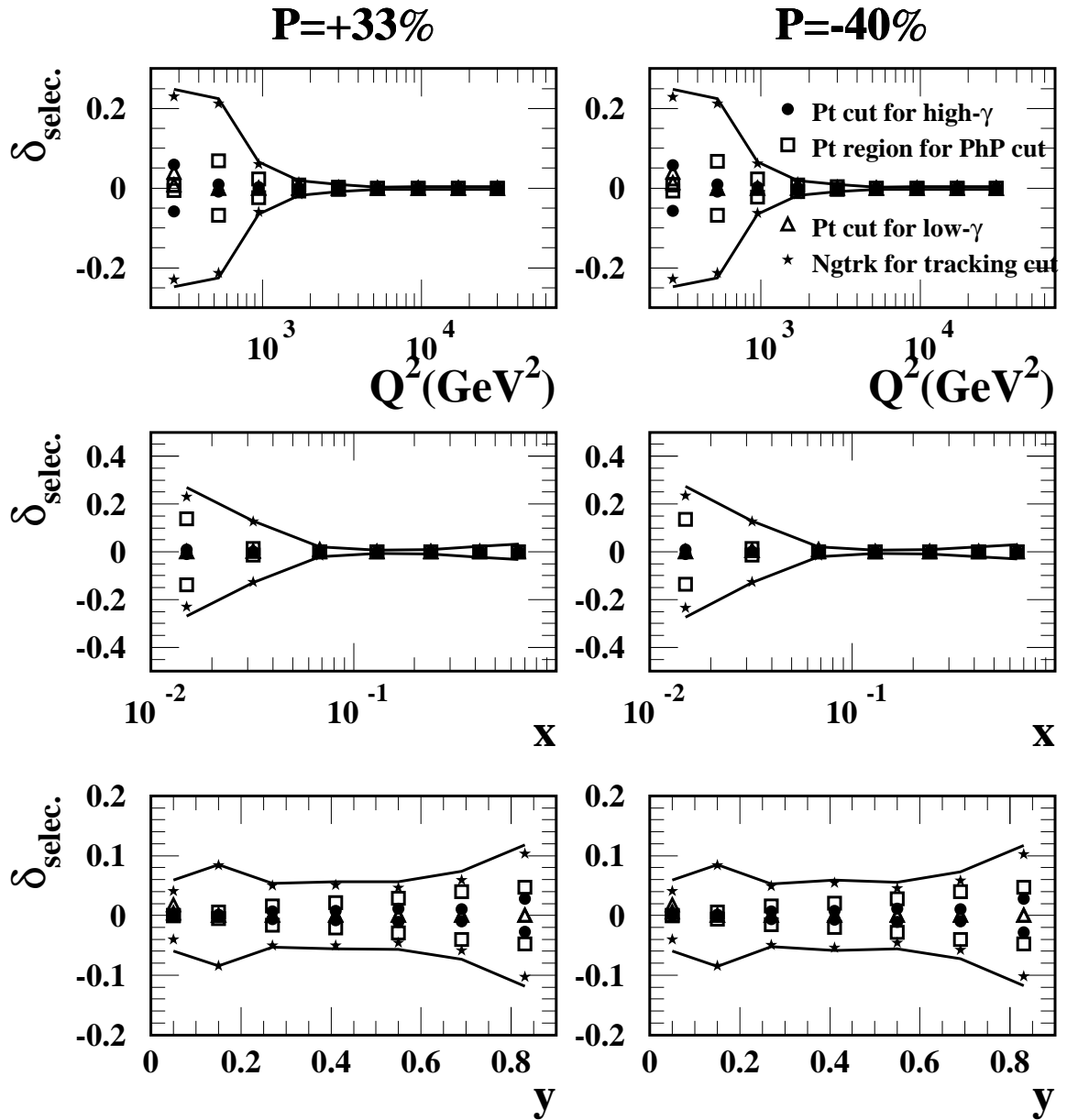


Figure 7.8: Systematic uncertainty due to the selection threshold: Closed circle denotes $d\phi$ cut for $P_{T,miss} > 30$ GeV. Star denote $N_{\text{trk}}^{\text{good}}$ shifted for tracking cut. Closed triangle denotes $P_{T,miss}/E_T$ cut for $20 < P_{T,miss} < 30$. Opened triangle denotes $P_{T,miss}$ cut for low- γ . Opened square denotes $P_{T,miss}$ region for PhP rejection. The solid line denotes total systematic uncertainty of all items in Table 7.8.2

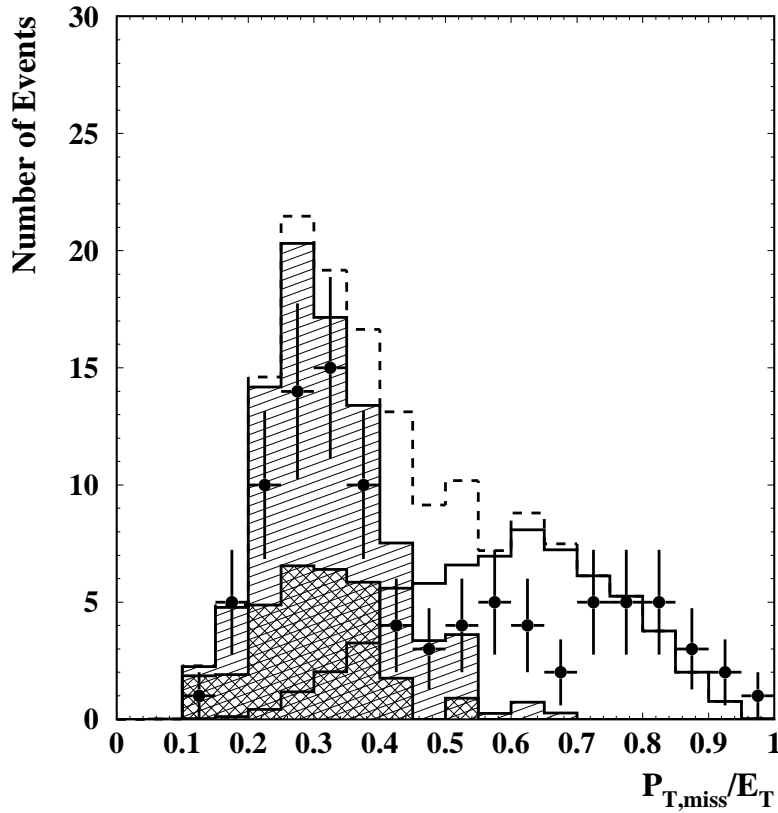


Figure 7.9: $P_{T,miss}/E_T$ distribution for the high- γ_0 events with $200 < Q^2 < 400 \text{ GeV}^2$. Closed circles denote all e^+p data and the solid histogram denotes the CC MC. The single shaded histogram is the sum of the resolved and direct PhP MC and the double shaded histogram is the direct PhP MC. The dashed histogram represent the sum of the CC and PhP. Their samples are selected using all the selections except for $P_{T,miss}/E_T$ cut.

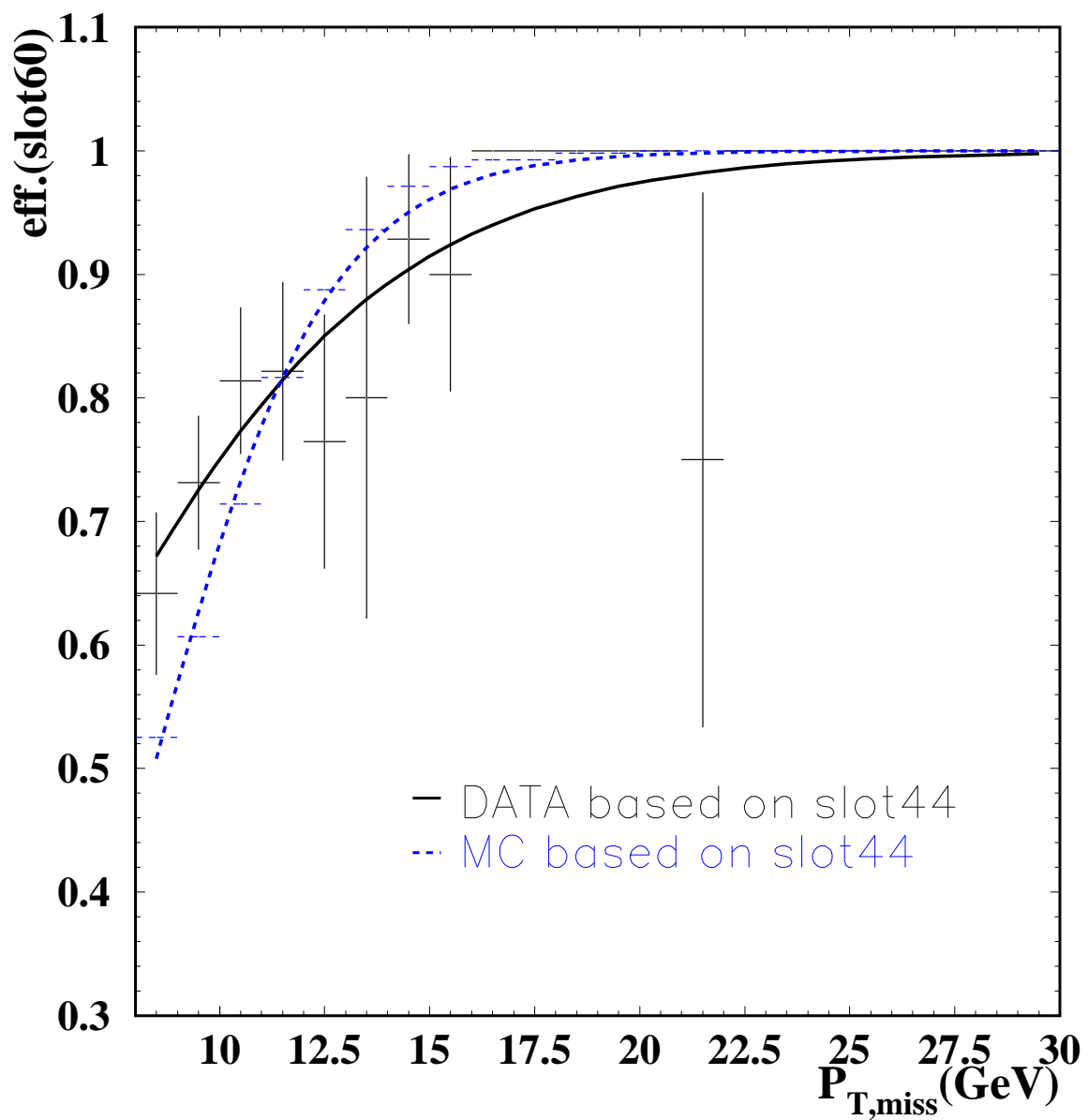


Figure 7.10: The FLT trigger slot60 efficiency as a function of $P_{T,miss}$.

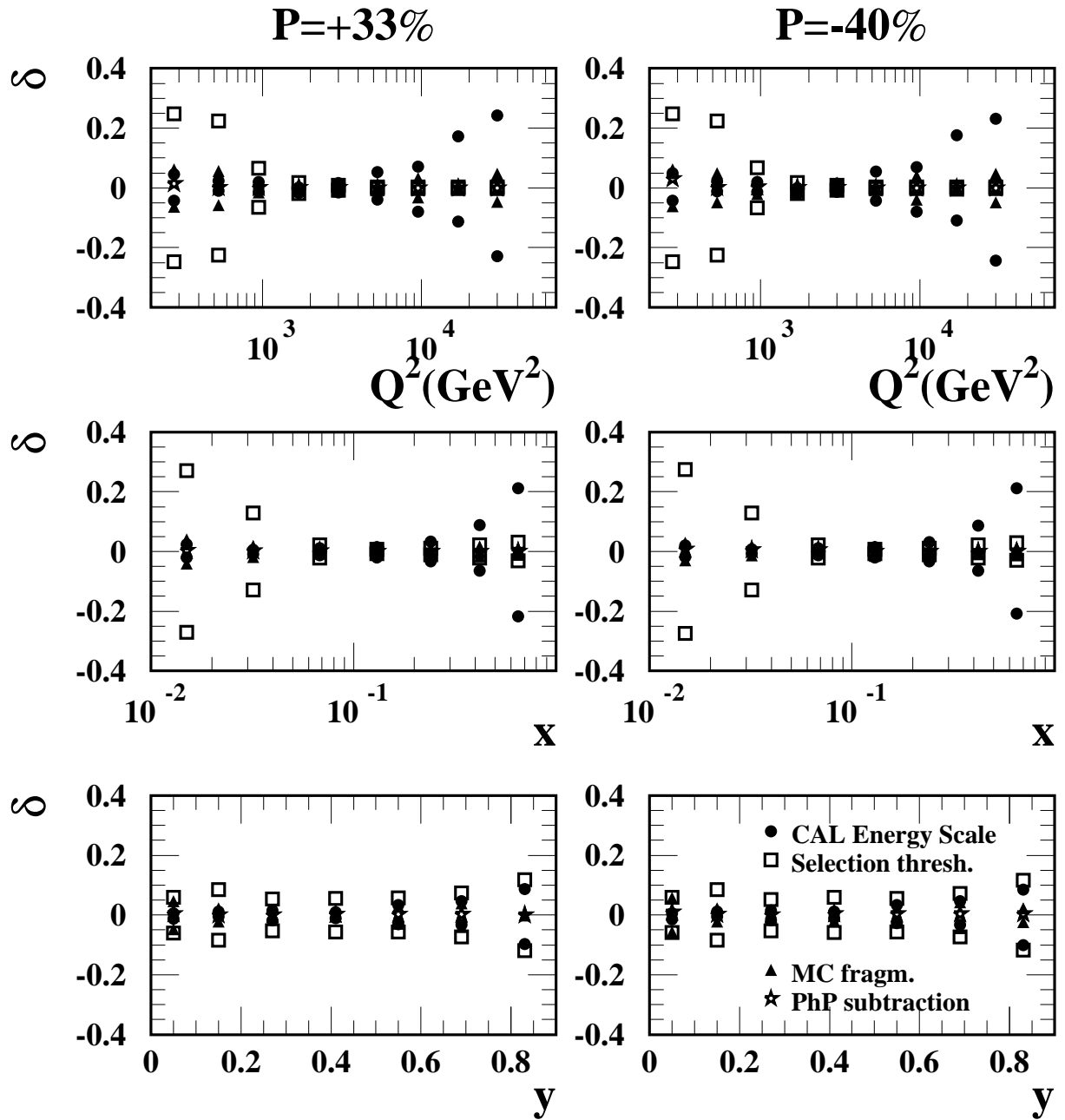


Figure 7.11: Summary of systematic uncertainties for the single differential cross sections

Chapter 8

RESULTS

In this chapter the results of the total cross section and single differential cross section are presented.

8.1 Single differential cross section

The single differential cross sections are measured as function of Q^2 , x , and y in the kinematic range of $Q^2 > 200$ GeV at the polarisation points of $P = + 32.6\%$ and $P = - 40.2\%$. Figure 8.1 shows the results, which are also summarised in Table 8.1-8.6 including the centre point (Q_c^2 , x_c and y_c), the number of the observed data events (N^{data}), the number of the estimated background events (N^{bg}), the efficiency (\mathcal{E}), the purity (\mathcal{P}) and the acceptance (\mathcal{A}), the radiative correction factor (\mathcal{C}_{rad}). The shape of the cross section measurements at $P = + 32.6\%$ and $P = - 40.2\%$ are similar, however the magnitude is clearly different, showing the left-right asymmetry of the SM. The comparison with the SM prediction of ZEUS-S PDFs is done in Figure 8.1 and the results are consistent with the SM.

Q^2 range (GeV ²)	Q_c^2 (GeV ²)	N^{data}	N^{bg}	\mathcal{E}	\mathcal{P}	\mathcal{A}	\mathcal{C}^{rad}	$d\sigma/dQ^2$ (pb/GeV ²)	
								SM prediction	results
200-400	280	40	1.6	0.14	0.60	0.23	1.02	$4.08 \cdot 10^{-2}$	$3.83^{+0.71}_{-0.60} \pm 1.00 \cdot 10^{-2}$
400-711	530	67	0.09	0.22	0.60	0.36	1.06	$2.75 \cdot 10^{-2}$	$2.82^{+0.39}_{-0.34} \pm 0.66 \cdot 10^{-2}$
711-1265	950	101	0.47	0.39	0.65	0.60	1.05	$1.71 \cdot 10^{-2}$	$1.42 \pm 0.14^{+0.099}_{-0.098} \cdot 10^{-2}$
1265-2240	1700	119	0.13	0.48	0.68	0.72	1.04	$9.20 \cdot 10^{-3}$	$7.91 \pm 0.73^{+0.17}_{-0.22} \cdot 10^{-3}$
2249-4000	3000	96	0.47	0.52	0.69	0.75	1.08	$4.07 \cdot 10^{-3}$	$3.54^{+0.40}_{-0.36} \pm 0.073 \cdot 10^{-3}$
4000-7113	5300	68	0.	0.53	0.71	0.75	1.09	$1.35 \cdot 10^{-3}$	$1.42^{+0.19}_{-0.17} \pm 0.075 \cdot 10^{-3}$
7113-12649	9500	18	0.	0.53	0.69	0.78	1.18	$2.91 \cdot 10^{-4}$	$2.12^{+0.63}_{-0.49} \pm 0.17 \cdot 10^{-4}$
12649-22494	17000	10	0.	0.49	0.65	0.75	1.21	$3.59 \cdot 10^{-5}$	$6.39^{+2.73}_{-1.98} \pm 1.10 \cdot 10^{-5}$
22494-60000	30000	0	0.	0.49	0.50	0.99	1.32	$1.96 \cdot 10^{-6}$	–

Table 8.1: The single differential cross sections $d\sigma/dQ^2$ for the e^+p data with $P = +32.6$ %

Q^2 range (GeV ²)	Q_c^2 (GeV ²)	N^{data}	N^{bg}	\mathcal{E}	\mathcal{P}	\mathcal{A}	\mathcal{C}^{rad}	$d\sigma/dQ^2$ (pb/GeV ²)	
								SM prediction	results
200-400	280	16	1.1	0.14	0.60	0.23	1.02	$1.84 \cdot 10^{-2}$	$2.12^{+0.67}_{-0.53} \pm 0.55 \cdot 10^{-2}$
400-711	530	26	0.07	0.21	0.60	0.36	1.06	$1.24 \cdot 10^{-2}$	$1.55^{+0.37}_{-0.30} \pm 0.36 \cdot 10^{-2}$
711-1265	950	43	0.35	0.39	0.65	0.59	1.05	$7.72 \cdot 10^{-3}$	$0.86^{+0.15}_{-0.13} {}^{+0.063}_{-0.061} \cdot 10^{-2}$
1265-2240	1700	43	0.11	0.48	0.68	0.70	1.05	$4.15 \cdot 10^{-3}$	$4.03 \pm 0.71 {}^{+0.61}_{-0.111} \cdot 10^{-3}$
2249-4000	3000	31	0.30	0.51	0.69	0.74	1.08	$1.83 \cdot 10^{-3}$	$1.62^{+0.34}_{-0.29} {}^{+0.029}_{-0.027} \cdot 10^{-3}$
4000-7113	5300	12	0.	0.52	0.70	0.74	1.09	$6.09 \cdot 10^{-3}$	$0.35^{+0.13}_{-0.10} {}^{+0.019}_{-0.015} \cdot 10^{-3}$
7113-12649	9500	7	0.	0.52	0.69	0.76	1.18	$1.31 \cdot 10^{-4}$	$1.17^{+0.63}_{-0.43} {}^{+0.093}_{-0.104} \cdot 10^{-4}$
12649-22494	17000	4	0.	0.47	0.65	0.73	1.21	$1.62 \cdot 10^{-5}$	$3.64^{+2.88}_{-1.74} {}^{+0.64}_{0.40} \cdot 10^{-5}$
22494-60000	30000	0	0.	0.48	0.49	0.98	1.32	$8.83 \cdot 10^{-7}$	–

Table 8.2: The single differential cross sections $d\sigma/dQ^2$ for the e^+p data with $P = -40.2\%$

x range	x_c	N^{data}	N^{bg}	\mathcal{E}	\mathcal{P}	\mathcal{A}	\mathcal{C}^{rad}	$d\sigma/dx(\text{pb})$	
								SM prediction	results
0.010-0.021	0.015	47	0.46	0.23	0.64	0.36	1.11	$6.27 \cdot 10^2$	$5.33^{+0.90}_{-0.78} \pm 1.46 \cdot 10^2$
0.021-0.046	0.032	90	0.82	0.43	0.73	0.59	1.06	$4.18 \cdot 10^2$	$3.00^{+0.35}_{-0.32} \pm 0.39 \cdot 10^2$
0.046-0.10	0.068	174	1.22	0.57	0.81	0.71	1.05	$2.18 \cdot 10^2$	$2.15 \pm 0.16^{+0.054}_{-0.056} \cdot 10^2$
0.010-0.178	0.130	119	0.	0.58	0.83	0.71	1.00	$1.00 \cdot 10^2$	$1.01 \pm 0.093^{+0.020}_{-0.024} \cdot 10^2$
0.178-0.316	0.240	72	0.	0.54	0.87	0.62	1.01	$3.59 \cdot 10^1$	$3.75^{+0.50}_{-0.44} \pm 0.13 \cdot 10^1$
0.316-0.562	0.420	9	0.	0.42	0.91	0.46	1.00	$7.32 \cdot 10^0$	$3.48^{+1.59}_{-1.14}^{+0.32}_{-0.24} \cdot 10^0$
0.562-1.000	0.650	0	0.	0.25	0.84	0.29	0.94	$5.00 \cdot 10^{-1}$	–

Table 8.3: The single differential cross sections $d\sigma/dx$ for the e^+p data with $P = + 32.6 \%$

x range	x_c	N^{data}	N^{bg}	\mathcal{E}	\mathcal{P}	\mathcal{A}	\mathcal{C}^{rad}	$d\sigma/dx(\text{pb})$	
								SM prediction	results
0.010-0.021	0.015	17	0.30	0.23	0.64	0.35	1.11	$2.82 \cdot 10^2$	$2.72^{+0.83}_{-0.65} \pm 0.75 \cdot 10^2$
0.021-0.046	0.032	43	0.67	0.43	0.73	0.58	1.06	$1.88 \cdot 10^2$	$2.02^{+0.36}_{-0.31} \pm 0.26 \cdot 10^2$
0.046-0.10	0.068	52	0.80	0.56	0.81	0.70	1.05	$9.83 \cdot 10^1$	$8.99^{+1.43}_{-1.24} {}^{+0.22}_{-0.24} \cdot 10^1$
0.010-0.178	0.130	38	0.	0.57	0.83	0.70	1.00	$4.51 \cdot 10^1$	$4.58^{+0.87}_{-0.74} {}^{+0.10}_{-0.12} \cdot 10^1$
0.178-0.316	0.240	17	0.	0.53	0.87	0.61	1.01	$1.62 \cdot 10^1$	$1.26^{+0.38}_{-0.30} {}^{+0.043}_{-0.044} \cdot 10^1$
0.316-0.562	0.420	9	0.	0.42	0.91	0.45	1.00	$3.30 \cdot 10^0$	$4.90^{+2.23}_{-1.60} {}^{+0.43}_{-0.33} \cdot 10^0$
0.562-1.000	0.650	1	0.	0.24	0.84	0.29	0.94	$2.25 \cdot 10^{-1}$	$8.78^{+20.1}_{-7.26} {}^{+1.88}_{-1.84} \cdot 10^{-1}$

Table 8.4: The single differential cross sections $d\sigma/dx$ for the e^+p data with $P = -40.2\%$

y range	y_c	N^{data}	N^{bg}	\mathcal{E}	\mathcal{P}	\mathcal{A}	\mathcal{C}^{rad}	$d\sigma/dy$ (pb)	
								SM prediction	results
0.00-0.10	0.05	97	1.03	0.39	0.92	0.42	0.98	$1.08 \cdot 10^2$	$1.15^{+0.13}_{-0.12} {}^{+0.088}_{-0.089} \cdot 10^2$
0.10-0.20	0.15	117	0.48	0.54	0.82	0.66	0.98	$8.69 \cdot 10^1$	$7.55 \pm 0.70 {}^{+0.67}_{-0.66} \cdot 10^1$
0.20-0.34	0.27	118	0.079	0.55	0.80	0.69	1.02	$6.36 \cdot 10^1$	$5.41 \pm 0.50 \pm 0.30 \cdot 10^1$
0.34-0.48	0.41	81	0.37	0.47	0.74	0.63	1.03	$4.60 \cdot 10^1$	$4.08 {}^{+0.51}_{-0.50} \pm 0.23 \cdot 10^1$
0.48-0.62	0.55	46	0.36	0.38	0.69	0.55	1.03	$3.49 \cdot 10^1$	$2.65 {}^{+0.45}_{-0.39} \pm 0.19 \cdot 10^1$
0.62-0.76	0.69	44	0.33	0.28	0.65	0.44	1.06	$2.78 \cdot 10^1$	$3.32 {}^{+0.58}_{-0.50} {}^{0.32}_{0.30} \cdot 10^1$
0.76-0.9	0.83	16	0.063	0.17	0.59	0.29	1.08	$2.36 \cdot 10^1$	$1.86 {}^{+0.59}_{-0.46} {}^{0.27}_{0.28} \cdot 10^1$

Table 8.5: The single differential cross sections $d\sigma/dy$ for the e^+p data with $P = + 32.6$ %

y range	y_c	N^{data}	N^{bg}	\mathcal{E}	\mathcal{P}	\mathcal{A}	\mathcal{C}^{rad}	$d\sigma/dy$ (pb)	
								SM prediction	results
0.00-0.10	0.05	35	0.75	0.38	0.92	0.41	0.98	$4.87 \cdot 10^1$	$5.84^{+1.16}_{-0.98} {}^{+0.48}_{-0.49} \cdot 10^1$
0.10-0.20	0.15	42	0.32	0.53	0.82	0.65	0.98	$3.92 \cdot 10^1$	$3.83^{+0.69}_{-0.59} \pm 0.34 \cdot 10^1$
0.20-0.34	0.27	41	0.050	0.54	0.80	0.68	1.02	$2.86 \cdot 10^1$	$2.66^{+0.48}_{-0.41} \pm 0.15 \cdot 10^1$
0.34-0.48	0.41	28	0.30	0.47	0.74	0.63	1.03	$2.08 \cdot 10^1$	$1.98^{+0.45}_{-0.37} {}^{+0.13}_{-0.12} \cdot 10^1$
0.48-0.62	0.55	16	0.24	0.37	0.69	0.54	1.03	$1.58 \cdot 10^1$	$1.31^{+0.41}_{-0.32} {}^{+0.091}_{-0.088} \cdot 10^1$
0.62-0.76	0.69	15	0.22	0.28	0.65	0.43	1.06	$1.25 \cdot 10^1$	$1.59^{+0.53}_{-0.41} {}^{+0.15}_{-0.14} \cdot 10^1$
0.76-0.9	0.83	5	0.058	0.17	0.59	0.29	1.08	$1.06 \cdot 10^1$	$0.81^{+0.55}_{-0.35} {}^{+0.12}_{-0.13} \cdot 10^1$

Table 8.6: The single differential cross sections $d\sigma/dy$ for the e^+p data with $P = -40.2\%$

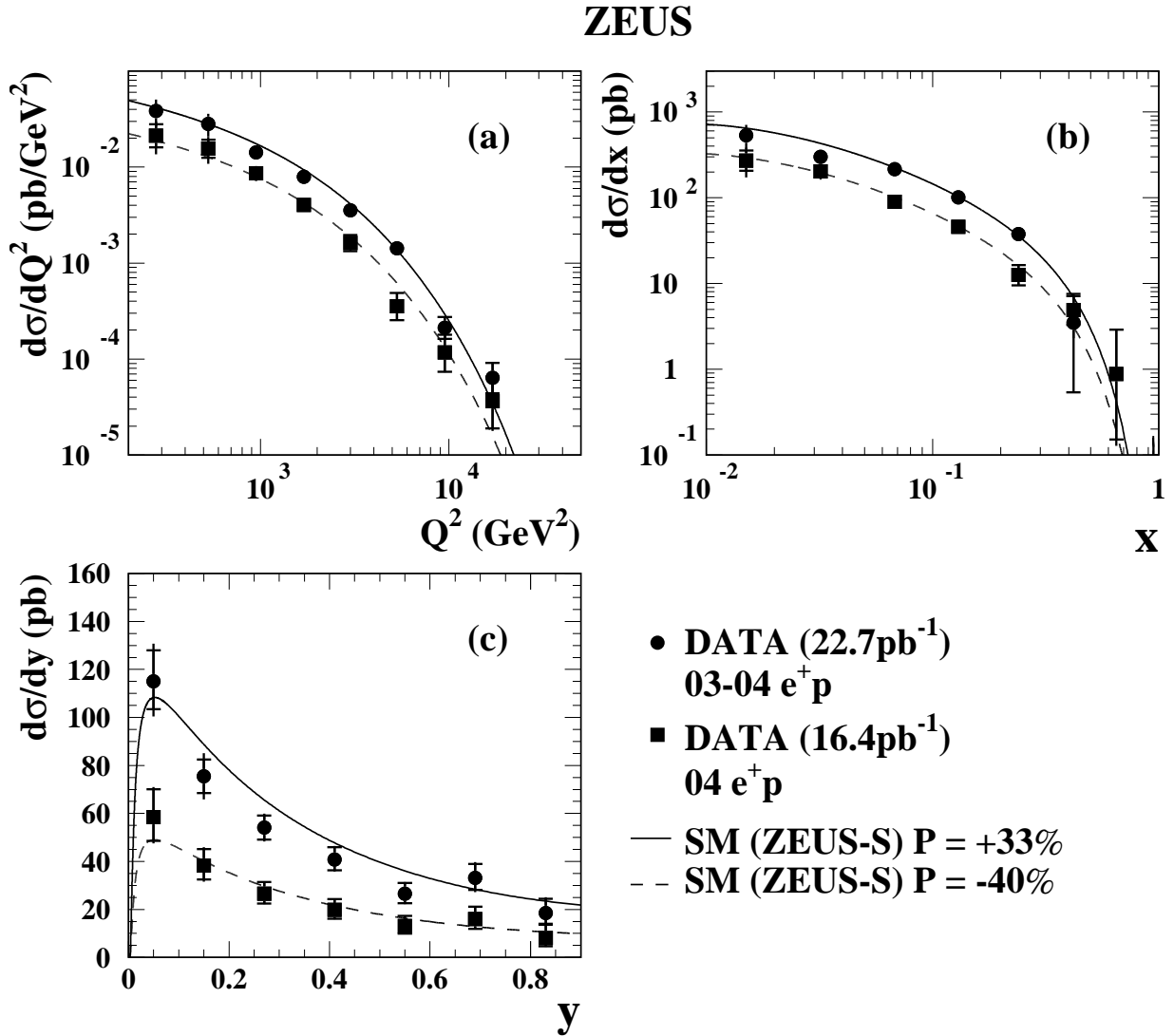


Figure 8.1: The Single differential cross section, (a) $d\sigma/dQ^2$, (b) $d\sigma/dx$ and (c) $d\sigma/dy$. Closed circles denote the CC cross section for the positron polarisation of $P = +32.6\%$. Closed square denotes for the positron polarisation of $P = -40.2\%$. The solid line denotes the SM prediction for $P = +32.6\%$ and the dashed line for $P = +40.2\%$.

8.2 Total cross section

The total CC DIS cross sections in $Q^2 > 200 \text{ GeV}^2$ for the longitudinally polarised positrons with the protons are measured.

The results are, for positron polarisation, $P = +32.6 \pm 0.9\%$,

$$\sigma_{tot}^{CC}(P = +32.6 \%) = 43.14 \pm 1.89(\text{stat.}) \pm 2.71(\text{syst.}) \text{ pb}, \quad (8.1)$$

for $P = -40.2 \pm 1.2\%$,

$$\sigma_{tot}^{CC}(P = -40.2 \%) = 21.34 \pm 1.58(\text{stat.}) \pm 1.39(\text{syst.}) \text{ pb}, \quad (8.2)$$

where the first error is the statistical uncertainty and the second error is the total systematic uncertainty. The uncertainties of the luminosity measurement of 5 % are not included. The SM predictions are 47.67 pb for $P = +32.6 \%$ and 21.48 pb for $P = -40.2 \%$. The measured cross sections are in good agreement with their predictions.

The measurements for unpolarised positron was $\sigma_{tot}^{CC}(P=0) = 34.8 \pm 0.9(\text{stat.})_{-1.0}^{+0.9}(\text{sys.})$ pb [36]. The total cross sections at $P = +32.6 \%$ and $P = -40.2 \%$ are 2.5 standard deviations above and 6.7 standard deviations below the unpolarised measurement, respectively. The left-right asymmetry of the SM is clearly shown.

The measured results are compared with this unpolarised results and the SM prediction from the ZEUS-S PDFs [37] in Figure 8.2 as a function of the positron polarisation, P . The uncertainties of the luminosity measurement are included in this figure, as a quadratic sum to experimental systematic errors.

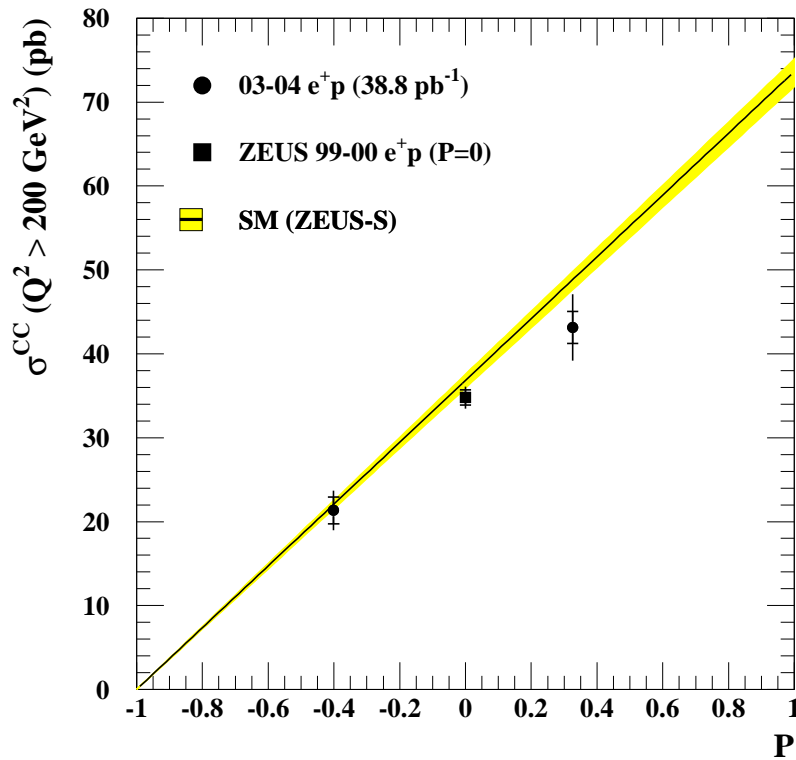


Figure 8.2: The measured total cross sections; closed circles denote the CC cross section for the positron polarisation of $P = +32.6\%$ and -40.2% . Closed square denotes the unpolarised CC cross section from 1999-2000 data. The solid line denotes the SM prediction. These uncertainties for measured three cross section are including the systematics and luminosity measurements.

Chapter 9

Discussion of search of W_R boson

The measured cross sections at $P = -40.2\%$, 0% and $+32.6\%$ are linearly fitted and then we extrapolate to $P = -100\%$ to extract σ_{CC}^R because the left-handed CC DIS cross section should be zero at $P = -100\%$. In this chapter, the method for extracting σ_{CC}^R is presented.

9.1 Limit of σ_{CC}^R

The method of linear least squares (see Appendix .1) is used as a fit method. The result is from the statistical error,

$$\sigma_{CC}^R = 3.63 \pm 3.26(stat.) \text{ pb.} \quad (9.1)$$

We estimated the various systematic uncertainties for the total cross section in Section 7.8. Table 9.1 shows the summaries of systematic uncertainties and their correlation for three data sets with different beam polarisation. It is important to take account of the correlation in the systematic uncertainties, since all uncertainties behave coherently for these measured cross sections. As the event selection procedure has changed a lot in this analysis compared with the previous one for unpolarised positron beam, the correlation between the two measurements is considered to be weak. This is true also for the luminosity measurements, since the detector has upgraded. However, since the two polarised cross sections are fully correlated and since the uncertainty for unpolarised cross section is much smaller than polarised ones, all the systematic uncertainties are treated as fully correlated among the three data sets. For the correlated systematic errors, these cross sections are shifted coherently by amount of uncertainty and re-fit is performed.

The fit results are shown in Table 9.1. The deviation from the centre value ($\sigma^{centre} = 3.63$ pb) is summed quadratically and the systematic uncertainty is set as

$$\sigma_{syst} = \sqrt{\sum_{ierr} (\sigma_{ierr}^{centre} - \sigma^{centre})^2}, \quad (9.2)$$

where σ_{ierr}^{centre} denotes centre value of the each re-fit for systematic uncertainty.

The result is

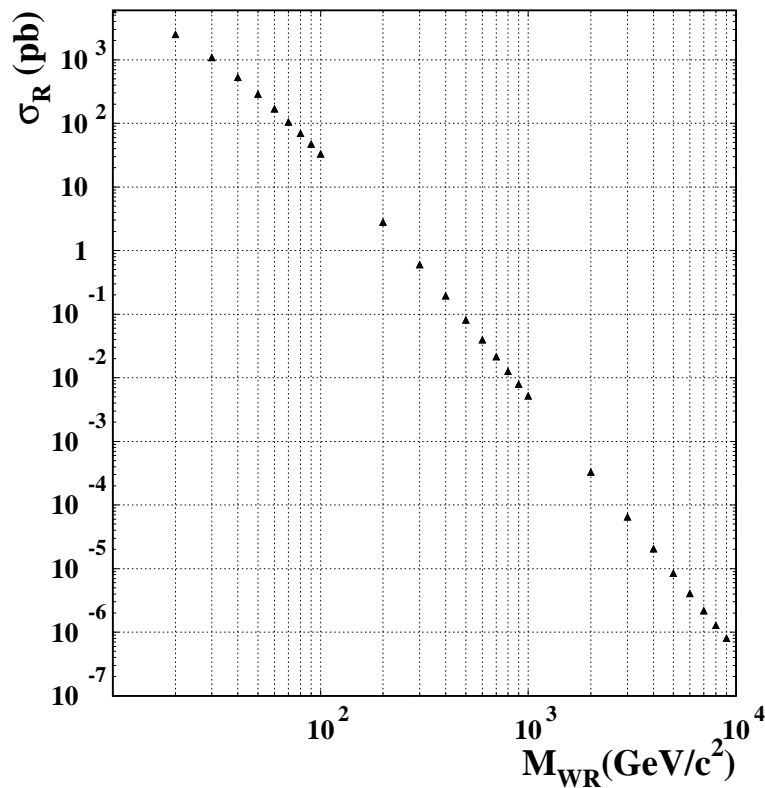
$$\sigma_{CC}^R = 3.63 \pm 3.26(stat.) \pm 1.27(syst.) \text{ pb} \quad (9.3)$$

The measurement is still statistically limited. The dominant systematic uncertainty is from the polarisation measurement. This cross section is consistent with the Standard Model prediction of a zero. Considering 97.5 % confidence level, $\sigma_{CC}^R < 10.6$ pb. Figure 9.1 shows theory prediction of σ_{cc}^R as a function of W_R mass, as calculated using the HECTOR [42]. The above σ_{CC}^R limit is converted to the lower limit of M_{W_R} : $M_{W_R} > 116$ GeV.

	$P = -40.2 \%$	$P = 0 \%$	$P = +32.6 \%$	correlation of 3 points
Total cross section(pb)	21.3	34.8	43.1	–
Statistical error(pb)	± 1.58	± 0.90	± 1.90	NO
CAL energy scale(pb)	± 0.14	$^{+0.17}_{-0.09}$	$^{+0.29}_{-0.30}$	YES
Selection threshold(pb)	± 1.32	± 0.16	± 2.67	YES
QCD cascade model(pb)	± 0.14	± 0.38	± 0.40	YES
Background Subtraction(pb)	± 0.09	$^{+0.14}_{-0.24}$	± 0.08	YES
Luminosity measurement(pb)	± 1.07	± 0.78	± 2.16	YES
Polarisation $\delta P(\%)$	± 1.17	± 0.0	± 0.91	YES (anti-correlation)

Table 9.1: Systematic uncertainties for total cross section

error item	cross section (pb) at $P = -100\%$	
Statistical error	3.63 ± 3.26	
	+ error fit	- error fit
CAL energy scale	3.64 ± 3.29	3.65 ± 3.24
Selection thresholds	3.53 ± 3.47	3.72 ± 3.06
QCD cascade model	3.57 ± 3.29	3.70 ± 3.24
Background Subtraction	3.75 ± 3.28	3.51 ± 3.25
Luminosity measurement	3.66 ± 3.43	3.60 ± 3.10
Polarisation	4.49 ± 3.17	2.73 ± 3.36

Table 9.2: Results of the extrapolation to $P = -100\%$ Figure 9.1: Theory prediction of W_R cross section as function of W_R mass calculated by HECTOR [42]

Chapter 10

CONCLUSION

The charged current deep inelastic scattering cross sections in e^+p collisions with longitudinally polarised positron beams were measured at a centre of mass energy of 318 GeV. The measurements are based on two data sets with opposite signed polarisation P . These integrated luminosities are 22.7 pb^{-1} for polarisation $P = +32.6 \pm 0.9 \%$ and 16.4 pb^{-1} for $P = -40.2 \pm 1.2 \%$ which are collected with the ZEUS detector since 2003 autumn until 2004 summer.

Observed are 519 and 182 CC DIS candidates for data with $P = +32.6 \%$ and $P = -40.2 \%$, respectively. In the various distributions of these final candidates, data and the Monte Carlo are in good agreement.

The single differential cross sections as functions of Q^2 , x and y are measured. These cross sections are described by the Standard Model (SM) prediction with the ZEUS-S parton distribution function. The shape of the cross sections between both of polarisations are similar, and only the magnitude is different, as expected from the beam helicity effect. It demonstrates the left-right asymmetry of the weak interaction.

The total cross sections are measured. The results are

$$\sigma_{tot}^{CC}(P = +32.6 \%) = 43.14 \pm 1.89(\text{stat.}) \pm 2.71(\text{syst.}) \text{ pb},$$

$$\sigma_{tot}^{CC}(P = -40.2 \%) = 21.34 \pm 1.58(\text{stat.}) \pm 1.39(\text{syst.}) \text{ pb}.$$

Comparing to the unpolarised measurement, these results for $P = +32.6 \%$ and $P = -40.2 \%$ are 2.5 standard deviations above and 6.7 standard deviations below,

respectively. Clearly the left-right asymmetry is observed.

The right-handed charged current cross section is extracted. The result is

$$\sigma_{CC}^R = 3.63 \pm 3.26(stat.) \pm 1.27(syst.) \text{ pb.} \quad (10.1)$$

This cross section is consistent to zero as expected in the SM. Assuming the coupling strength of right-handed W boson (W_R) is same as that of the SM W boson, the lower limit on the mass of W_R is evaluated as 116 GeV at 97.5 % confidence level.

Appendix

.1 The method of linear least squares fitting

We consider the very a straight line Data fitted well to a set of data points $(x_1, y_1 \pm \sigma_1), \dots, (x_n, y_n \pm \sigma_n)$. The fitted function is defined as,

$$f(x) = a + bx, \quad (2)$$

where a and b are the unknown parameters. In this case, we assume there are uncertainties σ_n in the y -coordinate of each point. This line is determined as χ^2 becomes the smallest and defined as follows,

$$\chi^2 \equiv \sum_{i=1}^n (w_i(y_i - a - bx_i))^2, \quad (3)$$

where the summation extends over all the n data points and $w_i = 1/\sigma_i^2$. After differentiating Eq. 2 and substituting to 3, we obtain the following eqations:

$$\sum_{i=1}^n w_i y_i = a \sum_{i=1}^n w_i + b \sum_{i=1}^n w_i x_i, \quad (4)$$

$$\sum_{i=1}^n w_i x_i y_i = a \sum_{i=1}^n w_i x_i + b \sum_{i=1}^n w_i x_i^2. \quad (5)$$

From Eq. 4 and 5, we determine a and b as follows,

$$\begin{aligned}
a &= \frac{1}{D} \begin{vmatrix} \sum w_i y_i & \sum w_i x_i \\ \sum w_i x_i y_i & \sum w_i x_i^2 \end{vmatrix} \\
&= \frac{1}{D} (\sum w_i y_i \sum w_i x_i^2 - \sum w_i \sum w_i x_i y_i),
\end{aligned} \tag{6}$$

$$\begin{aligned}
b &= \frac{1}{D} \begin{vmatrix} \sum w_i & \sum w_i y_i \\ \sum w_i x_i & \sum w_i x_i y_i \end{vmatrix} \\
&= \frac{1}{D} (\sum w_i \sum w_i x_i y_i - \sum w_i x_i \sum w_i y_i),
\end{aligned} \tag{7}$$

where D is,

$$\begin{aligned}
D &= \begin{vmatrix} \sum w_i & \sum w_i x_i \\ \sum w_i x_i & \sum w_i x_i^2 \end{vmatrix} \\
&= \sum w_i \sum w_i x_i^2 - (\sum w_i x_i)^2.
\end{aligned} \tag{8}$$

Next, errors for a and b can be determined from *the law of error propagation* and they (σ_a and σ_b) are,

$$\sigma_a = \frac{1}{D} \sum_{i=1}^n w_i x_i^2, \tag{9}$$

$$\sigma_b = \frac{1}{D} \sum_{i=1}^n w_i. \tag{10}$$

At $x = x_i$, error for y -coordinate are obtained as follows,

$$\sigma_y^2 = x^2 \sigma_b^2 + 2x \text{cov}(a, b) + \sigma_a^2. \tag{11}$$

where the $\text{cov}(a, b)$ is covariance term between a and b . In particular, if x position where σ_y is determined is set to 0, the covariance term disappears and we can simply obtain as follows,

$$\sigma_y^2 = x^2 \sigma_b^2 + \sigma_a^2. \quad (12)$$

Acknowledgements

First of all, I would like to appreciate to my supervisor Prof. S. Noguchi for giving opportunity of my studying at ZEUS group from the doctor course and his support and encouragement to me for three years.

I express my gratitude to Prof. K. Tokushuku for always making me be at the best surrounding of my research and giving me his advice and supports. I appreciate to his reading my manuscript many times, his advice and discussions with me.

I am really thankful to Dr. K. Nagano. The analysis presented in this thesis went smoothly thanks to lots of discussions with him. Further, I learned the working posture in High Energy Physics from him.

I am also very thankful to my coordinators of ZEUS high Q^2 group, Dr. A. Tapper, Prof. E. Tassi, Dr. K. Wichmann, Dr. E. Gallo and Dr. S. Schlenstedt for giving the chance of such a great analysis topics and helping with hearty look. I would like to thank to Mr. A.M. Gabareen for working together with me and his thoughtfulness for me at working. And to High Q^2 group friends, I could enjoy the meeting and feel comfortable with them.

I would like to thank the ZEUS collaboration for helping my analysis, especially to Dr. U. Stösslein, Dr. L. Gladilin and Dr. H. Lim for their support on analysing new data. I would have made this results so quickly with new data without their efforts.

I am thankful to ZEUS Tokyo group. First I would like to thank to Dr. Y. Yamazaki and Prof. M. Kuze for their eager, care and many advice. I had a poor knowledge of ZEUS at my first stay. since then, I leaned HERA physics from the basics thanks to their kindly helps and patience. It is the great time to discuss with Prof. Y. Iga, Prof. R. Hamatsu, Prof. S. Kitamura, Prof. T. Tsurugai and Prof. S. Yamada at the group meeting, which let me think carefully about my analysis again with their comments. And I am thankful to the ZEUS Tokyo group students. I enjoyed the time at DESY thanks to them.

I would like to say special thanks to my mothers of Hamburg, Frau. H. Thiel, Frau. E. Kaplanski and Frau U. Dorn, with whom I lived under the same roof in Hamburg, Frau. Y. Shogase and Frau. M. Saeki. They taught me the ABC of German life. I was happy to see them, for which I could spend without loneliness in Hamburg.

I am thankful to Mrs. K. Ma for her kindness. I shall never forget having a chat at breaks and good time with you at DESY. I am thankful to Dr. T. Kohno. I could finish writing my thesis in good spirits thanks to him.

Finally, I had a lot of great experiences in Germany thanks to my family for their willing permission of my visiting to Germany. I would like to show my gratitude to my family for the best love, patient, understanding and encouragement.

Bibliography

- [1] E. Rutherford, *Phil. Mag.* **21**(1911) 669.
- [2] UA2 Collaboration, J. Alitti, *et al.* *Nucl. Phys.* **B400**, 3 (1993)
- [3] D0 Collaboration, B. Abbott, *et al.* International Europhysics Conference on High Energy Physics, August 19-26, 1997, Jerusalem, Israel.
- [4] D0 Collaboration, S. Abachi, *et al.* *Phys. Rev. Lett.* **76**, 3271 (1996).
- [5] CDF Collaboration, F. Abe, *et al.* *Phys. Rev. Lett.* **74**, 2900 (1995).
- [6] M. Kuze and Y. Sirois, Search for Particles and Forces beyond the Standard Model at HERA *ep* and Tevatron *p \bar{p}* Colliders, DESY 02-165 (2002).
- [7] H. Spiesberger, "HERACLES and DJANGO: Event Generation for ep Interaction at HERA Including Radiative Processes", 1998, available on <http://www.desy.de/hspiesb/djangoh.html>.
- [8] A. Kwiatkowski, H. Spiesberger, H. J. Möhring, *Comp. Phys. Commun.* **69** (1992)155-172.
H. Spiesberger, "HERACLES - An Event Generator for ep interactions at HERA Including Radiative Processes (Version 4.6)", 1996, available on <http://www.desy.de/hspiesb/heracles.html>.
- [9] G. Ingelman, A. Edin, J. Rathsman, *Comp. Phys. Commun.* **101** (1997) 108-134.
- [10] L. Lönnblad, *Comp. Phys. Commun.* **71** (1992) 15.
- [11] U. Baur, J.A.M Vermaseren, D.Zeppenfeld, *Nucl. Phys.*,**B875** (1992) 3.
- [12] J.A.M Vermaseren, *Nucl. Phys.*,**B229** (1983) 347.
- [13] M. Minty, "SUMMARY OF RECENT HIGH LUMINOSITY EXPERIMENTS AFTER THE HERA-II LUMINOSITY UPGRADE AND FUTURE PROSPECTS", DESY HERA 03-25 (2003).

- [14] A.A Sokolov and I.M. Ternov, Sov. Phys. Doklady**8**, 1203 (1962).
- [15] D.P. Barber et al., The HERA Polarimeter and the First Observation of Electron Spin Polarimeter at HERA, DESY 92-136 (1992).
- [16] M. Beckmann et al, Nucl. Instr. and Meth. A479 (2002)334.
- [17] ZEUS Collaboration, M. Derrick, et al., The ZEUS Detector, Status Report 1993, DESY (1994), available on <http://www-zeus.desy.de/bluebook/bluebook.html>.
- [18] B. Foster et al., Nucl. Inst. Meth. **A 338**, 254 (1994)
- [19] ZEUS Collaboration, Calorimeter group, U. Behrens et al., Nucl. Inst. Meth. **A 289**, 115 (1990).
- [20] ZEUS Luminosity Group, *Luminosity Measurement in the ZEUS Experiment, ZEUS Note 01-004, 2001.*
- [21] ZEUS Luminosity Group, *Proposal of an Upgraded Luminosity Monitor for the ZEUS Experiment, 1999.*
- [22] ZEUS Luminosity Group, *Aerogel Cherenkov Detectors for the luminosity Measurement at HERA, ZEUS Note 02-013, 2002.*
- [23] W.H. Smith et al. *The ZEUS Trigger System, ZEUS Note 89-084, 1989.*
- [24] F. Jacquet and A. Blondel, 'Proceedings of the Study for and *ep* Facility for Europe', U. Amaldi (ed.), p.391. Hamburg Germany (1979). Also in preprint DESY 79/48
- [25] S. Bentvelsen, J Engelen and P. Kooijman, 'Reconstruction of (x, Q^2) and extraction of structure functions in neutral current scattering at HERA, Proc. Workshop on Physics at HERA', W. Buchmüller and G. Ingelman (eds.), Vol.1, p. 23. Hamburg, Germany, DESY (1992)
- [26] G. Briskin, Ph. D. thesis, University of Tel Aviv, 1998; DESY-THESIS-1998-036.
- [27] A. Savin, 'Study of calorimeter noise in the 1996 data', ZEUS Note 98-007 Calorimeter group, 1998.
- [28] J. Grosse-Knetter, 'Corrections for the Hadronic Final State', ZEUS Note 98-031, 1998.

- [29] G.F. Hartner *et al.*, 'VCTRAK (3.07/04): Offline Output Information', ZEUS Note 97-064, 1997.
- [30] A. Arnulf and O. Ruske, 'A New Method to Measure Vertex Distribution', ZEUS Note 98-036, 1998.
- [31] R. Pawlak, 'Vertex reconstruction from FCAL timing', ZEUS Note 98-040, 1998.
- [32] K. Nagano, 'Tight Track Veto study update', ZEUS internal *ZEMS* 19th November 2004 @ Trigger meeting
- [33] H. Abramowicz, A. Caldwell, R. Sinkus, 'Neural Network Based Electron Identification in the ZEUS Calorimeter', DESY Note 95-054. R. Sinkus, Nucl. Inst. Meth. **A 361** (1995) 290.
- [34] ZEUS Collab., J. Breitweg *et al.*, Eur. Phys. J. **C11**(1999)3, 427-445.
- [35] K. Nagano, ZEUS internal page 'ZEMS', High- Q^2 group, 17th November, 2004
- [36] ZEUS Collab., S. Chekanov *et al.*, 'Measurement of high- Q^2 charged current cross-sections in e^+p deep inelastic scattering at HERA', Eur. Phys. J. **C32**(2003).
- [37] ZEUS Collab., S. Chekanov *et al.*, 'A ZEUS next-to-leading-order QCD analysis of data on deep inelastic scattering', Phys. Rev. **D67**,012007(2003), hep-ex/0208023
- [38] J. Pati and A. Salam, Phys. Rev. **D 10 (1974) 275**; R.E. Marshak and R.N. Mohapatra, Phys. Lett **B 91 (1974) 222**.
- [39] R.N Mahapatra, Phys. Rev. **D 34 (1986)3457**.
- [40] S.P Martin, Phys. Rev. **D 46 (1992)2769**.
- [41] C.S Aulakh, A.Melfo and G.Senjanovič, Phys. Rev. **D 57 (1998)4174**.
- [42] HECTOR program manual; DESY preprint 95-185